

High and low velocity collisions between porous small bodies in our Solar System

Dissertation

der Mathematisch-Naturwissenschaftlichen Fakultät
der Eberhard Karls Universität Tübingen
zur Erlangung des Grades eines
Doktors der Naturwissenschaften
(Dr. rer. nat.)

vorgelegt von
Oliver Jürgen Wandel
aus Reutlingen

Tübingen
2020

Gedruckt mit Genehmigung der Mathematisch-Naturwissenschaftlichen Fakultät der
Eberhard Karls Universität Tübingen.

Tag der mündlichen Prüfung:

20.11.2020

Stellvertretender Dekan:

Prof. Dr. József Fortágh

1. Berichterstatter:

Prof. Dr. Wilhelm Kley

2. Berichterstatter:

Prof. Dr. Klaus Werner

Contents

1	Introduction	5
1.1	Small bodies in our Solar System	5
1.1.1	Dynamical classification	5
1.1.2	Properties	6
1.2	Porous bodies	11
1.2.1	Observations and findings	11
1.2.2	Influence of porosity	11
1.3	Outlook	15
2	Porosity	17
3	Numerics	21
3.1	Smooth Particle Hydrodynamics	21
3.1.1	Hydrodynamic equations	23
3.1.2	Solid body mechanics	25
3.2	Physical and numerical models	25
3.2.1	Equation of state	25
3.2.2	Strength models	25
3.2.3	Fragmentation model	25
3.3	Porosity models	26
4	Publications	27
5	Conclusion & Outlook	105

Abstract

Recent space missions like New Horizons, observations and interplanetary dust particles found on Earth show that asteroids belonging to the taxonomic classes C and D, centaurs, as well as Kuiper-belt objects have low bulk densities ($\leq 1300 \text{ kg/m}^3$) compared to terrestrial planets. This indicates that the solar system in its early stages likely consisted of highly porous small bodies. For the purpose of studying the formation of asteroids and planetesimals alike, it is essential to understand the collisional process, the different behaviour, as well as the dissipative nature of porous materials. Impact studies suggest that due to their dissipative nature, porous bodies show a higher material strength than bodies without porosity (Stewart & Ahrens, 1999). Furthermore, cratering events could involve more compaction and less ejection (Housen & Holsapple, 1999).

In this thesis, we mainly use the so-called P - α model (Herrmann, 1969) to account for the effect of porosity in order to investigate collisions and impacts between porous bodies. The model is described in detail including validation simulations and a display of the timestep resolution for the iterative relation between the pressure P and the distention α . The time resolution is of importance due to the existence of a specific pressure value for a specific distention value. If the relation of values does not agree, the timestep has to be reduced. We studied the formation of the largest crater on the Mars moon Phobos called Stickney, tightening the parameter space for the impactor size, velocity, as well as porosity. Furthermore, we investigated the comet-like activity of porous main-belt comets resulting from the sublimation of sub-surface water-ice getting exposed by impacts of meter-sized bodies. The crater of these porous bodies becomes larger and can be used as an upper limit for the depth at which ice needs to be present.

In addition, we found a formation channel for the Kuiper-belt contact binary Arrokoth (2014 MU₆₉), which has been visited by the New Horizons spacecraft, using semi-secular Lidov-Kozai oscillations. They are induced by the Sun and may lead to changes of the inner orbit's mutual inclination and its eccentricity on timescales that are much longer compared to the orbital period. The collision velocity of Ultima and Thule to form Arrokoth approximately amounts to the escape velocity which is of the order of a few m/s. With Smooth Particle Hydrodynamics (SPH) simulations we scanned the parameter space of material strength and impact angle.

Our studies conclude that porosity plays a major role in the outcome of porous body collisions. One can not simply reduce the bulk modulus, as well as the density, and use a model for non-porous material to account for porosity. Further investigations regarding porous materials will improve the understanding of formation processes of small bodies and planetesimals alike as well as the strength of these weak bodies.

Zusammenfassung

Die Untersuchung der Zusammensetzung von interplanetaren Objekten ist unter anderem möglich mit Hilfe von aktuelle Raumfahrtmissionen wie New Horizon, diverse Beobachtungen sowie auf der Erde gemessene, interplanetare Staubpartikel. Dabei kann gezeigt werden, dass Asteroiden der taxonomischen Klasse C und D, Zentauren und Objekte des Kuipergürtels im Vergleich zu terrestrischen Planeten niedrigere Dichten ($\leq 1300 \text{ kg/m}^3$) besitzen. Dies weist daraufhin, dass das frühe Sonnensystem wahrscheinlich aus sehr porösen, kleinen Körpern bestand. Um die Entstehung von Planetesimalen und Asteroiden gleichermaßen zu verstehen, ist vertieftes Wissen über den Kollisionsprozess, das unterschiedliche Verhalten sowie die dissipative Natur von porösem Material notwendig. Einschlagsstudien haben herausgefunden, dass sich poröse Körper aufgrund ihrer dissipativen Eigenschaften „stärker“ verhalten im Bezug auf ihre Materialeigenschaften als Körper ohne Porosität (Stewart & Ahrens, 1999). Darüber hinaus könnten Einschlagsereignisse zu verstärkter Verdichtung und einer Verringerung des Auswurfmaterials führen (Housen & Holsapple, 1999).

Um die Auswirkung der Porosität zu berücksichtigen, die bei Kollisionen und Einschlägen zwischen porösen Körpern wichtig ist, verwenden wir in dieser Arbeit das sogenannte P - α Modell (Herrmann, 1969). Detaillierte Beschreibungen des Modells beinhalten sowohl Validierungssimulationen als auch eine Diskussion der zeitlichen Auflösung für die iterative Beziehung zwischen dem Druck P und der Distention α . Diese Arbeit beinhaltet die Untersuchung des größten Kraters Stickney auf dem Marsmond Phobos und eine Einschränkung des entsprechenden Parameterraums für die Größe des Einschlagobjekts, der Geschwindigkeit sowie der Porosität. Darüber hinaus untersuchen wir poröse Kometen des Hauptgürtels, die streng genommen eigentlich als Asteroiden klassifiziert sind. Aufgrund der Sublimation von unterirdischem Wassereis, welches durch Einschläge von metergroßen Körpern freigesetzt wird, besitzen diese Objekte allerdings kometenähnliche Eigenschaften und Aktivitäten. Die Krater dieser porösen Körper werden größer, was als obere Grenze verwendet werden kann für die Tiefe, bei welcher Eis zur Sublimation vorhanden sein muss. Für den Kontakt-Doppelasteroid Arrokoth (2014 MU₆₉) im Kuipergürtel, welcher kürzlich mithilfe der New Horizons Raumsonde beobachtet wurde, konnte außerdem unter Verwendung von sogenannten semi-sekulären Lidov-Kozai Oszillationen ein Entstehungskanal gefunden werden. Die Kollisionsgeschwindigkeit von Ultima und Thule, die nötig ist um Arrokoth zu formen, ist ungefähr in der Größenordnung der Fluchtgeschwindigkeit von ein paar m/s. Mithilfe von Smooth Particle Hydrodynamics (SPH) Simulationen haben wir dabei den Parameterraum der Materialstärke und des Kollisionswinkels untersucht. Unsere Ergebnisse zeigen, dass Porosität für Kollisionen von porösen Körpern und deren En-

dergebnis eine wichtige Rolle spielt. Es ist dabei nicht möglich, einfach nur sowohl das Kompressionsmodul als auch die Dichte zu verringern und ein Modell für nicht-poröse Körper zu verwenden. Weitere Untersuchungen von porösen Materialien können in Zukunft dazu beitragen, die Entstehung von kleinen Körpern und Planetesimalen sowie die Materialeigenschaft und Festigkeit von diesen schwachen Körpern besser zu verstehen.

Introduction

Small bodies are the remainder of early planetary formation in our Solar System. The valuable information regarding the accretion of planetesimals is still available in this population. This field of study started with the discovery of 1 Ceres over 200 years ago by the Italian astronomer Giuseppe Piazzi. Over the last decades, the knowledge and insight regarding small bodies in our Solar System have grown immensely. There have been (e.g., Deep Impact, Stardust NExT, Dawn, New Horizons) and will be many sky-surveys (LSST), impact spacecraft missions (DART, HERA), laboratory measurements, as well as computational simulations to research the evolution and composition of small bodies. One main interest is to investigate the primordial environment of solar nebula where the planets were formed. We therefore obtain knowledge about the formation phase of our Solar System by studying primitive objects. Furthermore, we can study the processes and forces which are significant only when acting on small bodies (e.g., radiation pressure). Over half a million unique objects have been observed, ranging from small near-Earth asteroids to main-belt comets and Kuiper-belt objects to so-called Trans-Neptunian Objects (TNOs).

1.1 Small bodies in our Solar System

1.1.1 Dynamical classification

There are different classes of small bodies. Near Earth Objects (NEOs) are asteroids, comets, and large meteorites with perihelion distances less than 1.3 Astronomical Units (au). Currently, there are over 20.000 known NEOs. Their orbits have been studied in great detail so it is possible to identify those intersecting Earth's in order to warn as well as defend against possible hazardous impacts. In 2005 the Japanese spacecraft Hayabusa had its flyby near 25143 Itokawa, which is a NEO with a diameter of about 300 m.

Located between the orbits of Mars and Jupiter are the so-called Main Belt Objects (MBOs). Ceres is the largest asteroid in the main belt, large enough to be called a dwarf planet and the only one to be rounded by its own gravity (Park et al., 2016) with a confirmed detection of water vapor (Küppers et al., 2014). The estimated number of MBOs is around one million.

Beyond the asteroid belt are the Hilda asteroids which form a "triangle" and are in a 3:2 orbital resonance with Jupiter. Trojans are asteroids found on the same orbit as Jupiter at the L_4

and L_5 Lagrange points, which can be calculated solving the three-body problem. They can be divided into the Greeks at L_4 (in front of Jupiter) and the Trojans at L_5 (following Jupiter). The estimated number of Trojans is more than one million (Yoshida & Nakamura, 2005) with 588 Achilles being the first one that was discovered. Figure 1.1 shows the inner Solar System from the Sun up until Jupiter with the planets, the main belt, as well as the Trojans.

Located between the orbit of Jupiter and Neptune are the so-called Centaurs. With generally unstable orbits, their dynamical lifetimes are rather short and only of a few million years (Horner et al., 2004). The largest confirmed Centaur is 10199 Chariklo with a diameter of 260 km.

Farther out as the orbit of Neptune is the Kuiper Belt and the so-called scattered disk containing Kuiper Belt Objects (KBOs) and Scattered Disk Objects (SDOs) respectively, which are generally referred to as TNOs. The KBOs can be categorized further into the resonant and the classical ones. The resonant KBOs have mean motion resonances with Neptune, e.g., 2:3 or 1:2, while most of the classical population of KBOs are between those two mean motion resonances without being controlled by any orbital resonance with Neptune. An example for a classical KBO would be 2014 MU₆₉, also known as Arrokoth, which was visited by the New Horizons spacecraft on the 1st January 2019. The KBOs usually have small inclinations and eccentricities, while SDOs are very eccentric and show high inclinations with unstable orbits scattered by Neptune. The first discovered TNO was Pluto which was classified as a planet until 2006. Figure 1.2 shows the smaller bodies in the outer Solar System with the Centaurs, the KBOs, as well as the SDOs.

1.1.2 Properties

The properties and composition of small bodies depend on the location they were formed. If the body formed farther out in the Solar System, as the TNOs and Oort Cloud objects (comets), they contain a lot of volatile materials, e.g., ice. In contrast, bodies formed farther inwards like MBOs (asteroids) hold fewer ice and volatiles and are more rocky as a consequence. In terms of global composition, the objects closer to Earth are studied more thoroughly and are better understood than those at large distances. These are still in an early stage of investigation since observations are more difficult.

Taxonomic classes are defined by single letters. Bodies of classes A, K, L, O, Q, R, S, V, Xe, and Xk are considered bright whereas B, C, D, T, and Xc are dark. The three most common classes are:

- D-type: Objects of this type are considered to be the simplest and have ultra low albedo. They are rich in organics and volatile elements.
- C-type: This is the most common class of asteroids with around 75% of the known asteroids. They are primitive, carbon-, and volatile-rich.
- S-type: These are silicate (rocky) objects and they form the largest group in the inner part of the main belt (within 2.2 au) with primitive and volatile poor composition. They are the second most common type forming around 17%.

The most common asteroids in the outer main belt belong to the dark type (such as D- and C-type). They are considered to be the most primitive asteroids, suffering very little thermal

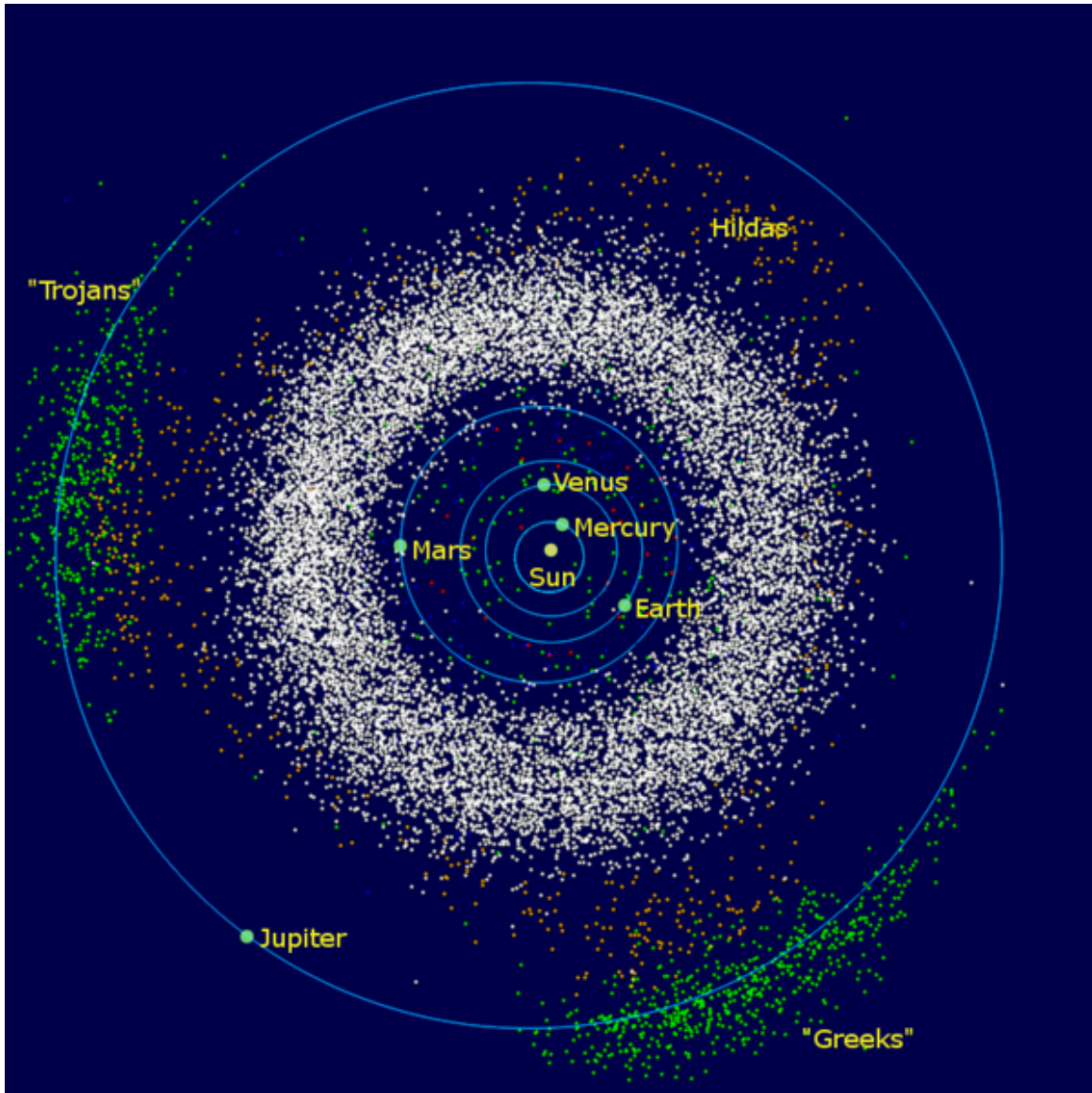


Figure 1.1: The inner Solar System ranging from the Sun to Jupiter. The white cloud represents the asteroid belt which is also called the main belt. The Hilda asteroids are shown in orange and form a "triangle" beyond the asteroid belt in a 3:2 orbital resonance with Jupiter. Jupiter's trojans are shown in green with the trailing "Trojans" and the leading "Greeks" (figure from Murray and Dermott, *Solar System Dynamics*, p. 107).

alteration and having a similar chemical composition as the Sun. The six most abundant elements are hydrogen, helium, carbon, nitrogen, oxygen, and neon. They usually have low albedos ($p \sim 0.05$) in contrast to high albedo objects, e.g., S-type with $p \sim 0.15$. Figure 1.3 shows the mass plotted against the density for different small bodies in our Solar System ranging from TNOs to different taxonomic classes of asteroids to comets. The taxonomy used here is based on wavelength range by DeMeo et al. (2009) which contains 15 classes that can be categorized into three complexes (C,S and X) with nine supplementary classes called end-members. Figure 1.4 presents a similar plot but with mass plotted against macroporosity. As one can easily see in these two plots, many objects possess a low density but a high macroporosity, reaching up to around 80% porosity and a huge bulk of small bodies have around 30 – 50%. Porosity in

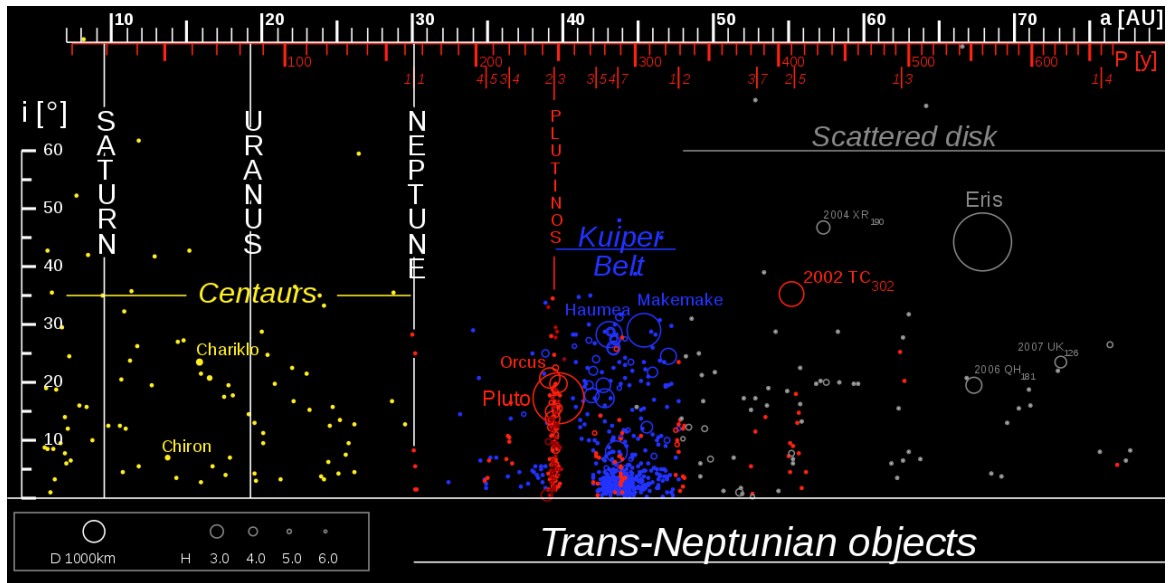


Figure 1.2: Inclination against semi-major axis for the outer Solar System ranging from around 5 au to 70 au. The centaurs are represented in yellow. Kuiper belt objects are shown in blue and red. Here, the classical Kuiper belt objects, or also called cubewanos, are blue while the resonant ones, also called plutinos, are red. SDOs are shown in grey. This figure was reproduced under the Creative Commons license.

small bodies is therefore not negligible.

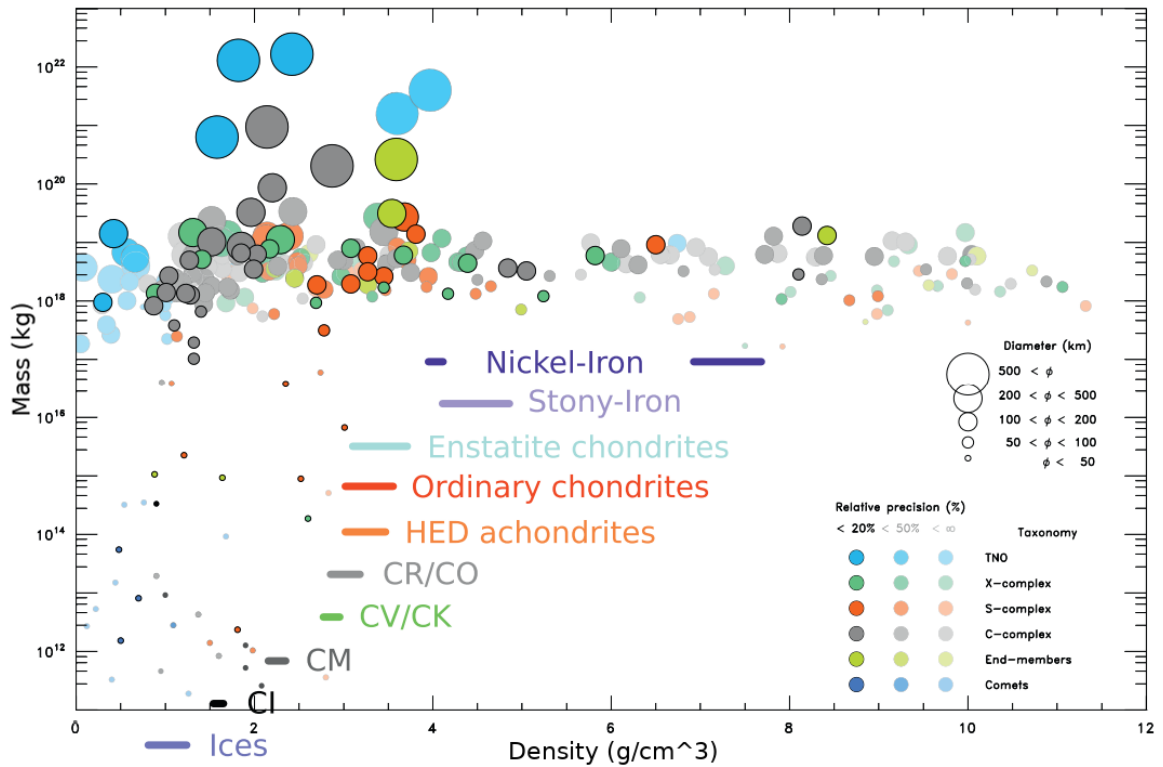


Figure 1.3: Mass against density with six different categories: TNOs (light blue), asteroids grouped into four taxonomic classes (X-complex in green, S-complex in red, C-complex in grey and end-members in yellow), and comets (blue). The sizes of the symbols refer to different diameters of the bodies. The relative accuracy is indicated by three different levels of transparency (20%, 50%, and regardless to the precision ($< \infty$)) (figure from Carry 2012).

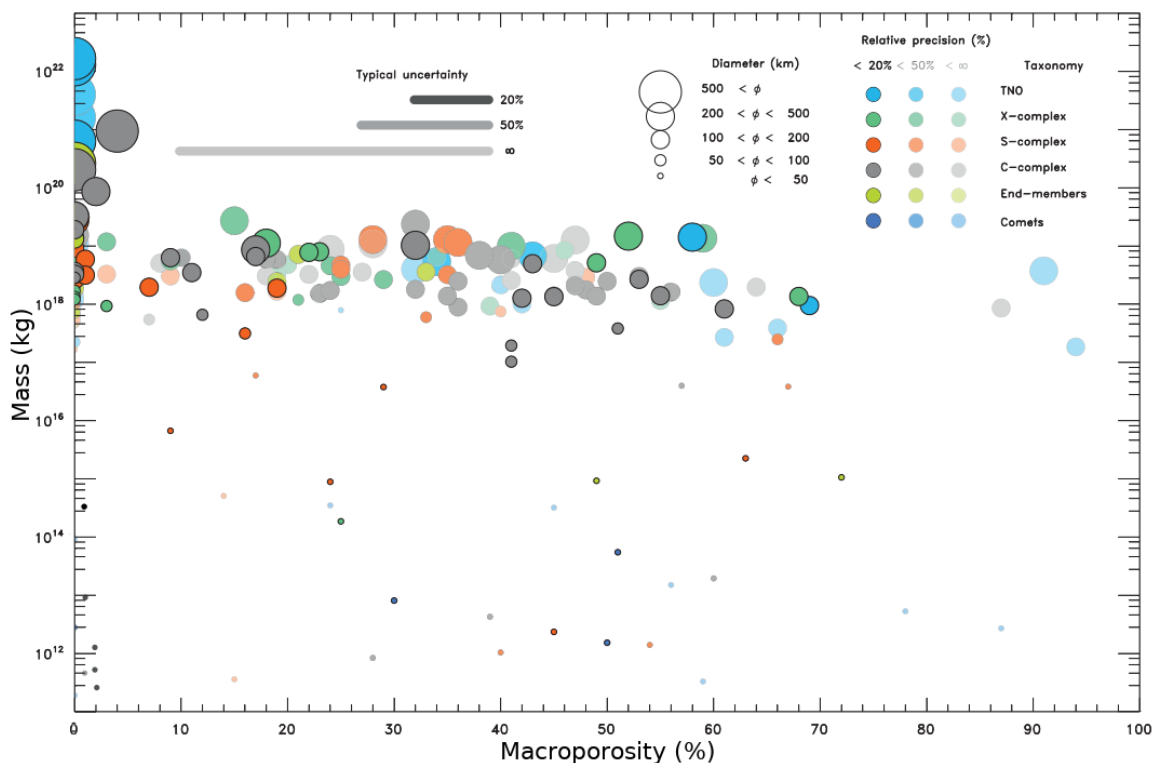


Figure 1.4: Mass against macroporosity with six different categories and five different sizes (see 1.3). The relative precision (20%, 50%, and $< \infty$) is indicated for each class with three transparency levels and the typical uncertainty in macroporosity is illustrated. Additionally, any value can get shifted by 30 – 40% due to erroneous asteroid-meteorite links (figure from Carry 2012).

1.2 Porous bodies

1.2.1 Observations and findings

Observational data regarding the structure, composition, and porosity of small bodies is increasing. It is believed that many bodies consist of rubble-piles with high degrees of porosity. For long it was suspected that small bodies have porous interiors (Chapman et al. 1977; Watson 1978) but measurements became possible only recently. Credible bulk density estimates for 22 asteroids have been obtained by spacecraft missions, as well as ground-based optical and radar observation techniques (Britt et al., 2002). Ten objects have densities less than 2000 kg/m^3 , five even less than 1500 kg/m^3 suggesting high degrees of porosity of up to 75%. The density of the majority indicates porosities in the range of 25 – 55%. Comets, for example, share the same or even higher degrees of porosity (Greenberg 1986; Sirono & Greenberg 2000).

Figures 1.5, 1.6, 1.7, 1.8, and 1.9 are examples of porous small bodies in our Solar System. The first figure (1.5) shows 9P/Tempel 1, which has been investigated by two spacecraft missions, Deep Impact and Stardust-NExT. The estimated bulk density is 470 kg/m^3 with a porosity of 75% (Thomas et al., 2013). Two types of terrain are present, a rough pitted and a smoother, flow-like material which is collected in low regions. The following figure (1.6) shows 25143 Itokawa, an asteroid which looks like two attached masses merged into a large lobe structure. Its surface is made up of a smooth zone of regolith and a bumpy area covered with many rocks (Saito et al., 2006). Its taxonomic class is S- or Q-type with a bulk density of 1900 kg/m^3 and a porosity of around 40% (Abe et al., 2006). The next figure (1.7) shows 67P/Churyumov-Gerasimenko, a Jupiter-family comet, that originated from the Kuiper-belt. The Rosetta spacecraft rendezvoused with Chury in 2014 and its lander "Philae" descended on the surface of the comet, which was the first spacecraft to land on a comet nucleus. With an average bulk density of 530 kg/m^3 and an averaged porosity of 70 – 75%, the nucleus is highly porous similar to that of comet Tempel 1 (Pätzold et al., 2016). Figure (1.8) illustrates 486958 Arrokoth which is, like Chury, a contact binary. It is the farthest ($a \approx 44.6 \text{ au}$) and most primitive object targeted by a space mission. In 2019, the New Horizons spacecraft made its flyby. The color of Arrokoth is redder compared to Pluto. Therefore, it is part of the "ultra red" population of cold KBOs. The presence of tholins is likely the cause, which indicates the existence of volatiles such as methane and ammonia (Stern et al., 2019). The estimated bulk density is 500 kg/m^3 with a porosity of around 50%. The surface shows only few and small craters suggesting very few impacts throughout its life. The last figure (1.9) shows the largest confirmed centaur, 10199 Chariklo. Astronomers discovered two rings around Chariklo by observing a stellar occultation, which makes it the first known minor planet with rings. Before, it was a general belief that rings could only be formed and contained by massive bodies. The rings are likely to contain water ice (Braga-Ribas et al., 2014).

1.2.2 Influence of porosity

In the previous section (1.1.2), the presence of high porosities has been shown in a large number of small bodies. The question is now: Does the porosity change the outcome for collisions or impacts of these objects? There have been many studies regarding this question and the short answer is "yes" (Housen & Holsapple 2003; Michikami et al. 2007). Porous material behaves



Figure 1.5: 9P/Tempel 1 with a radius of 2.83km showing a surface that consists of rough and smooth areas, which was deliberately struck by one component of the NASA Deep Impact probe (figure from NASA / Jet Propulsion Laboratory / University of Maryland).

differently compared to a material with the same low density but no porosity in the following ways:

- The ejecta mass is smaller the higher the porosity.
- A large amount of energy is transformed into heat due to the compaction of pore space.
- Crater depths increase with a larger porosity of the target.

The importance of porosity during collisions and impacts nowadays is a well-known fact. One cannot simply regard the material as non-porous and merely change the density of the material to a lower value and expect good results.

Due to the high presence of porosity in small bodies, it is important to know the influence of porosity on the collisional evolution. Spacecraft observations of asteroid Mathilde strongly

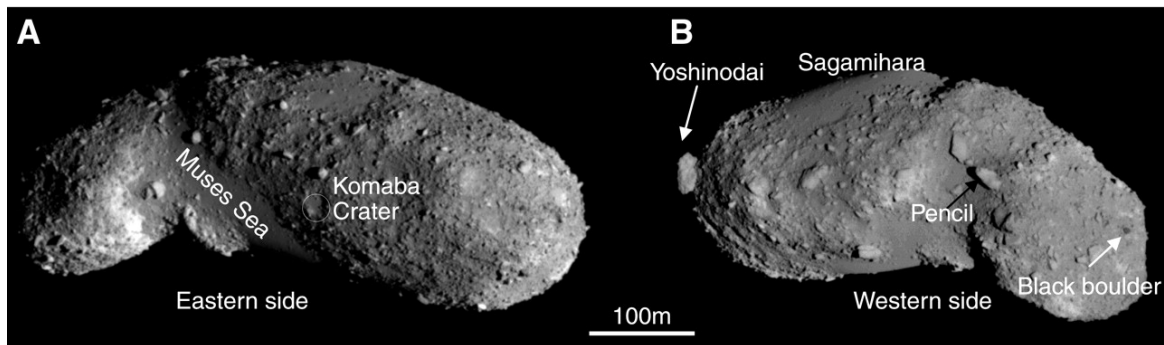


Figure 1.6: Itokawa is a sub-kilometer NEO of the Apollo group and a potentially hazardous asteroid. It has an elongated shape and is likely a rubble pile. The space probe Hayabusa was the first sample return mission ever with Itokawa as a target, it collected regolith dust particles from its surface (figure from Saito et al. 2006).



Figure 1.7: 67P Churyumov-Gerasimenko is made up of two lobes, the larger one with dimensions $4.1 \text{ km} \times 3.3 \text{ km} \times 1.8 \text{ km}$ and the smaller one with $2.6 \text{ km} \times 2.3 \text{ km} \times 1.8 \text{ km}$. The contact binary is likely the outcome of a soft, low-velocity collision of two bodies (figure from ESA/Rosetta/NAVCAM).

suggest that porosity has a big impact on crater formation, impact ejecta, catastrophic events, and so forth. Mathilde, a C-type asteroid with a size of $66 \text{ km} \times 48 \text{ km} \times 46 \text{ km}$, has a measured



Figure 1.8: Arrokoth is made up of two lobes, Ultima the larger one with dimensions $22\text{ km} \times 20\text{ km} \times 7\text{ km}$ and Thule the smaller one with $14\text{ km} \times 14\text{ km} \times 10\text{ km}$ (figure from ASA/Johns Hopkins University Applied Physics Laboratory/Southwest Research Institute).

bulk density of $\sim 1300\text{ kg/m}^3$ and a porosity of $\sim 50\%$ (Veverka et al. 1999; Britt et al. 2002). Collisions and impacts have always been and will always be shaping the faces of all solid bodies in each star system. They can range from μm up to hundreds of km sized objects. Different material and collision parameters have various influences on the outcome:

- Impact velocity: Slow collisions ($v \sim \text{cm/s}$) only slightly deform the bodies and hardly any fragmentation takes place. The deformation is mainly elastic and a negligible amount of energy is dissipated. For fast cases ($v \sim \text{km/s}$), the colliding bodies can shatter into small fragments with high amounts of dissipated energy and strong plastic deformations.
- Porosity: It is the ratio between the volume of the void spaces in the material and its total volume. Therefore, the more porous a material the more void spaces it has. During a collision, the material undergoes compaction and the void spaces get reduced while dissipating energy.
- Material strength: The higher the strength of a body the less deformation and fragmentation takes place.
- Body size: Large bodies have stronger gravitational forces and thus higher escape velocities. Therefore, the bodies hold together more easily during collisions since the particles are gravitationally bound.



Figure 1.9: Chariklo has an equivalent radius of 124 km, its two rings have orbital radii of 391 km and 405 km as well as optical depths of 0.4 and 0.6. They may originate from a debris disk, which is likely surrounded by kilometer-sized satellites. (figure from ESO/L. Calçada/M. Kornmesser/Nick Risinger).

1.3 Outlook

In the next chapter, we will give a general introduction to porosity. Chapter 3 introduces the numerical method SPH as well as more details regarding certain models, e.g., solid body physics or porosity. Chapter 4 contains all publications and puts them into the context of this thesis. In the last chapter, we will draw a conclusion regarding new possibilities with the code and the insights gained throughout the compilation of this thesis, as well as give an outlook about future work and improvements.

Porosity

Porosity Φ describes the fraction of void spaces V_v over the total volume V_{tot} resulting in $\Phi = V_v/V_{\text{tot}}$. Since the volume of the void spaces ranges from 0 to V_{tot} , the porosity ranges from 0 to 1 or, in terms of percentages, from 0% to 100%.

Porosity can be split mainly into two different types: macroporosity and microporosity. The first type, macroporosity, describes the void spaces in the material as actual holes. This is the case for large voids where the medium can no longer be considered isotropic and homogeneous with respect to fields of importance like the shock front. Therefore, the material is described consisting of areas with zero density (voids) and areas with densities that equal the matrix (solid) material. Microporosity describes a sub-resolution porosity for which the density of the material is reduced by a certain factor compared to the matrix material as material and void are indistinguishable. Thus, void spaces are homogeneous and isotropically distributed within the matrix material, and thereby the material has an overall lower density. Figure 2.1 shows the macroporosity on asteroid Itokawa with fine gravel and large boulders. Figure 2.2 depicts in picture (a) the porosity in perlite and sand as well as the highly porous nature of pumice demonstrated by a scanning electron microscope (SEM) of a single pumice particle in (b).

No matter the formation channel, a body will always contain a certain degree of porosity as long as it is not purely monolithic. Small bodies in our Solar System are porous, as mentioned previously in chapter 1.2.1. They can contain both micro- and macroporosity. Microporosity results from voids and pores surviving the early formation, as well as post-lithification fractures due to collisions. Macroporosity is represented by large-scale voids and fractures on the surface of small bodies, which are likely due to their impact history. The degree of macroporosity is an indication for their internal structure. For low porosity values they are solid, compact objects and for high values the objects are loosely combined, e.g., rubble piles held together by gravity (Richardson et al., 2002).

In addition, the importance and influence of porosity has been discussed in 1.2.2. We explained that the porosity is not negligible when it comes to crater formation, collisions and the resulting deformation.

We distinguish between two different velocity regimes regarding impacts. One is for very slow

impacts with velocities of some cm/s or m/s and the other is for very fast impacts with velocities in the range of hundreds of m/s up to km/s. The slow impacts occur in a protoplanetary disk between dust agglomerates. Their relative velocity results from Brownian motion, gas turbulences and differential drift motions, which depend on the size and density of the agglomerates (Weidenschilling & Cuzzi 1993 and Weidling et al. 2009). Another occurrence is the merging of asteroids in the Kuiper belt that form contact binaries. Billions of years ago, these collisions were probably much more prevalent due to most KBOs being on comparable orbits, which were more circular and close to the ecliptic. Nowadays, they are more scarce and also tend to be catastrophic because of their more elliptical and tilted orbits. This is exactly a scenario for high velocity impacts since these collisions tend to be in the regime of some km/s leading to high degrees of deformation and fragmentation. Of course, that is not only the case for objects in the Kuiper belt but also for the main asteroid belt.

This thesis researches porous bodies and pores in asteroids and comparable objects, which can be very small, even thinner than the shock front width. Therefore, we use a model that describes a sub-resolution porosity, which is explained in chapter 3.3 as well as in the publications. The porosity Φ is described using the volumes V_{tot} , V_v , and V_s as the total, the void, and the solid volumes, respectively. Together with the filling factor ϕ they are defined as follows

$$\Phi = \frac{V_v}{V_{\text{tot}}} \text{ and } \phi = \frac{V_s}{V_{\text{tot}}}. \quad (2.1)$$

The quantities are related via

$$\phi = \frac{V_s}{V_{\text{tot}}} = \frac{V_{\text{tot}} - V_v}{V_{\text{tot}}} = 1 - \frac{V_v}{V_{\text{tot}}} = 1 - \Phi. \quad (2.2)$$

With the porous density ρ and the solid density ρ_s , the filling factor reads

$$\phi = \frac{V_s}{V_{\text{tot}}} = \frac{V_{\text{tot}} - V_v}{V_{\text{tot}}} = \frac{\rho}{\rho_s}. \quad (2.3)$$

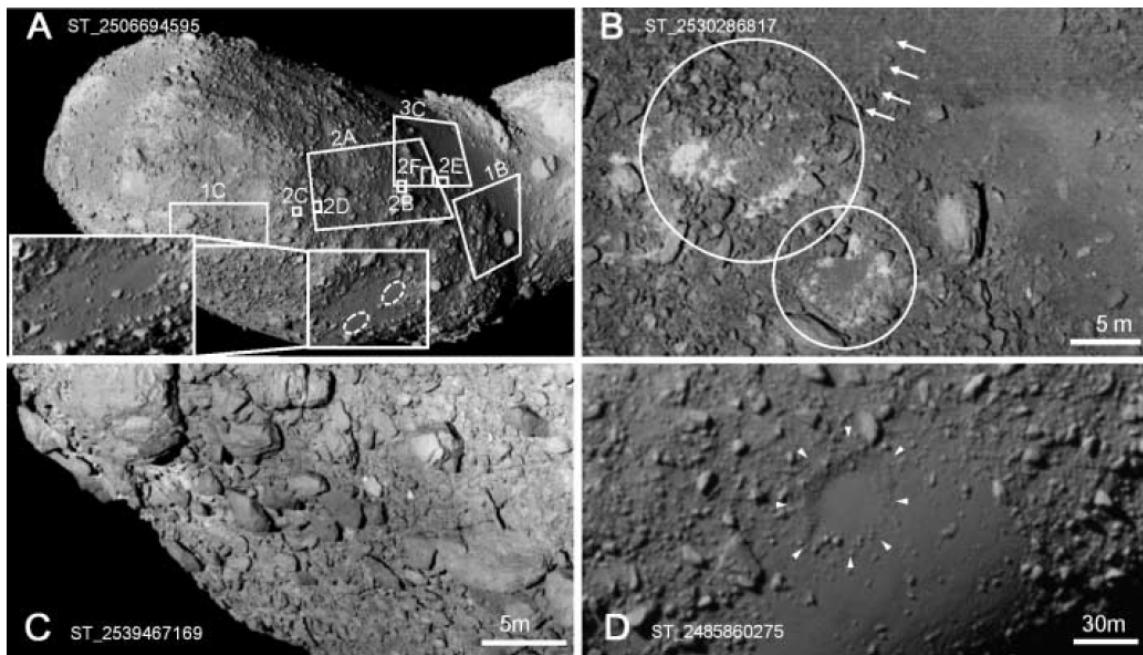


Figure 2.1: These four images show different kinds of porosities on Itokawa. A and B depict smooth terrain probably formed by one individual crater or a group of craters with fine and loose gravels filling them. C shows large, rounded boulders which are stably orientated against local gravity. The white triangles in D mark a crater candidate with the disrupted rim and flat floor (figure from Miyamoto et al. 2007).

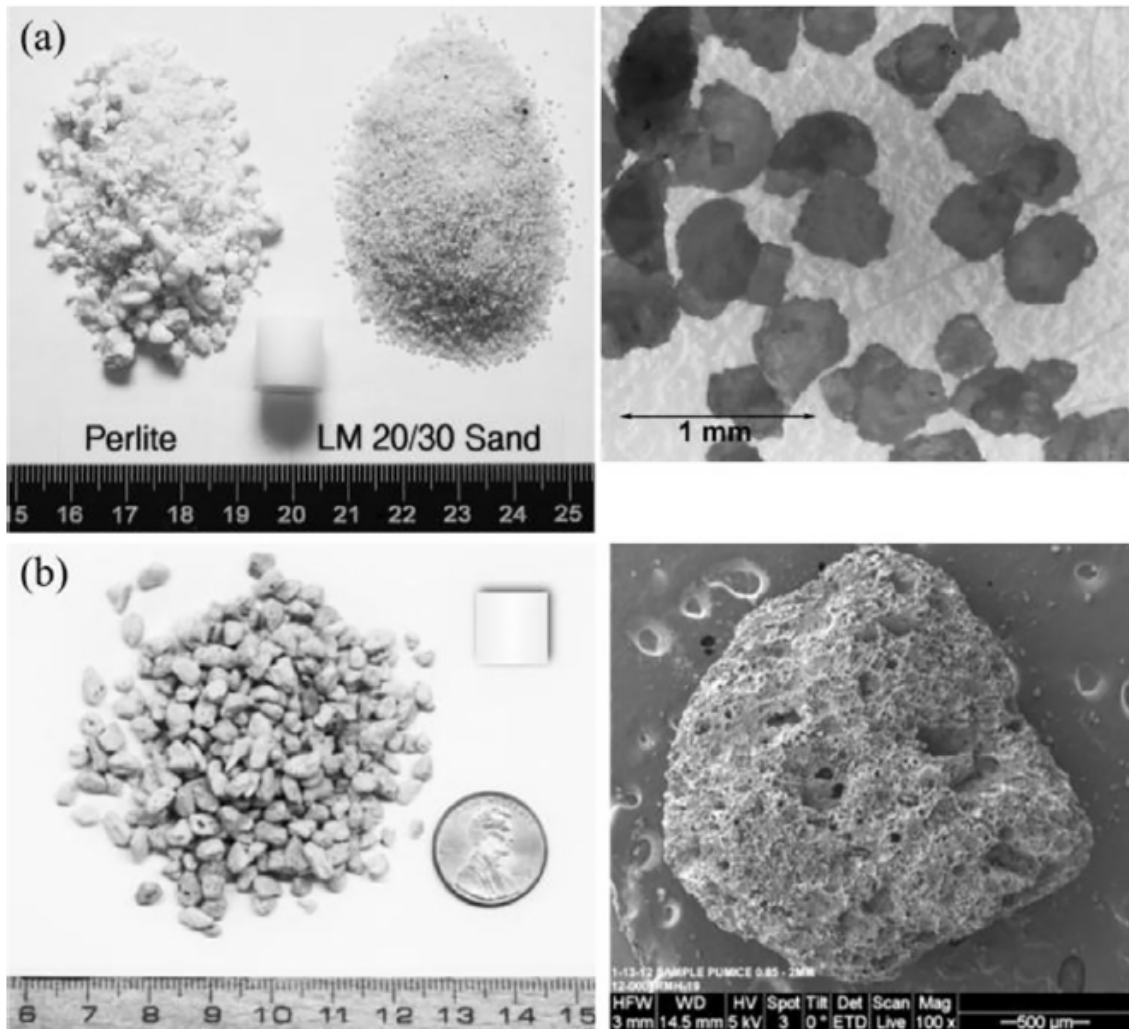


Figure 2.2: Examples of raw materials used in experiments by Housen et al. (2017). (a) Perlite and sand are mixed in a specific proportion in order to reach the desired porosity. The length scale is in cm, which is illustrated by a polyethylene cylindrical projectile. The figure to the right shows the angular nature of the Lane Mountain 20/30 sand. (b) The left side depicts granular pumice with sizes ranging from 2 to 4 mm. On the right side is a highly porous individual pumice particle shown with a SEM image (figure from Housen et al. 2017).

Numerics

This section introduces the numerical methods used for all simulations throughout this thesis. The strengths and weaknesses are described concisely. Most of the explanations of the schemes can be found in the publications and are referenced here.

3.1 Smooth Particle Hydrodynamics

Smooth Particle Hydrodynamics (SPH) is a numerical method to solve the hydrodynamic equations, which was first described by Lucy (1977) and Gingold & Monaghan (1977). It is a meshless Lagrangian particle method describing the fluid or solid body as many discretized, small mass packages. They can interact with each other and are called particles, but they are just the sampling points of the scheme and must not be mistaken for real particles. For example, the density at a certain coordinate \mathbf{x} is not only given by the contribution of the SPH particle at that coordinate but by all surrounding SPH particles. The contribution of every particle is weighted using the smoothing kernel W which will be introduced in eq. (3.2). The particles follow the Lagrangian equation of motion like point masses. They represent the fluid or solid body and thus contain important information like mass, density, pressure, and energy. Due to the fact that the particles move according to the equation of motion and are not bound by a grid, SPH is a very suitable scheme for complex geometries.

It was first used in astrophysics to solve the hydrodynamic equations for compressible flows. Nowadays, the method is used for a wide range of problems, e.g., to perform cosmological simulations, to simulate avalanches and granular media (Yu et al. 2018; Bui et al. 2008) or to tackle magneto-hydrodynamical problems (Price, 2012). The standard method was extended to include solid state mechanics (Libersky & Petschek 1991; Benz & Asphaug 1994). For further usage of the numerical method SPH and its fields of application see chapter 1 in Schäfer et al. (submitted).

In comparison to different numerical schemes, the SPH method provides various benefits (Speith, 2006) with the most relevant ones being:

- It is a very sturdy numerical scheme.
- Due to the meshless Lagrangian particle method, large deformations are handled easily.

- Breaking (e.g., of rocks) is modelled naturally by splitting particle groups.

The main drawbacks coming with this method are the following:

- The robustness unfortunately can cause problems due to non-physical effects, which can lead to instabilities but they do not crash the code.
- Compared to grid-codes the spatial resolution is generally lower.
- The level of noise is rather high compared to other numerical methods.

The main concept of this method is the construction of a set of ordinary differential equations from a set of partial differential equations (PDE). This is realized by using a kernel interpolation, in particular for the PDE of hydrodynamics.

Here, $f(\mathbf{x})$ is an arbitrary function at position \mathbf{x} , which can be expressed via the delta function $\delta(\mathbf{x})$ and reads

$$f(\mathbf{x}) = \int_V f(\mathbf{x}') \delta(\mathbf{x} - \mathbf{x}') d^3x'. \quad (3.1)$$

Approximating the function $f(\mathbf{x})$ leads to

$$\langle f(\mathbf{x}) \rangle = \int_V f(\mathbf{x}') W(\mathbf{x}, \mathbf{x}'; h) d^3x', \quad (3.2)$$

with the kernel function $W(\mathbf{x}, \mathbf{x}'; h)$ and the smoothing length h . The latter is a measure of the width of the kernel, thus representing the range of the interaction. The following relations have to be satisfied by the kernel function

$$\lim_{h \rightarrow 0} W(\mathbf{x}, \mathbf{x}'; h) = \delta(\mathbf{x} - \mathbf{x}'), \quad (3.3)$$

as well as

$$\int_V W(\mathbf{x}, \mathbf{x}'; h) d^3x' = 1. \quad (3.4)$$

It is advantageous to choose a spherically symmetric kernel function which reads

$$W(\mathbf{x}, \mathbf{x}'; h) = W(|\mathbf{x} - \mathbf{x}'|; h) = W(\tilde{r}; h), \quad (3.5)$$

with \tilde{r} denoting the distance between the positions \mathbf{x} and \mathbf{x}' . If the spherically symmetric kernel converges fast to zero for large \mathbf{x}' , then it satisfies the following two equations

$$\int_V \nabla' W(\tilde{r}; h) d^3x' = 0, \quad (3.6)$$

and

$$\nabla W(\tilde{r}; h) = -\nabla' W(\tilde{r}; h). \quad (3.7)$$

These equations allow for the approximation of partial derivatives of a function f

$$\left\langle \frac{\partial f(\mathbf{x})}{\partial x_\alpha} \right\rangle = \int_V f(\mathbf{x}') \frac{\partial W(\tilde{r}; h)}{\partial x_\alpha} d^3x'. \quad (3.8)$$

Due to the fact that the function f in most cases is only given as numbers at some discrete points in space, the integration is only solvable numerically. Thus, the approximation of the integral is given by a sum calculated at discrete values with weighting factors. This results in the summation over all SPH particles. The particle density n can be defined as

$$n(\mathbf{x}) := \sum_{j=1}^{N_p} \delta(\mathbf{x} - \mathbf{x}_j), \quad (3.9)$$

where N_p is the number of randomly distributed particles with positions \mathbf{x}_j and functions $f(\mathbf{x}_j)$ as well as the index $j = [1, \dots, N_p]$. Using the characteristics of the kernel, the limit of the particle density for a vanishing smoothing length can be written in the following way

$$\lim_{h \rightarrow 0} \langle n(\mathbf{x}') \rangle = \lim_{h \rightarrow 0} \sum_{j=1}^{N_p} W(\mathbf{x}', \mathbf{x}_j; h) = n(\mathbf{x}'). \quad (3.10)$$

Thus, $n(\mathbf{x}') / \langle n(\mathbf{x}') \rangle$ is an approximation of 1 (Laguna, 1995). Now, we can execute the integration for eq. (3.2) and eq. (3.8). As a result, approximating $f(\mathbf{x})$ gives

$$\langle f(\mathbf{x}) \rangle = \sum_{j=1}^{N_p} \frac{f(\mathbf{x}_j)}{\langle n(\mathbf{x}_j) \rangle} W(\mathbf{x}, \mathbf{x}_j; h). \quad (3.11)$$

Introducing the particle mass m_j as

$$m_j := \frac{\rho_j}{\langle n_j \rangle}, \quad (3.12)$$

where n is the particle density and ρ the mass density, simplifies this further. Finally, the following equation is obtained

$$f_i = \sum_j \frac{m_j}{\rho_j} f_j W_{ij}(h), \quad (3.13)$$

with its partial derivative

$$\frac{\partial f_i}{\partial x_i^\alpha} = \sum_j \frac{m_j}{\rho_j} f_j \frac{\partial W_{ij}(h)}{\partial x_i^\alpha}, \quad (3.14)$$

using the common abbreviations $f_i = f(\mathbf{x}_i)$ and $W_{ij}(h) = W(\mathbf{x}_i, \mathbf{x}_j; h)$. The summation is not over all particles but just the respective interaction partners of particle i . For a more elaborated explanation and derivation look, e.g., into Schäfer (2005) or Speith (1998).

3.1.1 Hydrodynamic equations

In this part, we present and explain the important hydrodynamical equations and their representations in the SPH formalism.

The density can be calculated with the SPH sum (3.13) and $f_i = \rho_i$ via the simple form

$$\rho_i = \sum_j m_j W_{ij}. \quad (3.15)$$

The particles residing on the edges of a solid body have less interaction partners, which leads to a lower density for particles with fixed smoothing lengths. However, this is problematic since the Tillotson or Murnaghan equation of state (EOS) calculates the pressure p using the ratio of the density ρ and the initial density ρ_0 . Thus, $p = 0$ is only the case for one density. The pressure for the particles on the edges would not vanish, effectively leading to a force. Therefore, the body would not be in a stable state. In order to avoid this, the continuity equation is integrated using the SPH scheme.

Continuity equation

The continuity equation describes the conservation of mass and reads in Lagrangian form

$$\frac{d\rho}{dt} + \rho \nabla \cdot \mathbf{v} = 0. \quad (3.16)$$

The formulation by Randles & Libersky (1996) is as following

$$\frac{d\rho_i}{dt} = -\rho_i \sum_j \frac{m_j}{\rho_j} \mathbf{v}_j \cdot \nabla_i W_{ij}(h). \quad (3.17)$$

After adding a zero to the right-hand side, we obtain the continuity equation that is used throughout this thesis for solid body simulations

$$\frac{d\rho_i}{dt} = -\rho_i \sum_j \frac{m_j}{\rho_j} (\mathbf{v}_j - \mathbf{v}_i) \cdot \nabla_i W_{ij}(h). \quad (3.18)$$

Conservation of momentum

The Euler equation represents the conservation of momentum. In Lagrangian formalism and without an external force, it is represented by the following equation

$$\frac{d\mathbf{v}}{dt} = -\frac{1}{\rho} \nabla p. \quad (3.19)$$

Using some general relations and applying the SPH formalism, it follows

$$\frac{d\mathbf{v}_i}{dt} = -\sum_j m_j \left[\frac{p_i}{\rho_i^2} + \frac{p_j}{\rho_j^2} \right] \nabla_i W_{ij}(h). \quad (3.20)$$

Conservation of internal energy

The following equation conserves the specific internal energy u

$$\rho \frac{du}{dt} = -p \nabla \cdot \mathbf{v}. \quad (3.21)$$

Translating it into the SPH formalism leads to the following equation

$$\frac{du_i}{dt} = \frac{1}{2} \sum_j m_j \left[\left(\frac{p_i}{\rho_i^2} + \frac{p_j}{\rho_j^2} \right) \right] (v_i^\alpha - v_j^\alpha) \frac{\partial W_{ij}(h)}{\partial x_i^\alpha}. \quad (3.22)$$

3.1.2 Solid body mechanics

The perfectly elastic behaviour of a solid body is based on Hooke's law and the implemented basic equations are presented in chapter 2.3 in Schäfer et al. (submitted) and chapter 2.2 in Wandel et al. (2017) following the concepts and ideas of Stellingwerf & Wingate (1994) and Benz & Asphaug (1994).

3.2 Physical and numerical models

This section shortly describes the other models included in our simulations, which are mentioned for the sake of completeness and are described in more detail in the aforementioned publications.

3.2.1 Equation of state

An EOS gives a relation between the thermodynamic state variables and completes the system of PDEs. It relates the pressure, density, and temperature or internal energy of a specific material. For different physical problems and simulations, various EOS are applied since no EOS can be used universally for all materials under all circumstances. Following EOS are available: liquid EOS, the Murnaghan EOS, the Tillotson EOS, a polytropic gas EOS, an isothermal gas EOS, an ideal gas EOS as well as ANEOS. For a more detailed description see chapter 2.6 in Schäfer et al. (submitted).

3.2.2 Strength models

Perfectly elastic behaviour of solid bodies is not realistic in many cases. The deformation becomes plastic as soon as the applied strain surpasses the elastic limit. We have three different plasticity models at our disposal for different simulations, which are the von Mises yield stress model, the Drucker-Prager yield and the Mohr-Coulomb yield criterion, as well as a pressure dependent yield stress combined with the fragmentation model. They are described in chapter 2.4 in Schäfer et al. (submitted).

3.2.3 Fragmentation model

We use the Grady-Kipp fragmentation model to treat fracture and brittle failure (Grady & Kipp 1980 and Benz & Asphaug 1995). It is based on flaws which are assigned to the SPH particles throughout the body. They follow a Weibull distribution with parameters that depend on the material. More details can be found in chapter 2.3 in Wandel et al. (2017). This model is solely for tensile damage but due to porosity and the compaction coming along with it, a compression part is added and presented in chapter 2.4 in Wandel et al. (2017).

3.3 Porosity models

Three porosity models have been implemented into our graphics processing unit (GPU) SPH code `miluphcuda` (Schäfer et al., submitted). These models describe the porosity on a microscopic level with pore sizes below the spatial resolution. This implies that there are no real voids inserted into the initial distribution but instead we have an isotropic and homogeneous porosity.

The three porosity models are:

- The P - α model by Herrmann (1969), which was later modified by Jutzi et al. (2008). The underlying idea behind this model is to divide the change in volume within a porous material into two parts: on the one side is the pore collapse of the porous material and on the other there is the compression of the solid matrix material. Hence, we introduce a so called distention parameter $\alpha = \rho_s/\rho$ calculating the porous pressure P from the solid pressure P_s with $P = 1/\alpha \cdot P_s(\alpha\rho, u)$. A short description can be found in chapter 2.5.1 in Schäfer et al. (submitted) and a more detailed one in chapter 2.4 in Wandel et al. (2017).
- The ϵ - α model, for which the main difference to the above mentioned model lies in the calculation of α (Collins et al., 2011). Instead of the pressure it uses the volumetric strain ϵ_V , thus removing the iterative nature of the P - α model. The volumetric strain is given by dividing the change in volume by the initial volume for small changes. It is used in the same research field as the P - α model and can be easily used with ANEOS, which is an analytical equation of state for shock physics codes. This model is explained in chapter 2.5.2 in Schäfer et al. (submitted).
- The Sirono model by Sirono (2004) and later modified by Geretshauser et al. (2010). This model is limited to isothermal compression, thus to a low velocity regime of up to some m/s, and is described in chapter 2.5.3 in Schäfer et al. (submitted).

Publications

All publications composed in the context of this thesis are presented in the following chapter. The publications consist of various studies regarding porous small bodies in our Solar System. They strongly differ in the velocity of the collision and the size ratio of the two bodies. We also vary the porosity as well as the material strengths accordingly. Therefore, a large field of small body collisions have been studied in this work resulting in the following publications, which were reproduced with the respective permissions:

- Wandel, O. J., Schäfer, C. M. and Maindl, T. I.: Collisional fragmentation of porous objects in planetary systems. In T. I. Maindl, H. Varvoglis & R. Dvorak (Eds.) *The First Greek-Australian Workshop on Extrasolar Planetary Systems*, (pp. 225-242) (2017).
- Haghighipour, N., Maindl, T. I., Schäfer, C. M. and Wandel O. J.: Triggering the Activation of Main-belt Comets: The Effect of Porosity. *The Astrophysical Journal*, 855(1), 60 (2018). <http://dx.doi.org/10.3847/1538-4357/aaa7f3>.
- Grishin, E., Malamud, U., Perets, H. B., Wandel O. and Schäfer C. M.: The wide-binary origin of (2014) MU69-like Kuiper belt contact binaries. *Nature*, 580(7804), 463-466 (2020). <https://doi.org/10.1038/s41586-020-2194-z>.
- Schäfer, C. M., Wandel, O. J., Burger, C., Maindl, T. I., Malamud, U., Buruchenko, S. K., Sfair, R., Audiffren, H., Vavilina, E. and Winter, P. M.: A Versatile Smoothed Particle Hydrodynamics Code for Graphic Cards. *Astronomy & Computing* (submitted).

Wandel et al. (2017) present an introduction to the SPH formalism, the implementation of the P - α porosity model into the code, as well as a study regarding the formation of crater Stickney on the Mars moon Phobos. Phobos is simulated as an ellipsoid made up of porous basalt, whereas the impactor is a slightly porous basalt sphere with a radius of the order of some hundred meters. The study includes high impact velocities v_{imp} between 6.5 km/s and 8.5 km/s (all super-sonic) as well as a selection of impactor radii r_{imp} , impact angles, and porosities. The high impact velocities in combination with a relatively big projectile, in comparison to the target, leads to a large crater.

This paper was written in collaboration with Christoph M. Schäfer and Thomas I. Maindl. All

simulations were conducted by myself, as well as the main parts of the analysis, the interpretation and the composition of most parts of the manuscript. Christoph M. Schäfer and Thomas I. Maindl contributed to all parts of the publication. The former concentrated mainly on the analysis and conclusion section and the latter on the scientific ideas.

In Haghighipour et al. (2018), we investigate impacts into MBCs and thus the possibility to trigger their activation. The target (MBC) is km-sized with a m-sized impactor. Four different simulation cases have been carried out:

- A rocky and non-porous target.
- A non-porous target with 50% water-mass fraction of non-porous ice.
- A rocky and porous target with 50% porosity.
- A 50% porous target containing 50% water-mass fraction of 50% porous ice.

The impactor and the solid part of the target are regarded as basalt. Impact velocities are in the range of some km/s, since the mean impact velocity in the main belt is ~ 5.3 km/s (Bottke et al., 1994). Due to the high impact velocities, the deformation is mainly in the plastic regime. This paper was written in collaboration with Nader Haghighipour, Thomas I. Maindl, and Christoph M. Schäfer. Most of the simulations were done by myself, the other simulations by Thomas I. Maindl. The publication was mainly written by Nader Haghighipour with exceptions to the section about SPH simulations and initial set-up, which was written by myself. The section about the results were mainly written by Christoph M. Schäfer and Thomas I. Maindl. The analysis and interpretation of the simulations were mostly done by Thomas I. Maindl and myself.

Grishin et al. (2020) is the third paper of this thesis and has recently been published in Nature. We point out the possibility of forming contact binaries, e.g., the KBO MU₆₉, through semi-secular Lidov-Kozai oscillations. This formation channel is able to explain such slightly deformed objects due to the very slow and gentle merging of two objects. In our example, the two objects Ultima and Thule that make up MU₆₉ are simulated as ellipsoids. They collide in a velocity range around their combined escape velocity of ~ 4.42 m/s. Therefore, we have a very slow (subsonic) collision and the deformation happens mainly in the elastic regime.

This publication was written in collaboration with Evgeni Grishin, Uri Malamud, Hagai B. Perets, and Christoph M. Schäfer. Evgeni Grishin led the project and performed the analytic calculations, as well as ran and analysed the N-body simulations. Uri Malamud had the leading role in the hydrodynamical modelling as well as its analysis and wrote most of the hydrodynamical section. Hagai B. Perets initiated and supervised the publication. The main ideas and concepts for this project was from him and he took part in all of the analysis. I conducted the hydrodynamical simulations, as well some parts of the analysis afterwards. Christoph M. Schäfer supervised the hydrodynamical simulations and is the main developer of the code used for the simulations. The main text of the publication was written by Evgeni Grishin and Hagai B. Perets.

In Schäfer et al. (submitted), we present an updated version of our GPU SPH code `miluphcuda` together with validation calculations, examples, and possible scenarios that the code can handle. The SPH method is explained further regarding solid body mechanics and the different

strength models. We also discuss the Tillotson equation of state that is used throughout this thesis.

This publication was written in collaboration with Christoph M. Schäfer, Christoph Burger, Thomas I. Maindl, Uri Malamud, Sergey K. Buruchenko, Rafael Sfair, Hugo Audiffren, Evita Vavilina, and Philip M. Winter. Christoph M. Schäfer led the project, had the main ideas and concepts, did a lot of validation simulations as well as calculations and wrote the main text. The text about the porosity models as well as the simulations and analysis of them was done by myself. I also contributed to most parts of the publication especially to the first three sections. The text, the simulations for the direct N-body - SPH hybrid section, as well as the formation of massive exomoons of super-terrestrial exoplanets were conducted by Christoph Burger. Thomas I. Maindl contributed to the whole project and is one of the main developers. Sergey K. Buruchenko wrote the section about high-speed dynamics and conducted the simulations for this part. Rafael Sfair wrote the text about ring structures around Chariklo and Haumea and did the simulations for this section. Hugo Audiffren wrote the section about circumbinary disk evolution and did the simulations mentioned there. Evita Vavilina contributed to the review and some editing parts. Philip M. Winter wrote the section about the viscously spreading ring.

Collisional fragmentation of porous objects in planetary systems

O. J. WANDEL¹, C. M. SCHÄFER¹ AND T. I. MAINDL²

¹Eberhard Karls Universität Tübingen, Institut für Astronomie und Astrophysik, Auf der Morgenstelle 10, 72760 Tübingen, Germany
email: oliver.wandel@student.uni-tuebingen.de

²University of Vienna, Department of Astrophysics, Türkenschanzstr. 17, 1180 Vienna, Austria

Abstract. We investigate the formation of the crater Stickney on the Mars moon Phobos. With 9 km in width, Stickney is the largest crater on Phobos. Our goal is to tighten the parameter space regarding the possible scenarios to form Stickney. Therefore, we performed Smooth Particle Hydrodynamics (SPH) simulations with varying impact velocity, impact angle, radius of the impactor as well as the degree of porosity. Our simulations show that the impactor radius r_p was smaller than 500 m. They further indicate, that the impactor was very likely around 300 m to 400 m with an impact velocity v_p between 6.5 km/s and 8.5 km/s. In addition, our results point to a porosity of around 25%. Regarding the topology of Stickney and our simulations, the impact angle was most likely rather steep.

Keywords. simulations: numerical, porosity, crater, impact, Phobos, Stickney

1 Introduction

Phobos is the larger (26.1 km × 22.8 km × 18.3 km, Willner et al. 2014) and inner (\approx 6200 km from the Mars surface) one of the two satellites orbiting Mars. Its origin is rather uncertain. With its density, shape and spectral characteristics being similar to primitive C-type asteroids (Thomas D. Jones et al., 1990) it was proposed that Phobos had its origin in the middle or outer Main Belt (Veverka et al., 1978). With regard to the dynamics it is challenging to explain how asteroids can get permanently captured into an orbit around Mars. Thus, Giuranna et al. (2011) proposed that Phobos formed in-situ and has been orbiting Mars since its formation. Phobos is exposed to strong tidal forces and experiences some dynamical friction, implying that its current orbit is unstable and continues to shrink, which leads to the conclusion that Phobos was in a higher orbit in the past (Burns, 1978). With all these uncertainties of the dynamical history of Phobos, Schmedemann et al. (2014) suggested two extreme cases with

the one case being the scenario where Phobos has been in its current orbit since its formation and the other case in which Phobos was captured by Mars recently. To describe the two cases, different impact velocities were assumed. For the first case the impact velocity was ≈ 8.5 km/s and for the second case it was ≈ 5.3 km/s.

Phobos' leading hemisphere is dominated by the considerably largest crater on the surface, Stickney, with a diameter of roughly 9 km. Therefore, Stickney is of the order of Phobos' effective radius. In this work we model the formation of the impact crater Stickney using the SPH code `miluphcuda` (Schäfer et al., 2016). Specifically we consider different scenarios (impact velocity v_p , impact angle ϕ , radius of the impacting projectile r_p and degree of porosity) that could form the well-studied crater in order to gain more insight about the scenario and settings needed to form Stickney. We are also interested in the impact geometry and we want to improve our understanding on the formation of large craters on small bodies. Furthermore, simulation results could help in discriminating between multiple hypotheses that have been suggested to explain the origin of Phobos.

2 Model

The simulations in this work were performed with the SPH code using 700.000 particles in 3D. For calculating the pressure we use the Tillotson equation of state (EOS) (Tillotson, 1962) with material parameters from Benz & Asphaug (1999) and the initial densities $\rho_{0,t} = 2350$ kg/m³ for Phobos and $\rho_{0,p} = 2500$ kg/m³ for the impactor. Fragmentation is included using the damage model by Grady & Kipp (1980) with an additional part coming from the porosity to include fracture during compression (see Section: 2.4). A simple strength model which is widely used to describe plasticity (Mises, 1913) is used. Phobos being between 25% and 35% porous (Andert et al., 2010), as well as the impactor being an estimated 10% porous (derived from the average meteorite types Britt et al. 2002), it is unavoidable to use a porosity model. Therefore, to describe porous material we include the modified P - α model by Jutzi et al. (2009). It models porosity on a microscopic scale giving every SPH particle an individual porosity.

Throughout this paper, the Einstein summation rule is used, Greek indices denote spatial coordinates and run from 1 to 3.

2.1 Hydrodynamic equations

2.1.1 Continuity equation

The continuity equation describes the conservation of mass and reads in Lagrangian form

$$\frac{d\rho}{dt} + \rho \frac{\partial v^\kappa}{\partial x^\kappa} = 0, \quad (1)$$

where ρ represents the density and \mathbf{v} the velocity of the solid body or fluid.

2.1.2 Conservation of momentum

The conservation of momentum in continuum mechanics for a solid body in Lagrangian form is represented by the following equation

$$\frac{dv^\kappa}{dt} = \frac{1}{\rho} \frac{\partial \sigma^{\kappa\lambda}}{\partial x^\lambda}, \quad (2)$$

where $\sigma^{\kappa\lambda}$ denotes the stress tensor given by the pressure P and the deviatoric stress tensor $S^{\kappa\lambda}$

$$\sigma^{\kappa\lambda} = -P\delta^{\kappa\lambda} + S^{\kappa\lambda}, \quad (3)$$

with the Kronecker delta $\delta^{\kappa\lambda}$.

2.1.3 Conservation of internal energy

The following equation conserves the specific internal energy u

$$\frac{du}{dt} = -\frac{P}{\rho} \frac{\partial v^\kappa}{\partial x^\kappa} + \frac{1}{\rho} S^{\kappa\lambda} \dot{\epsilon}^{\kappa\lambda}, \quad (4)$$

where $\dot{\epsilon}^{\kappa\lambda}$ is the strain rate tensor for small deformations

$$\dot{\epsilon}^{\kappa\lambda} = \frac{1}{2} \left(\frac{\partial v^\kappa}{\partial x^\lambda} + \frac{\partial v^\lambda}{\partial x^\kappa} \right). \quad (5)$$

2.2 Constitutive equations

The elastic behavior of a solid body is based on Hooke's law and leads in three dimensions to

$$S^{\kappa\lambda} \approx 2\mu \left(\epsilon^{\kappa\lambda} - \frac{1}{3} \delta^{\kappa\lambda} \epsilon^{\gamma\gamma} \right), \quad (6)$$

with the material dependent shear modulus μ and the strain tensor $\epsilon^{\kappa\lambda}$. The time evolution can then be written as follows

$$\frac{d}{dt}S^{\kappa\lambda} = 2\mu \left(\dot{\epsilon}^{\kappa\lambda} - \frac{1}{3}\delta^{\kappa\lambda}\dot{\epsilon}^{\gamma\gamma} \right) + \text{rotation terms.} \quad (7)$$

The rotation terms are needed since the constitutive equations have to be independent from the material frame of reference. There are various possibilities to achieve this. The usual approach for particle codes is the Jaumann rate form. The rotation terms of the Jaumann rate form are

$$S^{\kappa\gamma}R^{\gamma\lambda} - R^{\kappa\gamma}S^{\gamma\lambda}, \quad (8)$$

with the rotation rate tensor

$$R^{\kappa\lambda} = \frac{1}{2} \left(\frac{\partial v^\kappa}{\partial x^\lambda} - \frac{\partial v^\lambda}{\partial x^\kappa} \right). \quad (9)$$

2.3 Damage model for brittle material

The tension damage model we use was developed by Grady & Kipp (1980) and is based on the presence of incipient flaws in the material and on crack propagation under increasing strain. If an applied force on a solid brittle body is large enough, the atomic bonds can break and the material begins to fracture and develop cracks. The active flaws are distributed using the Weibull distribution (Weibull, 1939)

$$n(\epsilon) = k\epsilon^m, \quad (10)$$

where n is the number of flaws per unit volume with failure strains lower than ϵ and the two Weibull parameters k and m . Common values for basalt are $k = 10^{61} \text{ m}^{-3}$ and $m = 16$ (Nakamura et al., 2007). The scalar parameter damage D is 0 for undamaged material and 1 for fully damaged material that can not undergo any tension or deviatoric stress. Damage reduces the strength under tensile loading and shear and the stress tensor $\sigma^{\kappa\lambda}$ is decreased by the factor $(1 - D)$

$$\sigma^{\kappa\lambda} = -P\delta^{\kappa\lambda} + (1 - D)S^{\kappa\lambda}, \quad (11)$$

where the pressure P is also reduced by $(1 - D)$ but only for $p < 0$ since this only applies for tensile forces.

2.4 Porosity

The implemented porosity model is the so called $P - \alpha$ model (Herrmann, 1969) which was modified by Jutzi et al. (2009). The concept behind the $P - \alpha$ model is the separation of the volume change in a porous material into the pore collapse of the porous material and the compression of the matrix material. The distention is defined by following equation

$$\alpha = \frac{\rho_s}{\rho} = \frac{1}{1 - \Phi}, \quad (12)$$

where ρ is the density of the porous material, ρ_s the density of the corresponding matrix material and Φ the porosity. We gain the pressure of the porous material using the empirically found equation using the distention α and the pressure of the solid material P_s (Carroll & Holt, 1972)

$$P = \frac{1}{\alpha} P_s(\rho_s, E_s) = \frac{1}{\alpha} P_s(\alpha\rho, E), \quad (13)$$

where ρ_s and E_s are the density and the energy of the solid and ρ and E of the porous material. The last equation is gained using Eq. 12 and the assumption that the energy of the surface pores are neglected and therefore the energy of the porous material equals that of the solid material ($E = E_s$).

The pressure is a function of the density, the energy and the distention $P(\rho, E, \alpha)$ and is calculated with the Tillotson EOS (Tillotson, 1962).

Normally, the change of the distention is divided into two parts: on the one hand the elastic part where the change of the distention is reversible, and on the other hand the plastic part with an irreversible change. For the elastic regime the distention changes only slightly and therefore $d\alpha/dP$ is often assumed to be zero. If not mentioned otherwise, the elastic change of the distention with regard to the pressure is set to zero. In the plastic regime the distention α is computed

$$\alpha(P) = \begin{cases} (\alpha_e - \alpha_t) \frac{(P_t - P)^{n_1}}{(P_t - P_e)^{n_1}} + (\alpha_t - 1) \frac{(P_s - P)^{n_2}}{(P_s - P_e)^{n_2}} + 1 & \text{if } P_e < P < P_t \\ (\alpha_t - 1) \frac{(P_s - P)^{n_2}}{(P_s - P_e)^{n_2}} + 1 & \text{if } P_t \leq P < P_s \\ 1 & \text{if } P \geq P_s, \end{cases} \quad (14)$$

where P_e is the pressure where the transition from the elastic to the plastic regime happens, P_s the pressure where the porous material is fully compacted and the density equals the matrix density, resulting in $\alpha = 1$, and the pressure P_t indicates a transition between the two regimes with different slopes n_1 and n_2 (Jutzi et al., 2009). The distentions α_e and α_t correspond to the points where the pressure equals P_e and P_t , respectively. The parameters were gained through the fitting of the function to the crush-curve

Table 1. Parameter table of the crush-curve fitted to the experiment.

P_e [N/m ²]	P_t [N/m ²]	P_s [N/m ²]	α_0	α_t	n_1	n_2
1.0×10^6	6.80×10^7	2.13×10^8	4.64	1.90	12	3

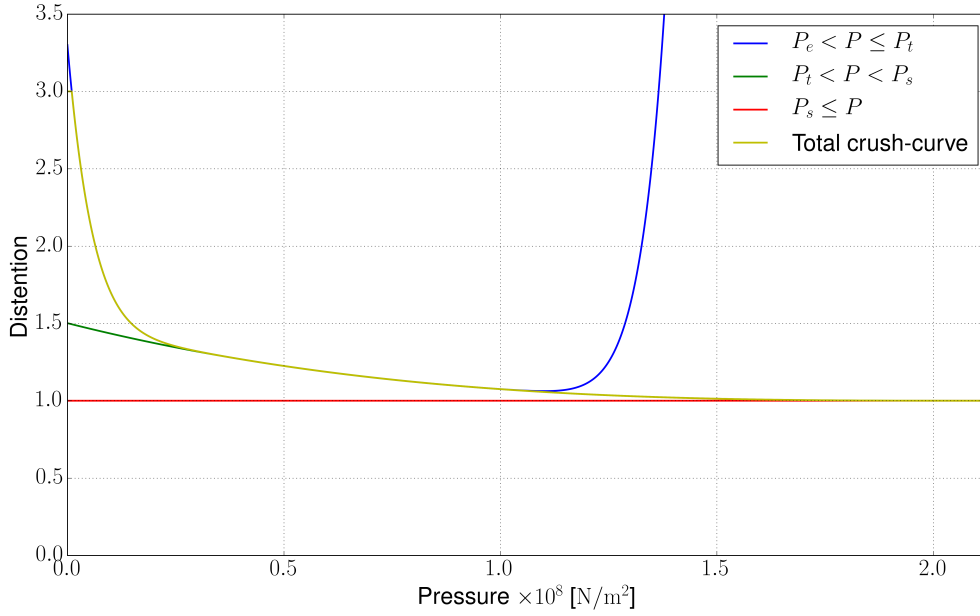


Figure 1. Relation between the distention α and the pressure P . The three regimes of the crush-curve as well as the total crush-curve for an initial distention of $\alpha_0 = 3.0$ is shown. The blue line shows the regime for a pressure P between P_e and P_t , the green line between P_t and P_s and the red line for a pressure above P_s . The yellow line shows the total crush-curve.

of porous pumice, using a compression testing machine (for more details see Jutzi et al. 2009). The fitted parameters of the crush-curve are in Table 1. The crush-curve was fitted to an initial distention of $\alpha_{0,\text{fit}} = 4.64$, which needs to be rescaled for the initial distention used in the specific simulation. Thus, to rescale the equations a correction factor is multiplied to each term except the 1, which is

$$\chi = \frac{\alpha_{0,\text{sim}} - 1}{\alpha_{0,\text{fit}} - 1} \quad (15)$$

with $\alpha_{0,\text{sim}}$ as the initial distention of the specific simulation and $\alpha_{0,\text{fit}}$ as the initial distention of the fitted crush-curve. Figure 1 shows the relation between the distention α and the pressure P . Depending on the pressure, the distention changes accordingly. Since we are interested in the time

evolution of the distention, we can calculate it using the equation

$$\dot{\alpha} = \frac{d\alpha}{dP} \frac{dP}{dt}. \quad (16)$$

The derivative $d\alpha/dP$ is given by

$$\frac{d\alpha}{dP} = \begin{cases} \left[\frac{d\alpha}{dP} \right]_{\text{elastic}} & \text{if } P < P_e \text{ or } dP \leq 0 \\ \left[\frac{d\alpha}{dP} \right]_{\text{plastic}} & \text{otherwise,} \end{cases} \quad (17)$$

which is just a case distinction between the elastic and the plastic regime, as well as the assumption that unloading (from a partially compacted) state is elastic. The derivative $d\alpha/dP$ reads

$$\frac{d\alpha}{dP} = \begin{cases} -n_1 \chi(\alpha_e - \alpha_t) \frac{(P_t - P)^{n_1 - 1}}{(P_t - P_e)^{n_1}} - n_2 \chi(\alpha_t - 1) \frac{(P_s - P)^{n_2 - 1}}{(P_s - P_e)^{n_2}} & \text{if } P_e < P < P_t \\ -n_2 \chi(\alpha_t - 1) \frac{(P_s - P)^{n_2 - 1}}{(P_s - P_e)^{n_2}} & \text{if } P_t \leq P < P_s \\ 0 & \text{if } P \geq P_s. \end{cases} \quad (18)$$

The time evolution of the pressure dP/dt can be written as

$$\frac{dP}{dt} = \left(\frac{\partial P}{\partial \rho} \right)_{E, \alpha} \frac{d\rho}{dt} + \left(\frac{\partial P}{\partial E} \right)_{\rho, \alpha} \frac{dE}{dt} + \left(\frac{\partial P}{\partial \alpha} \right)_{E, \rho} \frac{d\alpha}{dt}. \quad (19)$$

With the use of the relations $\rho_s = \rho\alpha$, $P = P_s/\alpha$ and $E = E_s$, as well as Eq. 19 and Eq. 16, the final equation for the time derivative of the distention can be calculated

$$\dot{\alpha} = \frac{\dot{E} \left(\frac{\partial P_s}{\partial E_s} \right) + \alpha \dot{\rho} \left(\frac{\partial P_s}{\partial \rho_s} \right) \frac{d\alpha}{dP}}{\alpha + \frac{d\alpha}{dP} \left[P - \rho \left(\frac{\partial P_s}{\partial \rho_s} \right) \right]} \frac{d\alpha}{dP}. \quad (20)$$

Therefore, we know how the distention evolves in time which enables us to calculate the density of the matrix material at later times. Since the Tillotson EOS is used for the porosity model, the parameters $\partial P_s/\partial E_s$ and $\partial P_s/\partial \rho_s$ are gained by deriving the Tillotson EOS. However, since the equations always refer to the pressure of the matrix material, the density in these equations also refers to the density of the matrix material and thus is replaced by $\rho_s = \rho\alpha$.

In section 2.2 and 2.3, the deviatoric stress tensor $S^{\kappa\lambda}$ and the damage D were introduced and need to be adapted to porous materials.

Because we used the density of the matrix material to calculate the pressure we introduce a factor f for the deviatoric stress tensor

$$f \equiv \frac{[\nabla \mathbf{v}]_s}{[\nabla \mathbf{v}]}. \quad (21)$$

The motivation for this definition of the factor f is the fact that both, the velocity divergence and the time derivative of the deviatoric stress tensor are linear combinations of the spatial derivative of the components of the velocity vector.

After using the continuity equation for the matrix material and for the porous material, as well as using $\dot{\rho}_s = \dot{\alpha}\rho + \alpha\dot{\rho}$ we get

$$f = 1 + \frac{\dot{\alpha}\rho}{\alpha\dot{\rho}}. \quad (22)$$

The factor f is used to compute the time evolution of the deviatoric stress tensor $S^{\kappa\lambda}$ for the porous material

$$\frac{dS^{\kappa\lambda}}{dt} \rightarrow f \frac{dS^{\kappa\lambda}}{dt}. \quad (23)$$

Since according to Eq. 21, the velocity divergence of the matrix is given by

$$[\nabla\mathbf{v}]_s = f [\nabla\mathbf{v}], \quad (24)$$

we obtain

$$\left[\frac{dS^{\kappa\lambda}}{dt} \right]_s = f \left[\frac{dS^{\kappa\lambda}}{dt} \right]. \quad (25)$$

In addition to the multiplication by f , the deviatoric stress tensor $S^{\kappa\lambda}$ is multiplied by α^{-1} as it is done with the hydrostatic pressure P . We finally write the time evolution of $S^{\lambda\kappa}$ in the following form

$$\frac{d}{dt} \left[\frac{1}{\alpha} S^{\kappa\lambda} \right] = \frac{1}{\alpha} \frac{dS^{\kappa\lambda}}{dt} - \frac{1}{\alpha^2} S^{\kappa\lambda} \frac{d\alpha}{dt}, \quad (26)$$

where $dS^{\kappa\lambda}/dt$ is modified according to equation (23).

As mentioned above, the damage model also needs to be adapted. In the fragmentation model by Grady & Kipp (1980), the parameter damage D also depends on the pressure P , which was divided by the distention to account for porosity. First, since the volume of the matrix material is smaller than the total volume for porous material, one needs to divide the total volume by the distention and distribute the flaws with respect to the actual volume of the matrix. Second a compaction part is introduced as a linear correlation between the damage and the distention to account for the distention change. This is assumed, because both variables are defined as volume ratios. The boundary conditions for the relations are $D = 0$ for $\alpha = \alpha_0$ and $D = 1$ for $\alpha = 1$ which leads to

$$D = 1 - \frac{\alpha - 1}{\alpha_0 - 1}. \quad (27)$$

To avoid divergence for $\alpha = \alpha_0$, we use a small quantity $\delta D = 0.01$. After normalizing the damage, the porous part of the time evolution of $D^{1/d}$ with the dimension d is then given by

$$\frac{dD^{\frac{1}{d}}}{dt} = -\frac{1}{d} \frac{\left[1 - \frac{\alpha-1}{\alpha_0-1} + \delta D\right]^{\frac{1}{d}-1}}{(1 + \delta D)^{\frac{1}{d}} - (\delta D)^{\frac{1}{d}}} \frac{1}{\alpha_0 - 1} \frac{d\alpha}{dt}. \quad (28)$$

Thus, the total time evolution of the damage is given by

$$\left(\frac{dD^{\frac{1}{d}}}{dt}\right)_{\text{total}} = \left(\frac{dD^{\frac{1}{d}}}{dt}\right)_{\text{tension}} + \left(\frac{dD^{\frac{1}{d}}}{dt}\right)_{\text{compression}}, \quad (29)$$

where the tension part comes from the normal fracture model by Grady & Kipp (1980) and the compression part is the addition by Jutzi et al. (2009). The sound speed for a porous material in this model is given by

$$c_s^2 = \frac{\partial}{\partial \rho} P(\rho, E, \alpha) \quad (30)$$

at constant entropy. For porous material using the Tillotson EOS it follows

$$c_s^2 = \frac{\alpha \left(\frac{\partial P_s}{\partial \rho_s}\right) + P \rho^{-2} \left(\frac{\partial P_s}{\partial E_s}\right)}{\alpha + \frac{d\alpha}{dP} \left[P - \rho \left(\frac{\partial P_s}{\partial \rho_s}\right)\right]}. \quad (31)$$

In the end we have a relation between the distention α and the pressure P which was measured for porous pumice. We have an equation which gives us the time derivative of the distention, a modified deviatoric stress, an additional term to the damage and a different sound speed.

At first, a new pressure, as well as the derivatives $\partial P_s / \partial \rho_s$ and $\partial P_s / \partial E$ are calculated using the Tillotson EOS. Then, the change in pressure from the previous time step to the current is calculated. With this we can calculate the derivative $d\alpha / dP$. After obtaining the change in distention with regard to the pressure, we can calculate the sound speed, as well as the factor for the deviatoric stress tensor. As soon as the integration of the density and energy is done, we evolve the distention in time. The time evolution of the damage is calculated last.

3 Simulations

The simulations performed in this work are chosen in a way that the parameter space of the impact scenario to create Stickney covers the extreme

Table 2. Parameters for all impact simulations with the target Phobos (ellipsoidal parameters a , b and c , density ρ_t and mass m_t) and the impacting projectile (density ρ_p , mass m_p and distention α_p).

Phobos data		Source
a [km]	13.5	Willner et al. (2014)
b [km]	11.0	Willner et al. (2014)
c [km]	9.0	Willner et al. (2014)
ρ_t [kg/m ³]	1880	Rosenblatt (2011)
m_t [10 ¹⁶ kg]	1.05	(calculated)
ρ_p [kg/m ³]	2250	Britt et al. (2002)
α_p	1.11	Britt et al. (2002)

cases. Phobos was modeled as an ellipsoid with parameters a , b and c and the impactor was modeled as a sphere with radius r_p . Table 2 shows the fixed parameters and Table 3 shows the varied parameters. With two projectile radii, two impact velocities, two porosities and two impact angles we get a total amount of 16 different simulations.

The impactor hits Phobos in the $x - y$ plane. For the head on case the impactor only has a velocity in x direction and hits Phobos on the semi-major axis with $y, z = 0$. The 45° impact is also in the $x - y$ plane and the point of impact is still on the semi-major axis with $y, z = 0$ and to this point of impact the angle is taken. Figure 2 and 3 show the geometry of the impact simulations for the two angles.

We assumed a porosity of 10% for the projectile, regarding the average meteorite types suggested by Britt et al. (2002). As for Phobos we assumed a porosity of 20% and 33.3% to cover the parameter space taken from Andert et al. (2010). The two impact velocities v_p were 5.3 km/s and 8.5 km/s taken from Schmedemann et al. (2014). In the simulations the radius of the impactor r_p was 250 m and 500 m. For the impact angle ϕ we chose 0° and 45° to get an impression of the impact influences for ellipsoidal bodies and their resulting craters.

For the calculation of the crater depth and width we calculated the particles which remain near the crater (with a velocity of $v_x < 4$ m/s). We chose this criteria, since the escape velocity of Phobos is roughly 11 m/s and particles close to the escape velocity will not stay near the crater. The crater depth was then calculated as the difference in height (x values) between the highest and lowest point of the remaining particles and the width as the difference in width (y values for $\phi = 0^\circ$ and z values for $\phi = 45^\circ$) between the highest particles on both sides of the crater.

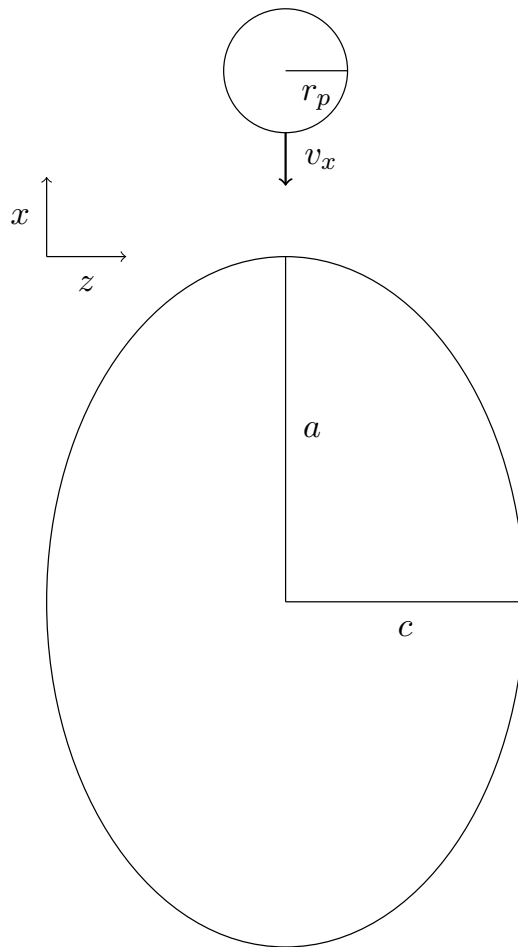


Figure 2. Schematic geometry of the impact scenario for a head on scenario with $\phi = 0^\circ$. The x -axis and z -axis are shown, as well as the ellipse with the semi-major axis a and semi-minor axis c . The impactor with radius r_p has only a velocity component in x direction v_x .

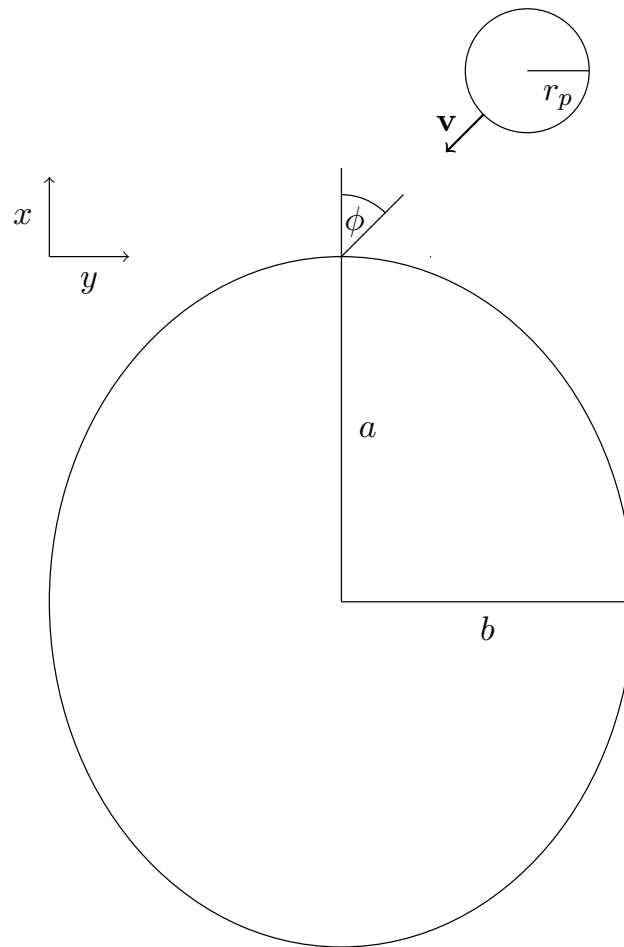


Figure 3. Schematic geometry of the impact scenario with $\phi = 45^\circ$. The x -axis and y -axis are shown, as well as the ellipse with the semi-major axis a and semi-minor axis b . The impactor with radius r_p has a velocity component in x and y direction with $v_x = v_y$.

Table 3. Varied parameters in the impact simulations are the impact angle ϕ , the radius r_p (and the resulting mass m_p), the impact velocity of the projectile v_p and the distention α_t of Phobos. Combining all variations, we performed 16 simulations in total.

Phobos data		Source
r_p [m]	250	Bruck Syal et al. (2016)
m_p [10^{11} kg]	1.47	(calculated)
r_p [m]	500	Lucchetti et al. (2015)
m_p [10^{11} kg]	11.78	(calculated)
ϕ [$^\circ$]	0 (head-on)	
ϕ [$^\circ$]	45	
v_p [m/s]	5300	Schmedemann et al. (2014)
v_p [m/s]	8500	Schmedemann et al. (2014)
α_t	1.25	Andert et al. (2010)
α_t	1.5	Andert et al. (2010)

4 Simulation results

Figures 5 to 7 show a slice of the x - z plane and Figure 8 of the x - y plane at $t = 150$ s. Figure 4 shows the impact scenario with the low velocity, low porosity and low impactor radius for the head on case. The crater is rather shallow and not very wide. Compared to Stickney, it is far off. Figure 5 shows the same impact scenario with the higher impact velocity. The crater is clearly wider and deeper than in the previous case. The crater width is close to that of Stickney, yet still too narrow. The impact scenario in Figure 6 shows the same as in the previous one but with the higher porosity. Once again, the crater becomes deeper and slightly wider. For the more porous case, we get much less ejected material. The impact scenario in Figure 7 included the lower velocity and lower porosity, and with a larger impactor radius. The crater differs strongly from the previous ones in both width and depth. Compared to Stickney, one may conclude that the larger impactor at the velocity has too much kinetic energy, resulting in a larger crater. In Figure 8 the low impact velocity, the small impactor and the low porosity simulation is shown with an impact angle of 45° . The crater is slightly deformed compared to the head on collision with one steeper and one more shallow crater side. The crater depth and width do not differ a lot from the head on impact results. In Table 4, we present the results of our simulations. Those regarding the impactor with $r_p = 500$ m and $v_p = 8.5$ km/s could not be evaluated since the crater was almost as wide as Phobos itself and thus only one case was simulated and for the other

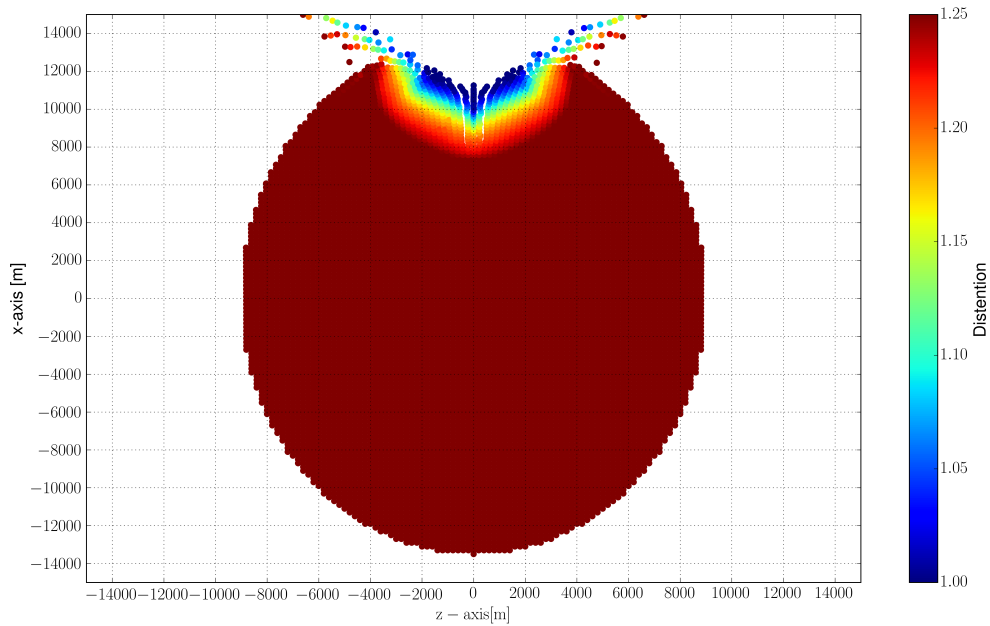


Figure 4. Impact on Phobos with an impactor radius $r_p = 250$ m, an impact velocity of $v_p = 5.3$ km/s and an impact angle of $\phi = 0^\circ$. The distention of Phobos was $\alpha = 1.25$ which translates to a porosity of $\Phi = 20\%$. The resulting crater was 5.1 km in width and 1.25 km in depth.

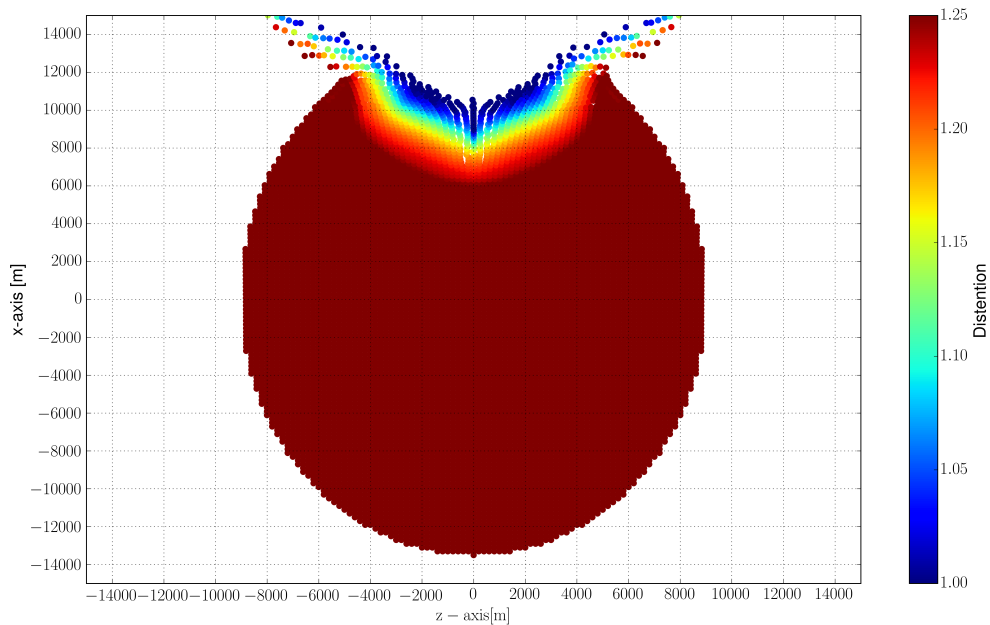


Figure 5. Impact on Phobos with an impactor radius $r_p = 250$ m, an impact velocity of $v_p = 8.5$ km/s and an impact angle of $\phi = 0^\circ$. The distention of Phobos was $\alpha = 1.25$ which translates to a porosity of $\Phi = 20\%$. The resulting crater was 7.3 km in width and 1.6 km in depth.

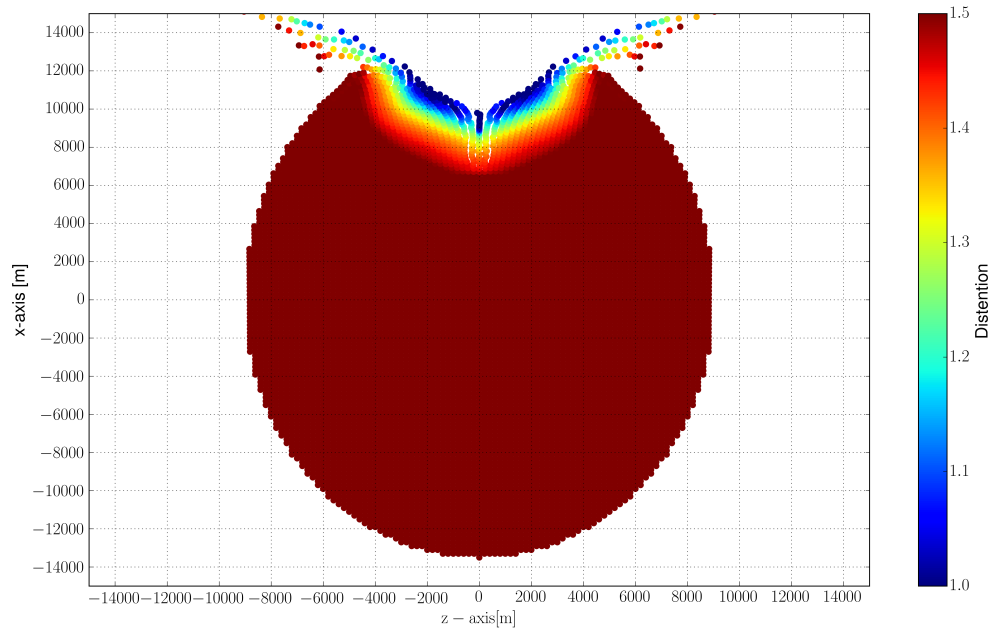


Figure 6. Impact on Phobos with an impactor radius $r_p = 250$ m, an impact velocity of $v_p = 8.5$ km/s and an impact angle of $\phi = 0^\circ$. The distention of Phobos was $\alpha = 1.5$ which translates to a porosity of $\Phi = 33.3\%$. The resulting crater was 7.4 km in width and 1.9 km in depth.

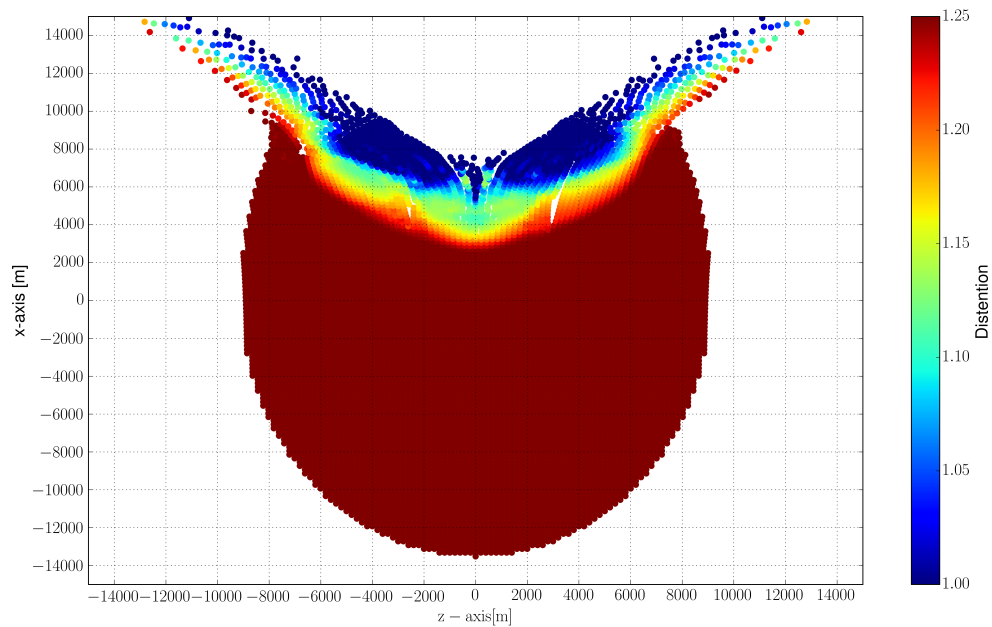


Figure 7. Impact on Phobos with an impactor radius $r_p = 500$ m, an impact velocity of $v_p = 5.3$ km/s and an impact angle of $\phi = 0^\circ$. The distention of Phobos was $\alpha = 1.25$ which translates to a porosity of $\Phi = 20\%$. The resulting crater was 11.0 km in width and 3.6 km in depth.

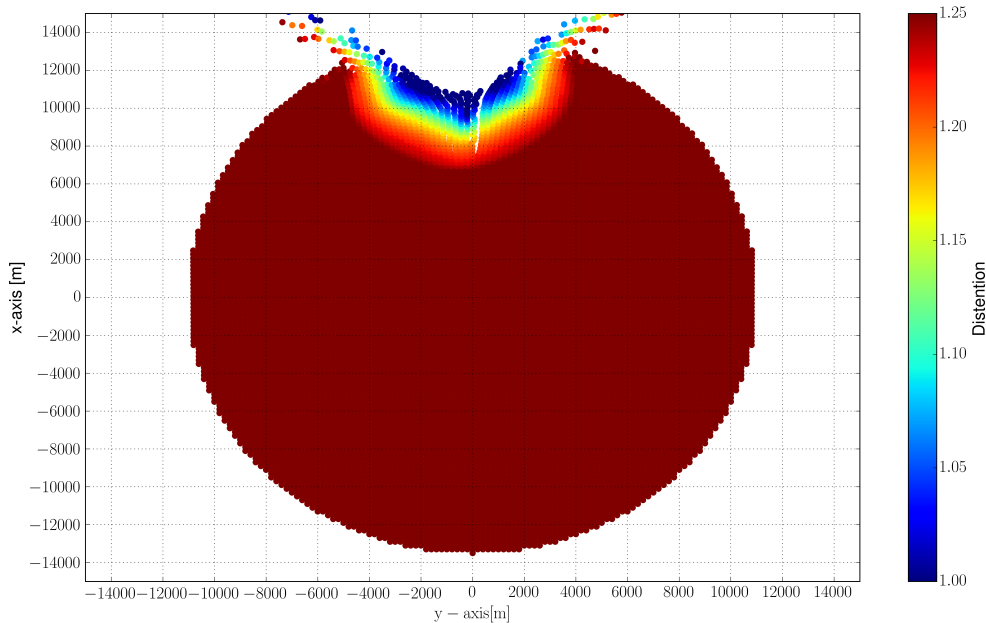


Figure 8. Impact on Phobos with an impactor radius $r_p = 250$ m, an impact velocity of $v_p = 8.5$ km/s and an impact angle of $\phi = 45^\circ$. The distention of Phobos was $\alpha = 1.25$ which translates to a porosity of $\Phi = 20\%$. The resulting crater was 6.2 km in width and 1.5 km in depth.

cases we did not simulate the large impactor with high velocity.

5 Conclusions

In this paper, we have presented a variation of simulations of impacts on Phobos to investigate the formation of Stickney. Our goal was to discern which impact parameters are realistic and to improve our understanding on the formation of large craters on small bodies.

1. Regarding the impactor radius: We can clearly see in our simulations, that an impactor with a radius of $r_p = 500$ m results in a crater which exceeds the crater depth and width of Stickney by far. Therefore, we conclude that the impactor on Phobos had to be smaller than 500 m and most probably larger than 250 m, since the resulting craters are smaller than Stickney.
2. Regarding the impact velocity: Obviously, a higher impact velocity leads to a deeper and wider crater. Therefore, it strongly depends on the impactor radius to discern the velocity. For a larger impactor, a slower and for a smaller impactor, a higher impact velocity is reasonable.

Table 4. Overview of the impact simulations including the radius of the impactor r_p , the distention α , the impact velocity v_p , the impact angle ϕ and the depth d and the width w of the resulting crater.

r_p [m]	α	v_p [km]	ϕ	w [km]	d [km]
250	1.25	5.3	0	5.1	1.25
250	1.25	5.3	45	4.5	1.1
250	1.25	8.5	0	7.3	1.6
250	1.25	8.5	45	6.2	1.5
250	1.5	5.3	0	5.3	1.75
250	1.5	5.3	45	4.6	1.5
250	1.5	8.5	0	7.4	1.9
250	1.5	8.5	45	5.5	1.8
500	1.25	5.3	0	11.0	3.6
500	1.25	5.3	45	9.5	3.4
500	1.25	8.5	0	16.4	3.8
500	1.25	8.5	45	-	-
500	1.5	5.3	0	10.1	3.8
500	1.5	5.3	45	9.7	3.2
500	1.5	8.5	0	-	-
500	1.5	8.5	45	-	-

3. Regarding the porosity: A more porous target leads to a deeper and at most slightly wider crater. Thus, this also needs to be taken into account to tighten the parameter space to form Stickney.
4. Regarding the impact angle: A head on impact forms a symmetric crater, whereas an impact with a more shallow angle results in a slightly deformed crater and the higher the velocity and/or the larger the impactor, the stronger this effect becomes.

Taking the different parameters into account, we conclude, that the impactor to form Stickney needs to be smaller than 500 m in radius. Our resulting craters for the $r_p = 250$ m impactor were a bit too narrow, even with $v_p = 8.5$ km/s, which would indicate that the impactor was at least slightly larger. Realistically between 300 m and 400 m with a velocity around 6.5 km/s to 8.5 km/s. With respect to the porosity, our results suggest that Phobos is roughly 25% porous, as Stickney is wide and shallow and the effect of porosity on the crater depth is stronger than on the crater width. The impact angle could not be pinpointed to a certain range.

Acknowledgements: TIM acknowledges support from the FWF Austrian Science Fund under project S11603-N16.

References

- Andert, T. P., Rosenblatt, P., Pätzold, M., et al. 2010, *Geophysical Research Letters*, 37, 109202
- Benz, W., & Asphaug, E. 1999, *Icarus*, 142, 5
- Britt, D. T., Yeomans, D., Housen, K., & Consolmagno, G. 2002, *Asteroid Density, Porosity, and Structure*, ed. W. F. Bottke, Jr., A. Cellino, P. Paolicchi, & R. P. Binzel (University of Arizona Press), 485–500
- Bruck Syal, M., Rovny, J., Owen, J. M., & Miller, P. L. 2016, *Geophysical Research Letters*, 43, 10,595, 2016GL070749
- Burns, J. A. 1978, *Vistas in Astronomy*, 22, 193
- Carroll, M., & Holt, A. C. 1972, *Journal of Applied Physics*, 43, 759
- Giuranna, M., Roush, T. L., Duxbury, T., et al. 2011, *Planet. Space Sci.*, 59, 1308
- Grady, D., & Kipp, M. 1980, *International Journal of Rock Mechanics and Mining Sciences & Geomechanics Abstracts*, 17
- Herrmann, W. 1969, *Journal of Applied Physics*, 40
- Jutzi, M., Michel, P., Hiraoka, K., Nakamura, A. M., & Benz, W. 2009, *Icarus*, 201
- Lucchetti, A., Cremonese, G., Pajola, M., Massironi, M., & Simioni, E. 2015, in *Lunar and Planetary Inst. Technical Report*, Vol. 46, Lunar and Planetary Science Conference, 1420
- Mises, R. v. 1913, *Nachrichten von der Gesellschaft der Wissenschaften zu Göttingen, Mathematisch-Physikalische Klasse*, 1913, 582
- Nakamura, A. M., Michel, P., & Setoh, M. 2007, *Journal of Geophysical Research (Planets)*, 112, 2001
- Rosenblatt, P. 2011, *A&A Rv*, 19, 44
- Schäfer, C., Riecker, S., Maindl, T. I., et al. 2016, *A&A*, 590, A19
- Schmedemann, N., Michael, G. G., Ivanov, B. A., Murray, J. B., & Neukum, G. 2014, *Planet. Space Sci.*, 102, 152
- Thomas D. Jones, Larry A. Lebofsky, John S. Lewis, & Mark S. Marley. 1990, *Icarus*, 88, 172
- Tillotson, J. H. 1962, *Metallic Equations of State for Hypervelocity Impact*, Tech. Rep. General Atomic Report GA-3216, General Dynamics, San Diego, CA
- Veverka, J., Thomas, P., & Duxbury, T. 1978, *S&T*, 56, 186
- Weibull, W. 1939, *A statistical theory of the strength of materials (Generalstabens litografiska anstalts förlag)*
- Willner, K., Shi, X., & Oberst, J. 2014, *Planet. Space Sci.*, 102, 51

Triggering the Activation of Main Belt Comets: The Effect of Porosity

N. Haghighipour

Institute for Astronomy, University of Hawaii-Manoa, Honolulu, HI, 96825, USA

nader@ifa.hawaii.edu

T. I. Maindl

Department of Astrophysics, University of Vienna, A-1180 Vienna, Austria

C. M. Schäfer and O. J. Wandel

Institut für Astronomie und Astrophysik, Eberhard Karls Universität Tübingen, 72076 Tübingen, Germany

ABSTRACT

It has been suggested that the comet-like activity of Main Belt Comets is due to the sublimation of sub-surface water-ice that is exposed when these objects are impacted by meter-sized bodies. We recently examined this scenario and showed that such impacts can in fact excavate ice and present a plausible mechanism for triggering the activation of MBCs (Haghighipour et al. 2016). However, because the purpose of that study was to prove the concept and identify the most viable ice-longevity model, the porosity of the object and the loss of ice due to the heat of impact were ignored. In this paper, we extend our impact simulations to porous materials and account for the loss of ice due to an impact. We show that for a porous MBC, impact craters are deeper, reaching to ~ 15 m implying that if the activation of MBCs is due to the sublimation of sub-surface ice, this ice has to be within the top 15 m of the object. Results also indicate that the loss of ice due to the heat of impact is negligible, and the re-accretion of ejected ice is small. The latter suggests that the activities of current MBCs are most probably from multiple impact sites. Our study also indicates that in order for sublimation from multiple sites to account for the observed activity of the currently known MBCs, the water content of MBCs (and their parent asteroids) needs to be larger than the values traditionally considered in models of terrestrial planet formation.

Subject headings: methods: numerical – minor planets, asteroids: general

1. Introduction

With orbital and dynamical properties characteristic of asteroids, and tails similar to those of comets, Main-Belt Comets (MBCs) have attracted a great deal of interest since their identification as activated asteroids by Hsieh & Jewitt in 2006. Most of the interest in these objects is due to the implication that their comet-like activity is the result of the sublimation of sub-surface volatiles, presumably water-ice. This, combined with results of dynamical studies that suggest MBCs are native to the asteroid belt (see below), argues strongly in support of the idea that water-carrying planetesimals and planetary embryos from the outer part of the asteroid belt provided the majority of Earth’s water during its formation.

At the time of this writing, 8 unambiguous MBCs were known¹. Table 1 and figure 1 show these objects along with some of their physical and orbital properties. As shown here, MBCs are km-sized bodies with orbits that are mainly in the outer part of the asteroid belt. Dynamical studies by Haghhighipour (2009, 2010) and Hsieh & Haghhighipour (2016) strongly suggest that these objects are most probably fragments of larger asteroids, and were scattered to their current orbits through interactions with giant planets. This scenario is also supported by the fact that three of these objects, namely, 133P/(7968) Elst-Pizarro, 313P/Gibbs, and P/2012 T1 (PANSTARRS) are members of two asteroid families (Nesvorný et al. 2008; Hsieh et al. 2013, 2015). We refer the reader to Haghhighipour et al. (2016, hereafter Paper I) for a comprehensive review of the origin, dynamics, and activation of MBCs.

It has been suggested that the activity of MBCs is most likely due to the sublimation of sub-surface water-ice that has been exposed through impacts of these objects with small, meter-sized bodies (Hsieh et al. 2004; Hsieh & Jewitt 2006). We would like to note in addition to collision, rotational disruption, for instance due to YORP effect (Steckloff et al. 2016; Graves et al. 2017) or rapid rotation (Sheppard & Trujillo 2015) has also been proposed as a mechanism to break up comets and activated asteroids, and expose their sub-surface volatiles. In Paper I, we examined the collision-activation scenario of MBCs by modeling impacts using our SPH code. We showed that for a wide range of material strength and water content of MBCs, and for impact velocities typical of those in the asteroid belt, the impact craters are deep and large enough to expose water-ice. Our results also indicated that the depths of impact craters, resulted from collisions of m-sized bodies with km-sized objects, are slightly larger than 10 m implying that

¹We call an MBC unambiguous if its activation can only be explained by sublimation of volatiles.

- if the activity of MBCs is due to the sublimation of water-ice, ice must be buried no deeper than approximately 15 m from the surface of the object, and
- the water content of MBCs (as well as those planetesimals and planetary embryos responsible for the delivery of water to the accretion zone of Earth) must be much higher than the 5% water-mass fraction that is traditionally considered in models of terrestrial planet formation.

While results of our simulations in Paper I clearly demonstrated that impacts of m-sized objects can in fact excavate ice (and other volatiles) to trigger the activation of MBCs, they had some limitations. Because in that paper, focus was placed on proving the concept and identifying the most viable ice-longevity model that would be consistent with the sublimation-driven activity of MBCs, the porosity of the target and the loss of ice due to the heat of impact were ignored. Porosity can play an important role as porous materials have lower strength which causes impactors to penetrate deeper in the target, and also affects the geometry and morphology of the impact crater. For instance, while the results presented in paper I were consistent with the ice-longevity model proposed by Schörghofer (2008) (this author suggests that a thin layer of solid material on the surface of an asteroid would be sufficient to preserve water-ice for the age of the solar system), if porosity causes impact craters to be deeper than 50 m, a competing theory by Prialnik & Rosenberg (2009) for ice-longevity in asteroid belt may also be applicable. These authors suggest that water-ice inside an asteroid can sublimate during the evolution of the solar system causing the ice level to sink to depths below 50 m.

In this paper, we extend our simulations to include porous targets, and examine the degree to which porosity plays a role in the final depth and size of an impact crater, as well as the plausibility of the two ice-longevity models. To consider porosity, we implemented in our SPH code the $P-\alpha$ porosity model of Jutzi et al. (2008), and simulated the impact between a m-sized body and a km-sized object for different impact velocities, impact angles, and water contents of an MBC.

The outline of our paper is as follows. We continue in section 2 by explaining our computational method and the implementation of porosity. In section 3, we present results of our impact simulations and present a comparison between these results and those in Paper I. We conclude our study in sections 4 and 5 by discussing the implications of the results and presenting highlights of our findings.

2. SPH Simulations and Initial Set-up

To simulate impacts, we use a 3D SPH code developed by Schäfer et al. (2007, 2016) and Maindl et al. (2013). This code solves the continuity equation and the equation of the conservation of momentum in continuum mechanics. It also includes material strength and implements a full elasto-plastic model (see, e.g., Maindl et al. 2013, 2014). We model any specific material using the Tillotson equation of state (Tillotson 1962; Melosh 1996). Fracture and brittle failure are treated using the Grady-Kipp fragmentation prescription (Grady & Kipp 1993; Benz & Asphaug 1994, 1999). This prescription is based on flaws that are distributed in the material following a Weibull distribution with material-dependent parameters.

The colliding bodies are discretized into mass packages (known as SPH particles) with each package carrying all physical properties (e.g., mass, momentum, energy) of the part of the solid body that it represents. As a result, depending on the type of the impactor or target material, particles may have different material parameters such as bulk and shear modulus and yield strength, or have different activation thresholds for the development of cracks. Each SPH particle moves as a point mass following the equation of motion.

To include porosity, we implemented an extension of the so called $P - \alpha$ model by Herrmann (1969) as described by Jutzi et al. (2009). Conceptually, this model is based on dividing the change in the volume of a porous material into two parts; the pore-collapse of the porous material, and the compression of the matrix material. These two parts are connected via a *distention parameter* α defined as

$$\alpha = \frac{\rho_s}{\rho}. \quad (1)$$

In this equation, ρ is the density of the porous material and ρ_s is the density of the corresponding matrix material. Following Carroll & Holt (1972), the pressure of the porous material (P) can be expressed as a function of the distention parameter (α) and the pressure of the solid material (P_s) as

$$P = \frac{1}{\alpha} P_s(\rho_s, E_s) = \frac{1}{\alpha} P_s(\alpha\rho, E). \quad (2)$$

Quantities ρ_s , ρ , E_s and E in equation (2) represent the density and internal energy of the solid and porous material, respectively. The internal energy corresponds to the energy contained inside the system due to the thermodynamical state of its internal parts excluding the kinetic energy of the object due to its bulk motion and its potential energy due to an external force. We note that in equation (2), it has been assumed that the energy of the surface pores (i.e., the energy necessary to change the assembly of pores on the surface of

an object) are negligible and, therefore, the energy of the porous material is equal to that of the solid material (i.e. $E = E_s$, Carroll & Holt 1972). We use the Tillotson equation of state (Tillotson 1962) to calculate the pressure as a function of ρ , E , and α .

3. Results of Impact Simulations

We considered a similar set up as in Paper I and simulated the impact between a m-sized impactor and a km-sized target. Because we are interested in the effect of porosity, we carried out simulations for four different cases: a dry and non-porous target, a non-porous target with 50% water-mass fraction of non-porous ice, a dry and porous target with 50% porosity (i.e., $\alpha = 2$), and a 50% porous target containing 50% water-mass fraction of 50% porous ice. We considered the impactor and the solid part of the target to be basalt², and because the size of the impactor is much smaller than the target, we considered the impactor to be non-porous. The material parameters for basalt and ice used in the Tillotson equation of state, and the Weibull parameters for the flaw distributions are given in Table 2.

We resolved the combined system of the impactor and target into approximately 500,000 SPH particles. Because compared to the time of the influence of the gravitational force of the target body, the impact timescales are very short (the collision velocities are in the order of km/s whereas the MBCs’ surface escape velocities are less than a few m/s, see Table 1), we simulated collisions without self-gravity (see Maindl et al. 2015, for more details). To analyze the evolution of the system during each impact, we took 100 snapshots every 0.4 ms. In between snapshots, time integration was continued with an adaptive step-size.

We carried out simulations for impact velocities of 1.5, 2.5, 3.5, 4.4, and 5.3 km/s. These values were chosen based on the study by Bottke et al. (1994), who showed that for objects of 50 km and larger, impact velocities in the asteroid belt have a mean value of ~ 5.3 km/s with a most probable value at 4.4 km/s. We considered an abundance of objects smaller than 50 km with similar orbital elements (e.g., semimajor axis, eccentricity, inclination) in the asteroid belt (i.e., $e \lesssim 0.25$). Given the small size of these objects, and therefore, their small gravitational interactions, collisions between these bodies will occur with relative velocities much smaller than a few km/s. Combining this assumption with results from Bottke et al.

²Although MBCs are most probably carbonaceous chondrites (CC), at the moment, no equation of state is known for CC material. Also, the purpose of this study is merely to understand the significance of including porosity in impact simulations. Because the equation state of basalt is well known, we, therefore, considered objects to be basaltic. A comprehensive model of the impact of m-sized bodies with km-sized CC MBCs is currently in the works.

(1994), we considered a range of impact velocities from 1.5 km/s to 5.3 km/s. The impact angles were chosen to be 0, 30° and 45°.

Figure 2 shows snap shots of the final craters of two sets of simulations for an impact velocity of 4.4 km/s. The target is a mixture of 50% porous basalt and 50% porous water-ice and has a 50% water-mass fraction. The left column shows the impact for a head-on collision and the right column shows the results for an impact angle of $\beta = 30^\circ$. The orange color represents porous basalt and blue is porous water-ice. As expected, water-ice is exposed in the interior part of the impact crater and is also scattered out due to the impact. Movies of these simulations can be found in the electronic supplementary material.

A comparison between these results and those of non-porous simulations points to interesting differences. The most prominent difference is in the shape and morphology of craters. Figure 3 shows impact craters of simulations with porous (top) and non-porous (bottom) targets. Both objects have a water-mass fraction of 50%. The impact velocities in all simulations are 4.4 km/s. As shown here, craters in the porous targets are noticeably deeper and narrower, and extend in the direction of impact velocity. In contrast, the craters in non-porous targets are shallower and much wider. Figure 4 shows this more clearly and for all our simulations with different target material and different impact velocities.

Figures 2 and 3 also show that craters form in a very short time and have irregular shapes. This asymmetry in the shapes of the final craters seems to be in contrast with the works of Collins (2014) and Milbury et al. (2015) who assumed that except for the most oblique cases, all impacts produce approximately radially symmetric craters. We believe that the reason for the quick formation of craters in our simulations and their irregular shapes lies in the fact that the gravity of our targets (i.e., MBCs) are negligible. Gravity is the main factor in forming final craters from transient ones. In the absence of gravity, the plastic flows during the impact phase stop rather quickly after the impact. In our systems, the MBCs do not have much gravity and as a result, the craters are formed quickly and are solely strength-dominated. We refer the reader to Collins et al. (2009) for crater formation in oblique impacts without gravity.

Because in porous targets, craters are irregularly shaped, we determined their depth by directly measuring the distance between the lowest point of their crater to the surface of the target. To determine the surface area of a crater, we followed the methodology presented in Paper I and calculated the area by fitting an ellipsoid to the crater. We refer the reader to sections 3.1 and 3.3 of of Paper I for more details on the technical aspects of our calculations. The increase in the penetration of the impactor in a porous target can, then, be attributed to the fact that compared to non-porous objects, porous targets, especially those with mixture of water-ice, have lower material strength. As a result, when these objects are impacted,

the momentum and energy of the impact carry the impactor deeper in the target whereas in non-porous objects, the rapid compaction of the target at the impact site causes the energy of the impact to be transferred laterally creating a less deep but wider crater. An important implication of the results shown by figure 4 is that crater depths are still smaller than 15 m suggesting the model by Schörghofer (2008) as the most viable ice-longevity model in the asteroid belt.

It has been suggested that the activity of an MBC, in addition to ice sublimation from the bottom and interior of an impact crater, may also be due to the sublimation of scattered ice that was re-accreted on the surface of the MBC. To examine this scenario, we calculated the amount and velocity of ejected ice after each collision. Figures 5 and 6 show the results. Figure 5 shows the amount of scattered ice in terms of the impact velocity and figure 6 separates this quantity into groups based on the ejection velocity of scattered ices. The vertical axis in this figure shows the accumulative mass of the ejected ice and the horizontal axis shows its velocity. Each curve corresponds to a different impact velocity for both porous and non-porous targets. As shown here, in all simulations, the ejection velocity of ice is larger than 20 m/s. An examination of Table 1 indicates that this ejection velocity is almost 10 times greater than the largest escape velocity of the currently known MBCs implying that almost all ejected ice is lost and there is basically no re-accretion. This strongly suggests that the activity of MBCs is most likely due to ice sublimation from multiple impact sites.

We also studied the change in the porosity of the target due to an impact. Figure 7 shows variations in the porosity of the targets of figure 2 during an impact. The color coding represents the value of the distention parameter α corresponding to the porosity of the target. Yellow represents 50% porosity where $\alpha = 2$ and black corresponds to no porosity where $\alpha = 1$. The left column corresponds to a dry, porous target and the right column represents the same object with 50% water content. As shown here, material on the surface of the impact crater is strongly compacted with the strongest compaction occurring at the bottom where the target becomes non-porous. As the shock of the impact propagates throughout the object, the degree of compaction lessens at deeper distances suggesting that away from the impact site and well inside the object, the target maintains its original porosity. Our simulations show that the propagation of shocks do not cause the target to disintegrate, and therefore, in addition to the maintaining its original porosity, the target maintains its original water content as well. The latter has important implications for the delivery of water to the accretion zone of Earth with water-carrying planetesimals and planetary embryos. As the orbits of these objects evolve during their dynamical evolution and they reach the accretion zone of Earth, they are repeatedly impacted by planetesimals and planetary embryos. However, as shown here and given the sizes of these objects, they can still maintain their water-ice deep inside until they are accreted by the still-forming Earth. Movies of the

simulations of figure 7 can be found in the electronic supplementary material.

4. Discussion

We carried out an extensive analysis of the impact of a m-sized body with a km-sized MBC. We extended our previous simulations (Paper I), where objects were considered to be non-porous, to more realistic cases where the porosity of an MBC is taken into account. We carried out simulations for different values of impact velocities and impact angles, and considered different water contents for the target. Results of simulations indicate that as expected, substantial amount of water-ice is exposed on the interior surface of impact craters providing a viable pathway for triggering activity of MBCs. Results also indicated that the depth and size of craters increase for porous targets, however, the increase in depth is still within the regime (< 15 m) where the ice-longevity model by Schörghofer (2008) applies.

In addition to being more realistic, our new simulations advanced those in Paper I by including vaporization due to the heat of impact. We treated phase transition during ice vaporization at the time of the impact by using the Tillotson equation of state. Results are shown in figure 8. As shown here and in agreement with the results obtained from observations, the amount of ice vaporized during an impact is very small. For instance, for the case of 176P/(118401) LINEAR, the entire ice vaporization due to an impact is less than 5 tons whereas the rate of ice-sublimation due to the activation of this body is ~ 720 kg/day. Other MBCs sublimate about an order of magnitude higher per days. This finding suggests that when modeling impacts as a way of excavating sub-surface ice to trigger activation of MBCs, vaporization due to impacts can be safely ignored.

As mentioned earlier, the combination of the high material strengths of our targets (see Table 2), small sizes of our impactors, and very low surface gravity of MBCs points to the fact that our impacts and their final craters are strength-dominated. This has strong implications when comparing our results with previous studies, in particular those of Richardson et al. (2007). These authors used the mathematical model developed by Holsapple (1993) and presented a thorough study of many impact properties of comets. A comparison of our results with those of these authors indicates that although our results are comparable with their findings within the order of magnitude, our crater diameters are smaller. This is not unexpected as our impacts involve asteroids which naturally have higher dynamic material strengths (Asphaug et al. 2002) compared to soft targets such as comets Basilevsk et al. (2016). For instance, our assumed porous, wet MBC material has an average density of 685 kg/m³. With an effective MBC diameters between 0.3 km and 4.0 km (see Table 1), the mean surface gravity of our targets range from 0.057 mm/s² to 0.38 mm/s², mostly lower

than Richardson et al. (2007)'s nominal value of 0.34 mm/s^2 . Given the range of our impact velocities (1.5 km/s - 5.3 km/s), our crater diameters fall between 3 m and 13.3 m, which, quite understandably, are smaller than those presented by Richardson et al. (2007). The crater diameters estimated by these authors range between 22 m to 26 m, and correspond to considerably faster projectiles (10.2 km/s) impacting softer targets.

Our assessment of the amount of the re-accreted ice after an impact indicated that, because of the low gravity of the target, except for cases where the impact velocities are very low, most scattered ice particles are lost and are not accreted back. This finding is consistent with previous results as reported in Paper I, and confirm that activation of MBCs must be due to ice sublimation from multiple impact sites.

In this study, we did not consider a regolith layer on the top of the target. We assumed a random distribution for ice inclusions and considered ice to exist everywhere throughout the target including its top surface. Although inclusion of a regolith layer might have resulted in craters with slightly smaller depths, the scattered fragments of the regolith layer could impact other parts of the target and expose ice in other sites causing underlying ice to be exposed in a larger area. The latter may compensate for smaller ice re-accretion and smaller ice exposure in the main impact crater. This scenario is currently being investigated.

5. Concluding Remarks

We close this study by presenting highlights of our findings.

- Impacts of small bodies presents a viable mechanism for exposing sub-surface volatiles including water-ice to trigger sublimation-driven activity of MBCs.
- The loss of ice due to the heat of impact is negligible.
- Most of the ejected ice particles are lost and not re-accreted.
- A comparison between ice sublimation from impact craters obtained from our simulations with results of observations suggests that activity of the current MBCs are most probably from multiple impact sites.
- Results of simulations suggest that the water content of MBCs and those of their parent asteroids needs to be larger than those traditionally considered in the models of terrestrial planet formation so that the sublimation of the exposed water-ice can account for the rate of sublimation obtained from observations of these objects.

- If the activation of MBCs is due to the sublimation of sub-surface water-ice, this ice must be buried within the top 15 m. This result points to the model of ice-longevity by Schörghofer (2008) as the most viable model for the retention of water-ice in the asteroid belt. This author suggested that a small layer of regolith on the outer surface of an asteroid can allow the body to maintain its sub-surface water ice for the age of the solar system.

NH acknowledges support from NASA PAST program under grant NNX14AJ38G. T.I.M. acknowledges support from FWF Austrian Science Fund, project S11603-N16. Most of the numerical simulations in this study were performed on the bwFor-CLuster BinAC, supported by the state of Baden-Württemberg through bwHPC, and the German Research Foundation (DFG) through grant INST 39/963-1 FUGG.

REFERENCES

- Asphaug, E., Ryan, E. V. & Zuber, M. T. 2002, in: Asteroids III, W. F. Bottke Jr., A. Cellino, P. Paolicchi, and R. P. Binzel (eds), University of Arizona Press, Tucson, p.463-484
- Basilevsky, A. T., Krasil'nikov, S. S., Shiryayev, A. A. et al. 2016, *Sol. Syst. Res.*, 50, 225
- Benz, W. & Asphaug, E. 1994, *Icarus*, 107, 98
- Benz, W. & Asphaug, E. 1999, *Icarus*, 142, 5
- Bottke, W. F., Nolan, M. C., Greenberg, R. & Kovoord, R. A. 1994, *Icarus*, 107, 255
- Carroll, M. M. & Holt A. C. 1972, *J. Appl. Phys.*, 43, 1626
- Collins, G. S., Davison, T., Elbeshausen, D. & Wünnemann, K. 2009, LPSC contribution 1620
- Collins, G. S. 2014, *JGR: Planet*, 119, 2600
- Grady, D. E. & Kipp, M. E. 1993, in: J. R. Asay & M. Shahinpoor (Eds), *High Pressure Shock Compression of Solids* (Springer-Verlag, New York), Chapter 5, 265
- Haghighipour, N. 2009, *Meteor. & Planet. Sci.*, 44, 1863

- Haghighipour, N. 2010, in: *Icy Bodies of the Solar System, Proceedings of the IAU Symposium 263*, 207
- Haghighipour, N., Maindl, T. I., Schäfer, C., Speith, R. & Dvorak, R. 2016, *ApJ*, 830, 22
- Herrmann, W. 1969, *J. Appl. Phys.*, 40, 2490
- Holsapple K. A. 1993, *Annu. Rev. Earth Planet. Sci.*, 21, 333
- Hsieh, H. H., Jewitt, D. C. & Fernández, Y. R. 2004, *AJ*, 127, 2997
- Hsieh, H. H. & Jewitt, D. 2006, *Science*, 312, 561
- Hsieh H. H., Yang, B., Haghighipour, N., Novaković, B., et al. 2012a, *AJ*, 143, 104
- Hsieh H. H., Yang, B., Haghighipour, N., Kaluna, H. M., et al. 2012b, *ApJ*, 748, L15
- Hsieh H. H., Kaluna, H. M., Yang, B., Novaković, B., et al. 2013, *ApJ*, 771, L1
- Hsieh H. H., Hainaut, O., Novaković, B., Bolin, B., et al. 2015, *ApJ*, 800, L16
- Hsieh, H. H. & Haghighipour, N. 2016, *Icarus*, 277, 19
- Graves, K., Minton, D. A., Molaro, J. & Hirabayashi, M. 2017, *American Astronomical Society, DPS meeting 49*, Abstract id.100.05
- Jewitt, D., Yang, B. & Haghighipour, N. 2009, *ApJ*, 137, 4313
- Jewitt, D., Hsieh, H. & Agarwal, J. 2015, in P. Michel, F. DeMeo & W. Bottke (Eds), *ASTEROIDS IV* (University of Arizona Press, Tucson), 221
- Jutzi, M., Benz, W. & Michel, P. 2008, *Icarus*, 198, 242
- Jutzi, M., Michel, P., Hiraoka, K., Nakamura, A. M. & Benz, W. 2009, *Icarus*, 201, 802
- Maindl, T. I., Schäfer, C., Speith, R., Süli, Á., Forgács-Dajka, E. & Dvorak, R. 2013, *AN*, 334, 996
- Maindl, T. I., Dvorak, R., Schäfer, C. & Speith, R. 2014, in: Knežević, Z. & Lemaître, A. (Eds), *Complex Planetary Systems, Proceedings of the IAU Symposium 310*, 138
- Maindl, T. I., Dvorak, R., Lammer, H., Güdel, M., Schäfer, C., Speith, R., Odert, P., Erkaev, N. V., Kislyakova, K. G. & Pilat-Lohinger, E. 2015, *A&A*, 574, A22
- Melosh, H. J. 1996, *Impact Cratering*, Oxford University Press

- Milbury, C., Johnson, B. C., Melosh, H. J., Collins, G. S., Blair, D. M., Soderblom, J. M., Nimmo, F., Bierson, C. J., Phillips, R. J. & Zuber, M. T. 2015, *GeoRL*, 42, 9711
- Nesvorný, D., Bottke, W. F., Vokrouhlický, D., et al. 2008, *ApJ*, 679, 143
- Prialnik, D. & Rosenberg, E. D. 2009, *MNRAS*, 399, L79
- Richardson J. E., Melosh H. J., Lisse C. M. & Carcich B. 2007, *Icarus*, 190, 357
- Schäfer, C., Speith, R. & Kley, W. 2007, *A&A*, 470, 733
- Schäfer, C., Riecker, S., Maindl, T. I., Scherrer, S., Speith, R. & Kley, W. 2016, *A&A*, 590, A19
- Schörghofer, N. 2008, *ApJ*, 682, 697
- Sheppard, S. S., Trujillo, C. 2015, *AJ*, 149, article id. 44
- Steckloff, J. K., Graves, K., Hirabayashi, M., Melosh, H. J. & Richardson, J. E. 2016, *Icarus*, 272, 60
- Tillotson, J. H. 1962. *Metallic Equations of State for Hyper-velocity Impact*. General Atomic Report GA-3216, General Atomic, San Diego, CA.

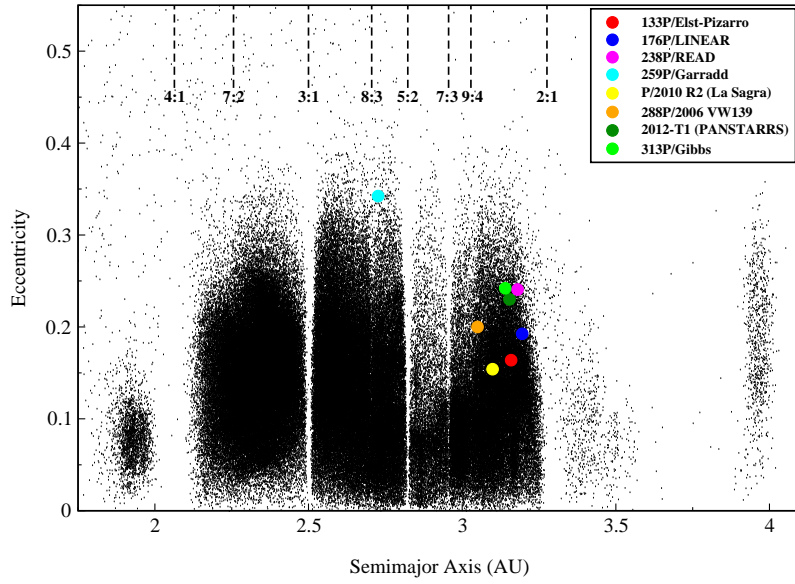


Fig. 1.— Locations of the currently known MBCs in the asteroid belt. The background shows all asteroids and the positions of mean-motion resonances with Jupiter.

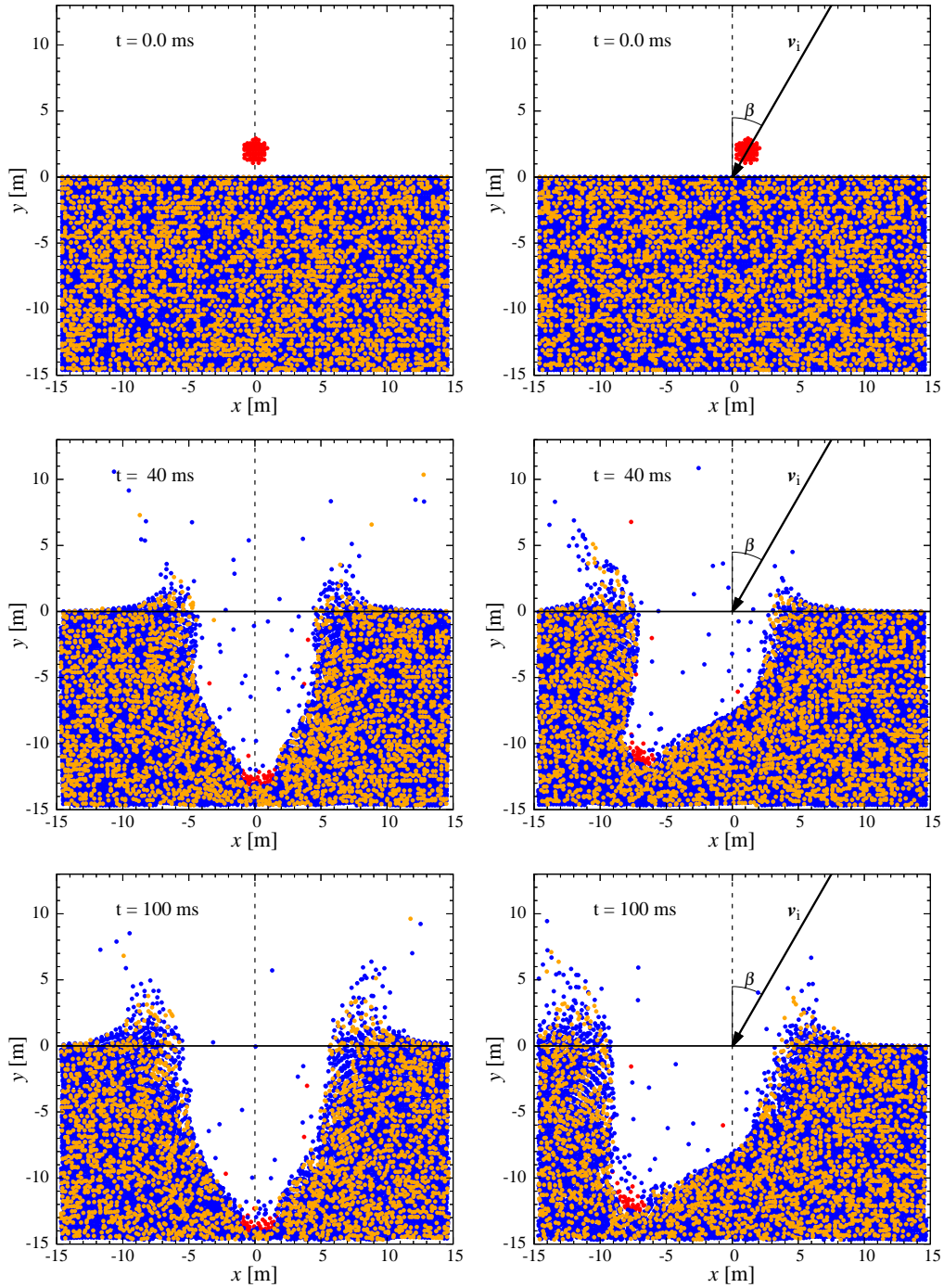


Fig. 2.— Snapshots of the collision of a m-sized object with a porous basaltic target with 50% water-mass fraction. The degree of porosity is 50%. The impactor is pure basalt with no porosity (red). The impact velocity is 4.4 km/s. The impact angle is $\beta = 0$ (left) and 30° (right). The orange color represents porous basalt and blue is for porous ice. The panels show 2D slices of 3D data.

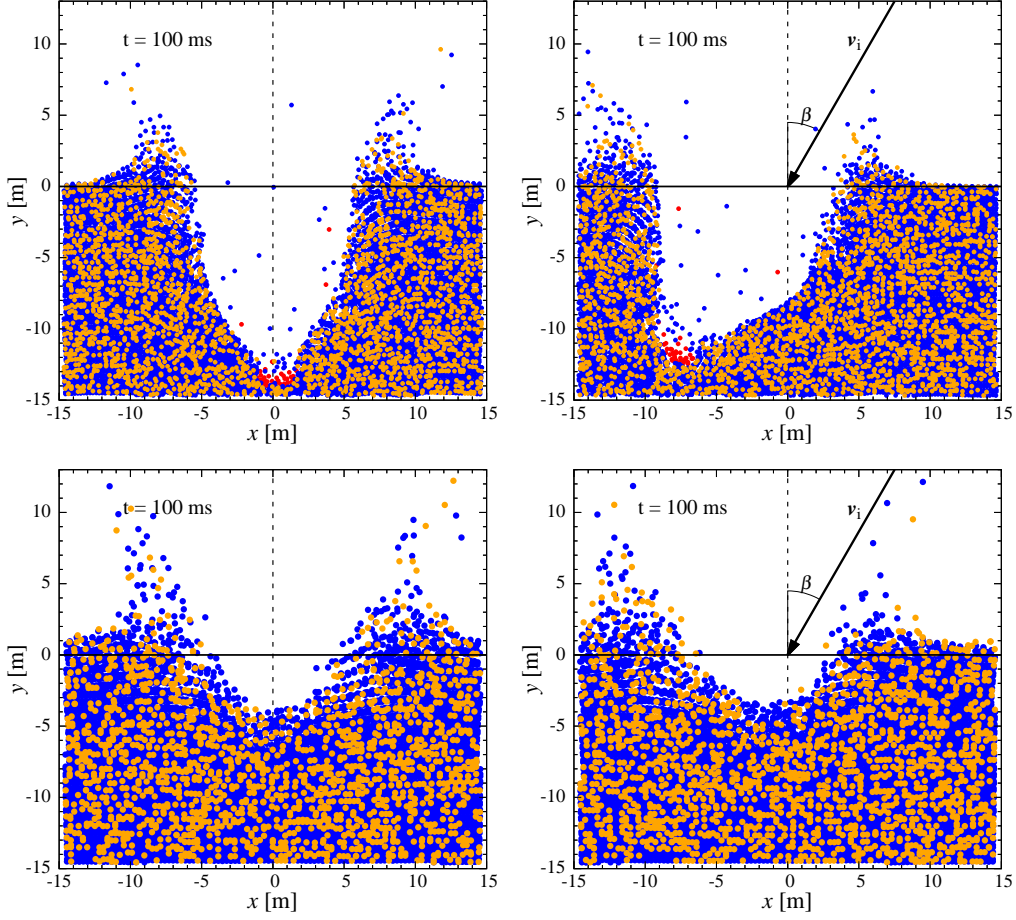


Fig. 3.— Comparing the depths and surface areas of impact craters with and without porosity. The target in the top panels is porous basalt with 50% water-mass fraction. The target in the bottom panels is non-porous basalt with 50% water-mass fraction. The impact velocity in all panels is 4.4 km/s. In the top panels, the orange color represents porous basalt and blue is for porous ice. In the bottom panels, the orange color represents non-porous basalt and blue is for non-porous ice. The panels show 2D slices of 3D data.

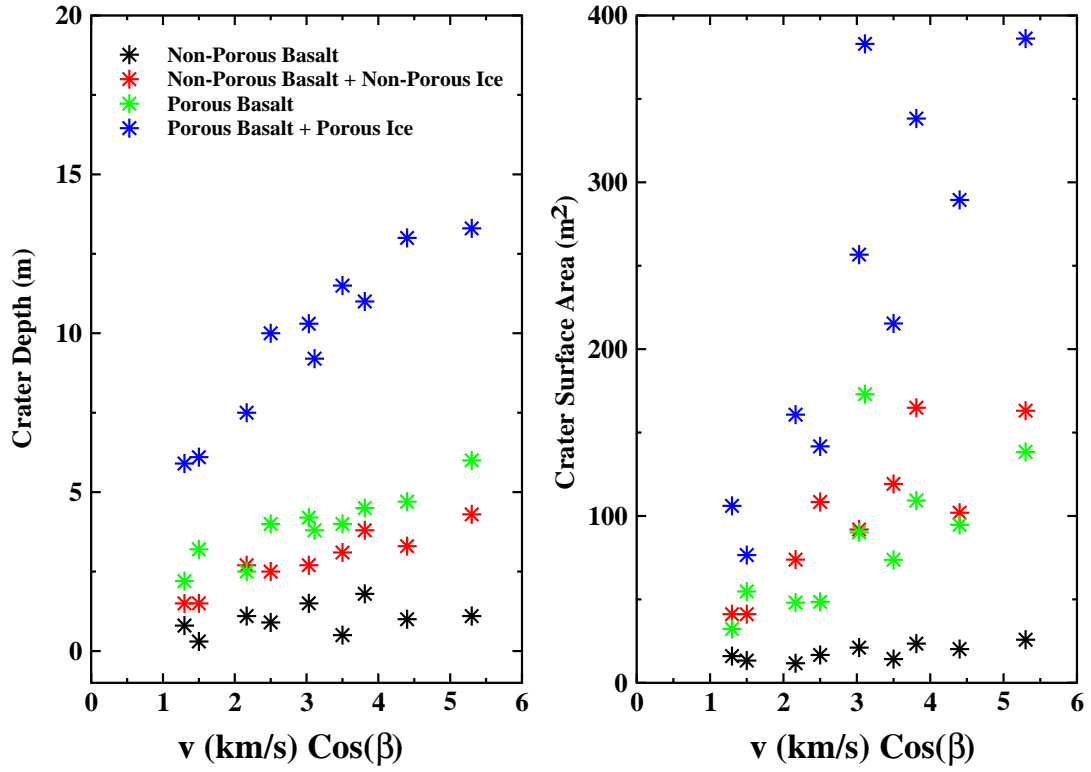


Fig. 4.— Graphs of the depth (left) and surface area (right) of impact craters in terms of impact velocity for porous and non-porous targets, and with different water contents.

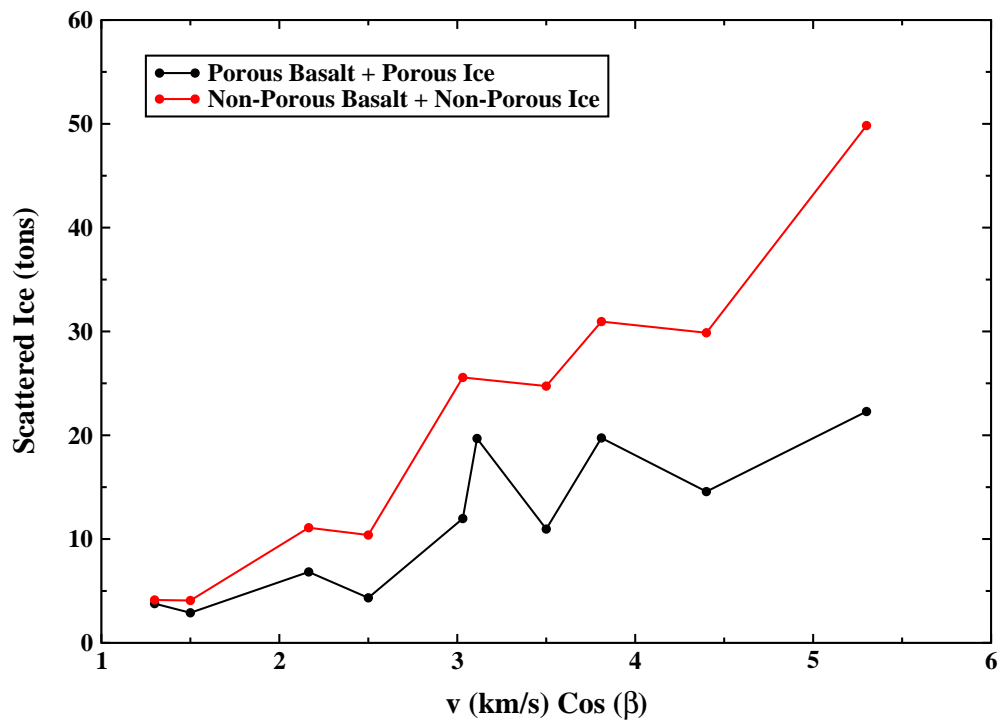


Fig. 5.— Graphs of the scattered ice in terms of impact velocity for porous and non-porous targets.

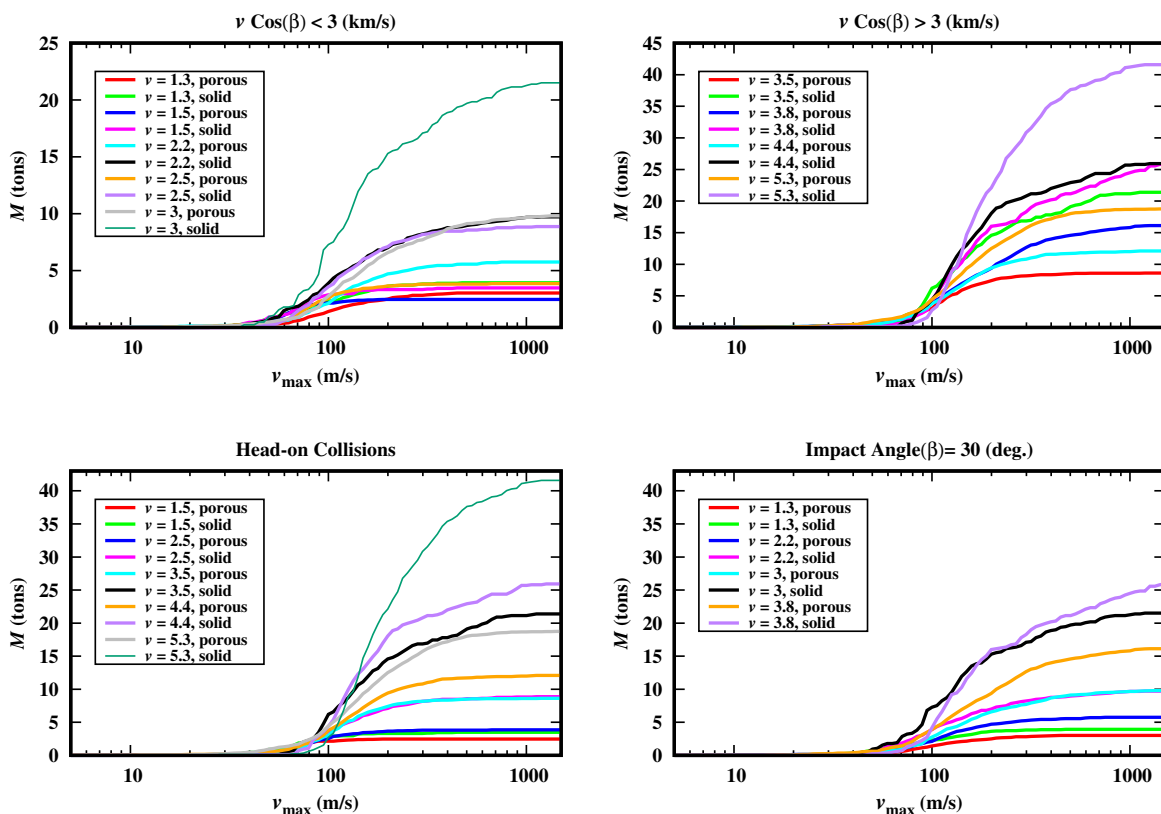


Fig. 6.— Graphs of the accumulative mass of the ejected ice in term of its velocity for different impact scenarios and impact velocities. The top panel corresponds to impacts for which the vertical component of the impact velocity is smaller (*left*) or larger (*right*) than 3 km/s. The bottom panels show ice ejection for a head-on (*left*) and a 30° (*right*) collision. As shown here, in all scenarios, the velocity of the ejected ice is larger than 20 m/s. The escape velocity of the currently known MBCs is smaller than 2.2 m/s. This figure shows that all ice is ejected and the amount of re-accreted ice is negligibly small.

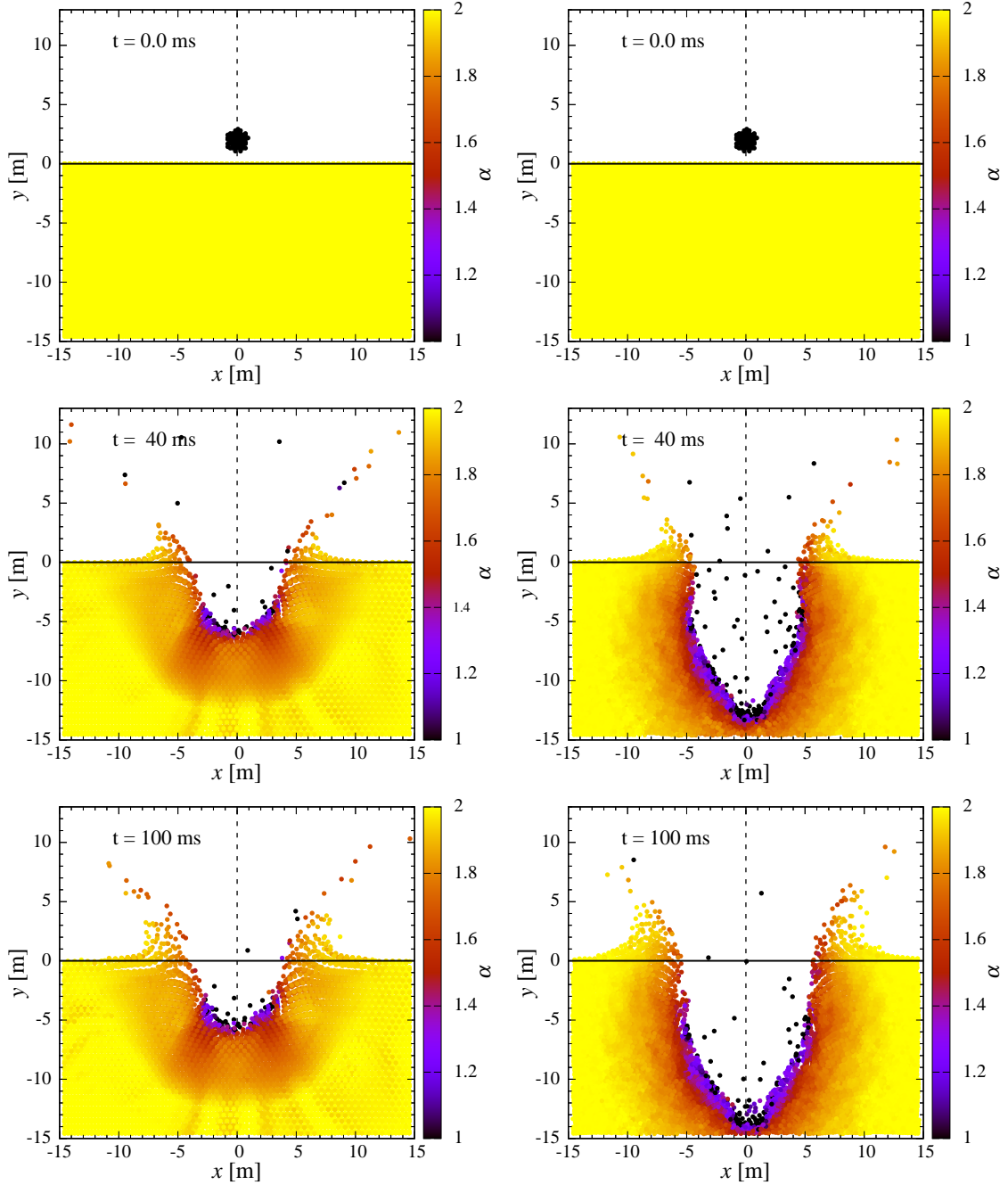


Fig. 7.— Snapshots of the variation of the porosity of the target in figure 1 during an impact. The color coding represents the value of the distention parameter α corresponding to the degree of compaction and porosity of the object. To better demonstrate changes in porosity, we show in the left column a dry, basaltic target with 50% porosity ($\alpha = 2$) and in the right column, we use the same target but this time with 50% water-mass fraction of porous ice. As shown here, the object is compacted at the site of the impact and the compaction extends to its inner parts as the shock of the impact propagates inside the body. However, most of the interior part of the target maintain its original porosity. The panels show 2D slices of 3D data.

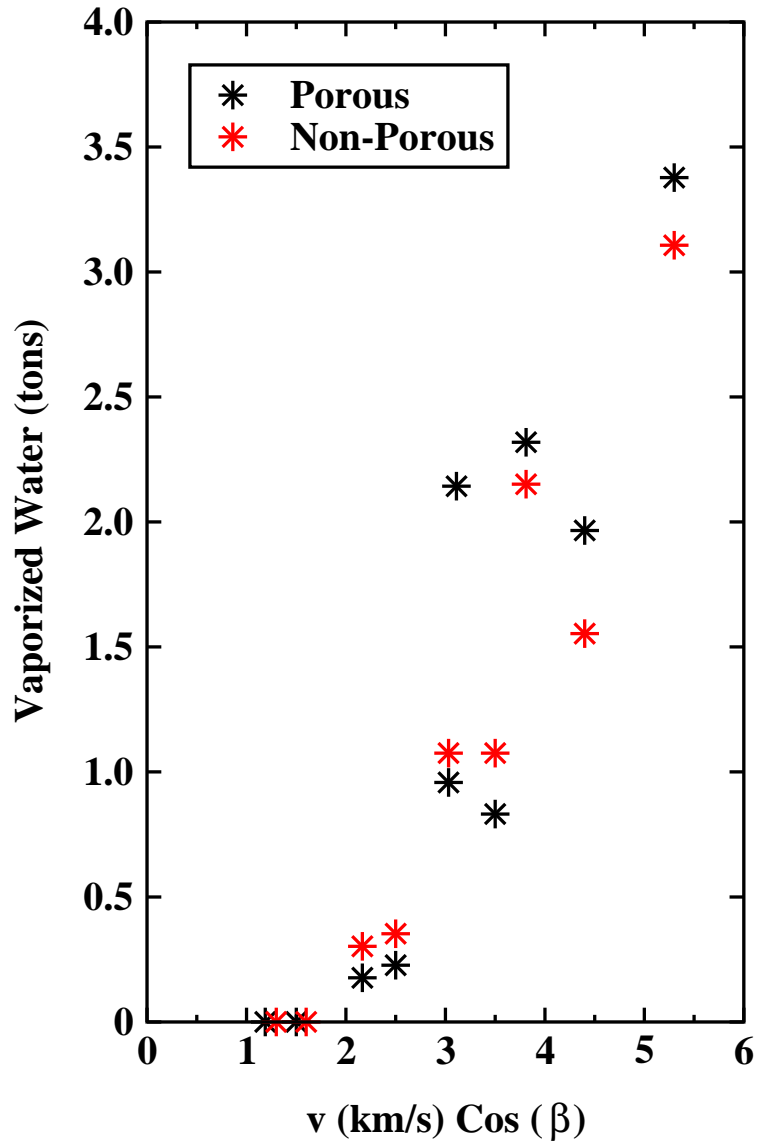


Fig. 8.— Graphs of the vaporized ice due to the heat of impact in terms of the impact velocity for porous and non-porous targets.

Table 1: Physical properties of the currently known MBCs. The quantity D_e represents an MBC’s effective diameter, a, e and i are its semimajor axis, eccentricity and orbital inclination, respectively, T_J is its Tisserand number with respect to Jupiter, and v_{esc} is the value of its escape velocity. Adopted from Jewitt et al. (2015).

Object	D_e [km]	a [AU]	e	i [deg]	T_J	v_{esc} [m/s]	Ref. ^a
133P/(7968) Elst-Pizarro	3.8 ± 0.6	3.157	0.165	1.39	3.184	2.13	1
176P/(118401) LINEAR	4.0 ± 0.4	3.196	0.192	0.24	3.167	1.95	1
238P/Read (P/2005 U1)	0.8	3.165	0.253	1.27	3.152	1
259P/Garradd (P/2008 R1)	0.3 ± 0.02	2.726	0.342	15.90	3.216	0.62	2
324P/La Sagra (P/2010 R2)	1.1	3.099	0.154	21.39	3.100	0.49	3,4
288P/(300163) 2006 VW ₁₃₉	3	3.050	0.200	3.24	3.203	...	5
P/2012 T1 (PANSTARRS)	2.4	3.154	0.236	11.06	3.134	...	6
313P/Gibbs (P/2014 S4)	1.0	3.156	0.242	10.97	3.132	0.86	7

^a1=Hsieh & Jewitt (2006), 2=Jewitt et al. (2009), 3=Hsieh et al. (2012a), 4=Hsieh et al. (2015), 5=Hsieh et al. (2012b), 6=Hsieh et al. (2013), 7=Hsieh et al. (2015)

Table 2. Material parameters for basalt and ice. The quantity ϱ_0 is the bulk density of the object. The 10 quantities ρ_0 , A_T , B_T , E_0 , E_{iv} , E_{cv} , a_T , b_T , α_T and β_T are the parameters used in the Tillotson equation of state (Melosh 1996). The remaining quantities, K , μ , and Y_0 are the bulk modulus, shear modulus, and yield stress, respectively. Values for basalt and ice are taken from (Benz & Asphaug 1999). Note that A_T and B_T are set equal to the bulk modulus.

Material	ϱ_0 [kg/m ³]	A_T [GPa]	B_T [GPa]	E_0 [MJ/kg]	E_{iv} [MJ/kg]	E_{cv} [MJ/kg]	a_T	b_T	α_T	β_T	K [GPa]	μ [GPa]	Y_0 [GPa]
Basalt	2700	26.7	26.7	487	4.72	18.2	0.5	1.50	5	5	26.7	22.7	3.5
Ice	917	9.47	9.47	10	0.773	3.04	0.3	0.1	10	5	9.47	2.8	1

The wide-binary origin of (2014) MU₆₉-like Kuiper belt contact binaries


<https://doi.org/10.1038/s41586-020-2194-z>

Evgeni Grishin^{1✉}, Uri Malamud¹, Hagai B. Perets¹, Oliver Wandel² & Christoph M. Schäfer²

Received: 19 February 2020

Accepted: 27 February 2020

Published online: 22 April 2020

 Check for updates

Following its flyby and first imaging of the Pluto–Charon binary, the New Horizons spacecraft visited the Kuiper belt object (KBO) 2014 MU₆₉ (also known as (486958) Arrokoth). The imaging showed MU₆₉ to be a contact binary that rotates at a low spin period (15.92 hours), is made of two individual lobes connected by a narrow neck and has a high obliquity (about 98 degrees)¹, properties that are similar to those of other KBO contact binaries inferred through photometric observations². However, all scenarios suggested so far for the origins of such configurations^{3–5} have failed to reproduce these properties and their probable frequent occurrence in the Kuiper belt. Here we show that semi-secular perturbations^{6,7} operating on only ultrawide KBO binaries close to their stability limit can robustly lead to gentle, slow binary mergers at arbitrarily high obliquities but low rotational velocities, reproducing the characteristics of MU₆₉ and other similar oblique contact binaries. Using *N*-body simulations, we find that approximately 15 per cent of all ultrawide binaries with a cosine-uniform inclination distribution^{5,9} are likely to merge through this process. Moreover, we find that such mergers are sufficiently gentle to deform the shape of the KBO only slightly. The semi-secular contact binary formation channel not only explains the observed properties of MU₆₉, but may also apply to other Kuiper belt or asteroid belt binaries and in the Solar System and extra-solar moon systems.

The discovery of the bilobate shape of MU₆₉ and its peculiar configuration provided new clues and opened avenues of exploration into the physical processes that sculpt the Solar System. Here we describe an evolutionary channel for the formation of MU₆₉ from an initially wide binary. We consider the initial binary to be a member of a hierarchical triple together with the Sun. Owing to secular evolution induced by the Sun, the inner orbit may experience changes in its eccentricity (*e*) and mutual inclination (*i*) on secular timescales much longer than the orbital period, known as Lidov–Kozai (LK) oscillations, which can be modelled using a secular orbit-averaging approach^{10,11}. Large LK oscillations take place when the mutual inclination is large ($40^\circ \leq i \leq 140^\circ$). The highest eccentricities are attained as the binary evolves to the lowest inclinations and vice versa¹².

If the eccentricity of the binary exceeds a threshold e_{coll} , the small pericentre allows binary collisions. Thus, LK evolution could lead to coalescence of individual Kuiper belt binary (KBB) members into a single, probably irregularly shaped, KBO⁵. However, because the closest approach occurs concurrently with the lowest inclinations, collisions mostly occur near $i \approx 40^\circ$ and $i \approx 140^\circ$ (ref. ¹³). Moreover, tidal effects and the non-spherical structure of KBB components quench LK evolution, which makes collision possible only in a small part of the parameter space^{5,14}. The standard LK mechanism is therefore disfavoured for the origin of the highly oblique MU₆₉, but can explain the origin of highly eccentric KBBs such as WW31 and 2001 QW322^{5,15,16}.

For larger ratios of the inner period to outer period, secular averaging breaks down and the evolution becomes semi-secular. The orbit of

the inner binary now evolves considerably on timescales of the outer orbit, and short-term fluctuations arise, making the LK evolution more complex^{6,7,17}. The maximal eccentricity can be calculated analytically, including in domains where it is unconstrained⁷ and the evolution is non-secular. Figure 1a shows the analytical two-dimensional parameter space for allowed and forbidden domains for collisions in terms of the initial inclination $\cos i_0$. The initial separation of the inner binary is normalized to the Hill radius, $r_{\text{H}} = a_{\text{out}}(m_{\text{in}}/3M_{\odot})^{1/3}$, where a_{out} is the outer semi-major axis, M_{\odot} is the mass of the Sun and m_{in} is the mass of the inner binary. For an inner semi-major axis *a*, the (dimensionless) separation $\alpha \equiv a/r_{\text{H}}$ cannot exceed the Hill stability limit for highly inclined orbits⁸, $\alpha_{\text{H}} = 0.4$. We use the outer orbit parameters of MU₆₉: $a_{\text{out}} = 44.581$ AU and eccentricity $e_{\text{out}} = 0.041$. We model the lobes as triaxial ellipsoids of dimensions approximately $22 \times 20 \times 7$ and $14 \times 14 \times 10$ km³ (ref. ¹), leading to a total radius $R_{\text{tot}} = 18$ km and inner mass $m_{\text{in}} = (1.61 + 1.03) \times 10^{18}$ g = 2.64×10^{18} g for a density of $\rho = 1$ g cm⁻³ (see Methods for other densities). Secular collisions occur only for sufficiently large critical inclination and beyond a certain initial separation α_{coll} , which overcomes LK quenching (see equation (12) and Methods). Non-secular collisions will dominate over secular collisions beyond a transitional separation α_{t} :

$$\alpha_{\text{t}} = 3^{1/3} \left[\frac{128}{135} \frac{(1 - e_{\text{out}}^2)}{\left(1 + \frac{2\sqrt{2}}{3} e_{\text{out}}\right)^2} \left(\frac{M_{\odot}}{m_{\text{in}}}\right)^{1/3} \frac{R_{\text{tot}}}{a_{\text{out}}} \right]^{1/4} \quad (1)$$

¹Physics Department, Technion–Israel Institute of Technology, Haifa, Israel. ²Institut für Astronomie und Astrophysik, Eberhard Karls Universität Tübingen, Tübingen, Germany.

✉e-mail: eugeneg@campus.technion.ac.il

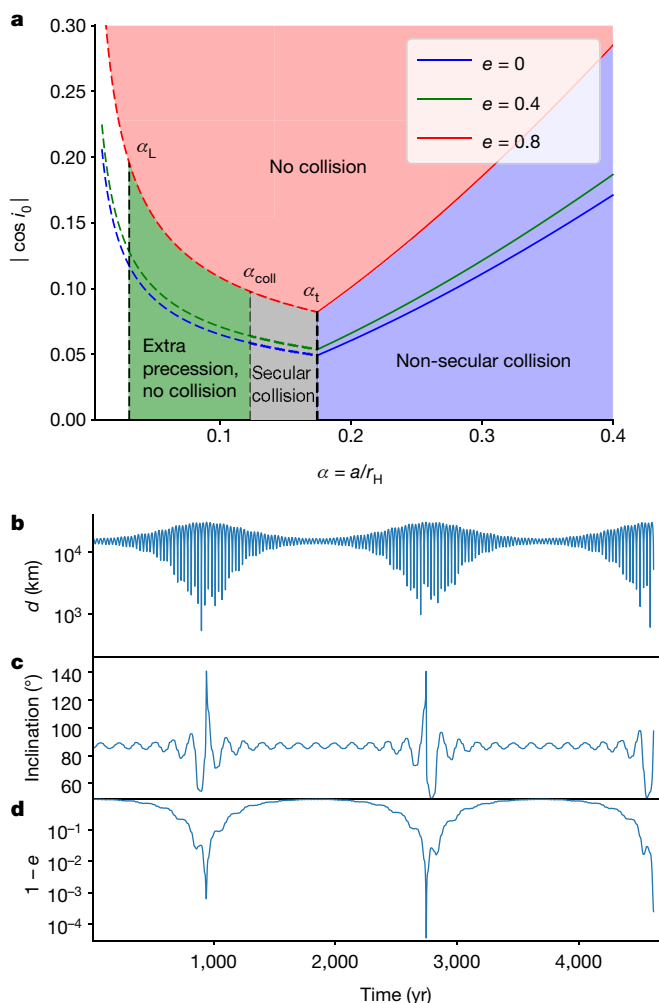


Fig. 1 | Roadmap to collisions of MU₆₉. **a**, The orbital evolution of MU₆₉ in initial separation–initial inclination space. The initial eccentricity, e , is 0 (blue), 0.4 (green) and 0.8 (red). Solid lines show the condition for non-secular collisions (equation (14)) with unbound eccentricity. Dashed lines show the conditions for a secular collision (equation (4)) with deterministic eccentricity. The different domains are as follows: white, LK oscillations are completely quenched and the eccentricity is constant, $\alpha < \alpha_t$ (equation (9)); green, the eccentricity is excited but below e_{coll} , and collisions are avoided, $\alpha_t < \alpha < \alpha_{coll}$ (equation (12)); grey, secular evolution can lead to a collision, $\alpha_{coll} < \alpha < \alpha_t$ (equation (1)); blue, non-secular perturbations dominate and lead to a collision; red, the initial inclination is too low to induce a collision. **b–d**, Time evolution of the instantaneous distance, inclination and eccentricity of an individual orbit with initial Keplerian elements: semi-major axis $a = 0.3r_H$, eccentricity $e = 0.1$, inclination $i = 86^\circ$, argument of periape $\omega = 0$, argument of ascending node $\Omega = \pi/4$ and mean anomaly $\mathcal{M} = 0$. The outer binary is set at $\Omega_{out} = 0$ and $\mathcal{M}_{out} = -\pi/4$.

In our case, $\alpha_t \approx 0.174$. Figure 1b demonstrates the separation in the non-secular regime before the collision. During the high-eccentricity phase, there are about 10 cycles where the instantaneous separation drops below 10^3 km. A collision occurs during the third LK cycle after about 4,600 yr. The mutual inclination flips its orientation during the high-eccentricity peak of the LK cycle (Fig. 1c). The eccentricity is essentially unbound and a collision eventually occurs (Fig. 1d).

To explore in detail the overall evolution and statistics of KBBs in the chaotic non-secular regime, we defer to detailed N -body simulations, which provide us with the probability for collisions and the post-collision characteristics. We use the publicly available code REBOUND¹⁸ with the IAS15¹⁹ integrator (see Methods for details and stopping conditions). We integrate four sets of initial conditions in

the non-secular regime. The first three sets have initial separations of $\alpha = 0.2, 0.3$ and 0.4 , and the fourth set has uniformly sampled separations in $\alpha = [0.2, 0.4]$. The orbital angles are sampled uniformly. The mutual inclination of observed binaries is cosine-uniform⁹, and thus we follow cosine-uniform sampling with a cut-off at $|\cos i| \leq 0.4$ (lower inclinations cannot lead to a collision). For each case, we run 250 simulations (except for $\alpha = 0.2$, for which we run 200 simulations and use $|\cos i| \leq 0.3$), each up to 5×10^4 yr.

Figure 2 shows the cumulative distribution function of various parameters of the colliding orbits. Both the closest-approach distance $q = a(1 - e)/R_{tot}$ (Fig. 2a) and the final inclinations (Fig. 2c) at collision are consistent with a uniform distribution (in $\cos i$) between 40° and 140° , suggesting that the orbits are indeed chaotic and in the non-secular regime, as expected. Most orbits induce collisions after about a few thousand years (Fig. 2b). The mean collision time increases with increasing separation. The velocity at impact is comparable to the escape velocity with a very small dispersion, consistent with a gentle collision²⁰ (Fig. 2d).

We find the overall merger fractions of wide binaries to be around 12%–18% (see Extended Data Table 1), which is roughly consistent with the observed 10%–25% occurrence of contact binaries for the cold classical belt²¹. Most mergers occur for initially high inclinations, as expected. About 1%–3% of all wide binaries produce highly oblique contact binaries ($i = 80^\circ$ – 100°), consistent with the observed high obliquity of MU₆₉, and providing predictions that can be verified by future KBO observations. There is little dependence on the underlying distribution of α , and merger rates are bounded between minimal and maximal values of 12% (for $\alpha = 0.2$) and 18% (for $\alpha = 0.4$). Moreover, in a collisional environment²² the binary orbits can be perturbed such that originally low-inclination orbits become highly inclined and become subject to semi-secular evolution, forming contact binaries; the quoted formation rates are thus lower limits to the total fraction of contact binaries formed through this process.

The non-merging systems continue to evolve quasi-periodically. On longer timescales, three-body encounters are expected to shape the populations of KBBs^{3,23}. Exchange interactions can drive the binaries into equal masses²⁴, and the loose nature of the binaries can result in evaporation (Heggie’s law)²⁵. There are only a handful of KBBs beyond $a \geq 0.05r_H$ with either prograde or retrograde orbits that are not highly inclined (see figure 1 of ref. ²⁶), whereas the widest known binary, 2001 QW₃₂₂, with $a \approx 0.2r_H$, is expected to disrupt within a billion years¹⁶.

To test the feasibility of the semi-secular collision origin of MU₆₉, we also need to account for the observed spin period of MU₆₉. Angular momentum conservation enables us to find the resulting spin period depending on the impact angle and the primordial spins of each component. The final impact parameter at collision (which corresponds to an impact angle; see Methods) is uniformly distributed, and thus our model can robustly produce a wide range of possible final rotation periods, without any fine-tuned modelling of the composition and density of MU₆₉, thus also alleviating the angular momentum problem of other models¹.

Figure 3a shows the outcome of a collision at a 40° impact angle with high-material-strength composition, which reproduces the shape of MU₆₉. Low- or medium-strength materials result in a deformed shape and are thus ruled out. If the density of MU₆₉ is halved compared to the fiducial 1 g cm^{-3} value (as suggested by ref. ¹), the escape velocity v_{esc} —at which typical collisions occur—is lower, and thus using medium-strength-material parameters also produces an undeformed shape. Random collisions—even at relative velocities as low as $10v_{esc}$ —destroy or heavily deform binaries with high-strength-material composition; they are likewise ruled out (see Methods). Figure 3b shows the expected spin-period dependence on the impact angle. An impact angle of about 40° reproduces the observed spin period (see Methods) for initially non-spinning objects. Taking a typical initial spin period of about 10 h with random orientations extends the range of plausible

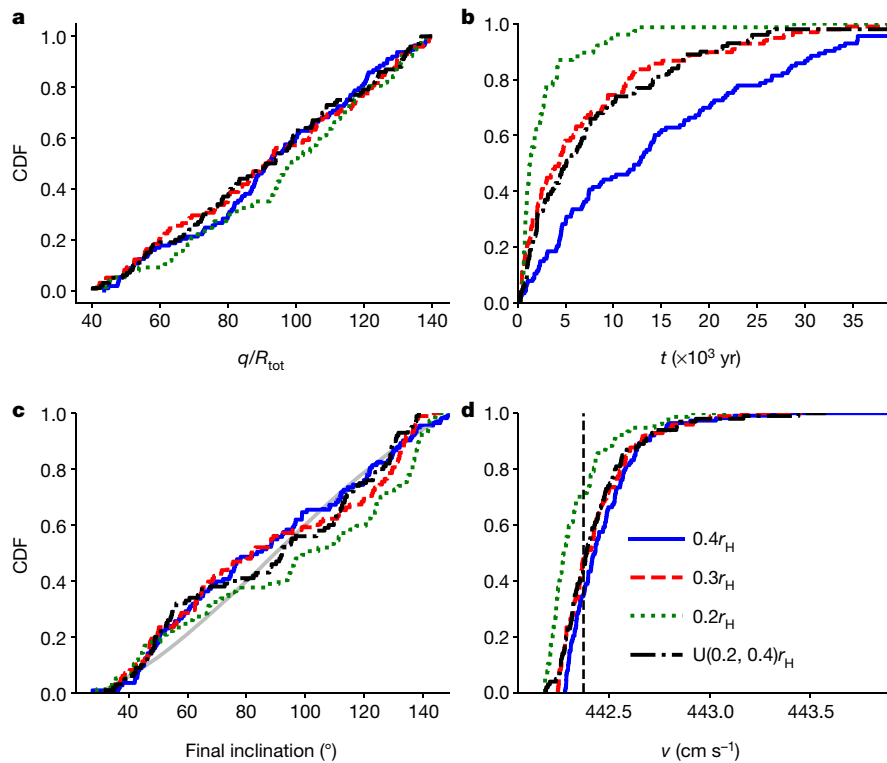


Fig. 2 | Cumulative distributions of the impact characteristics. The cumulative distribution functions (CDFs) are for $\alpha = 0.4$ (solid blue), 0.3 (dashed red), 0.2 (dotted green) and uniform in $(0.2, 0.4)$ (dash-dotted black). **a**,

Pericentre q/R_{tot} . **b**, Time of collision. **c**, Final inclination at impact. The shaded grey line is a uniform cumulative distribution in $\cos i$ in the range 30° – 150° . **d**, Velocity at impact. The vertical black dashed line is the escape velocity, v_{esc} .

impact angles to about 20° and 70° , for the maximally aligned and anti-aligned configurations, respectively. Smoothed particle hydrodynamics (SPH) collision simulations agree with our simplified estimate and support our assumptions of undeformed, rigid bodies when modelled with high-strength material parameters, or else medium-high strength parameters if the density and impact velocity are slightly lower (see ref. ²⁷ and Methods for details).

Together, our dynamical and post-collisional modelling yields a coherent picture for the origin of MU_{69} from an ultrawide KBO binary. Such wide KBB progenitors could be a natural byproduct of KBO and KBB evolution in the early Solar System^{3,28,29}. It is most probable that the characteristics of MU_{69} are not unique, and that secular or semi-secular evolution plays a major role in the evolution of many KBBs and in the

production of low-velocity collisions between individual KBB components. In fact, modelling of the Pluto–Charon system also suggests a low-velocity impact origin³⁰. Moreover, given the high obliquity of the Pluto–Charon system, it is possible that it also originated from an initially wide binary and followed a secular or semi-secular evolution, similar to MU_{69} . Similar evolutionary scenarios might also apply to the evolution of other contact binaries such as (139775) 2001 QG298 (ref. ²), as well as moons and exo-moons, as all of these form hierarchical triple systems with their host star.

Online content

Any methods, additional references, Nature Research reporting summaries, source data, extended data, supplementary information, acknowledgements, peer review information; details of author contributions and competing interests; and statements of data and code availability are available at <https://doi.org/10.1038/s41586-020-2194-z>.

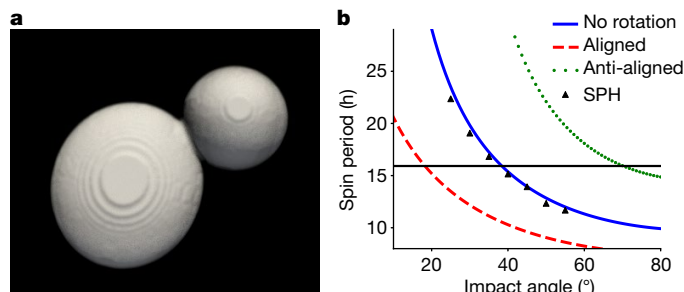


Fig. 3 | Shape and spin period of MU_{69} . **a**, Final collision outcome at an impact angle of 40° with high-material-strength composition (see Methods). **b**, Spin period as a function of the impact angle for MU_{69} . The horizontal line is the observed period, 15.92 h. The solid blue line indicates initially non-rotating progenitors. The dashed red line indicates two initially aligned rotating progenitors with a period of 10 h, and the dotted green line indicates an anti-aligned configuration. The black crosses are the results obtained from SPH simulations (see Methods).

1. Stern, S. A. et al. Initial results from the New Horizons exploration of 2014 MU_{69} , a small Kuiper belt object. *Science* **364**, eaaw9771 (2019).
2. Lacerda, P. A change in the light curve of Kuiper belt contact binary (139775) 2001 QG298. *Astron. J.* **142**, 90–98 (2011).
3. Goldreich, P., Lithwick, Y. & Sari, R. Formation of Kuiper belt binaries by dynamical friction and three-body encounters. *Nature* **420**, 643–646 (2002).
4. Richardson, D. C. & Walsh, K. J. Binary minor planets. *Annu. Rev. Earth Planet. Sci.* **34**, 47–81 (2006).
5. Perets, H. B. & Naoz, S. Kozai cycles, tidal friction, and the dynamical evolution of binary minor planets. *Astrophys. J. Lett.* **699**, 17–21 (2009).
6. Antonini, F. & Perets, H. B. Secular evolution of compact binaries near massive black holes: gravitational wave sources and other exotica. *Astrophys. J.* **757**, 27–40 (2012).
7. Grishin, E., Perets, H. B. & Fragione, G. Quasi-secular evolution of mildly hierarchical triple systems: analytics and applications for GW sources and hot Jupiters. *Mon. Not. R. Astron. Soc.* **481**, 4907–4923 (2018).
8. Grishin, E., Perets, H. B., Zenati, Y. & Michaely, E. Generalized Hill-stability criteria for hierarchical body systems at arbitrary inclinations. *Mon. Not. R. Astron. Soc.* **466**, 276–285 (2017).

9. Naoz, S., Perets, H. B. & Ragozzine, D. The observed orbital properties of binary minor planets. *Astrophys. J.* **719**, 1775–1783 (2010).
10. Lidov, M. L. The evolution of orbits of artificial satellites of planets under the action of gravitational perturbations of external bodies. *Planet. Space Sci.* **9**, 719–759 (1962).
11. Kozai, Y. Secular perturbations of asteroids with high inclination and eccentricity. *Astron. J.* **67**, 591–598 (1962).
12. Naoz, S. The eccentric Kozai–Lidov effect and its applications. *Annu. Rev. Astron. Astrophys.* **54**, 441–489 (2016).
13. Fabrycky, D. & Tremaine, S. Shrinking binary and planetary orbits by Kozai cycles with tidal friction. *Astrophys. J.* **669**, 1298–1315 (2007).
14. Porter, S. B. & Grundy, W. M. KCTF evolution of trans-Neptunian binaries: connecting formation to observation. *Icarus* **220**, 947–957 (2012).
15. Veillet, C. et al. The binary Kuiper-belt object 1998 WW31. *Nature* **416**, 711–713 (2002).
16. Petit, J. M. et al. The extreme Kuiper belt binary 2001 QW₃₂₂. *Science* **322**, 432–434 (2008).
17. Luo, L., Katz, B. & Dong, S. Double-averaging can fail to characterize the long-term evolution of Lidov–Kozai cycles and derivation of an analytical correction. *Mon. Not. R. Astron. Soc.* **458**, 3060–3074 (2016).
18. Rein, H. & Liu, S.-F. REBOUND: an open-source multi-purpose *N*-body code for collisional dynamics. *Astron. Astrophys.* **537**, A128 (2012).
19. Rein, H. & Spiegel, D. S. IAS15: a fast, adaptive, high-order integrator for gravitational dynamics, accurate to machine precision over a billion orbits. *Mon. Not. R. Astron. Soc.* **446**, 1424–1437 (2015).
20. McKinnon, W. B. et al. The solar nebula origin of (486958) Arrokoth, a primordial contact binary in the Kuiper belt. *Science* **367**, eaay6620 (2020).
21. Thirouin, A. & Sheppard, S. S. Light curves and rotational properties of the pristine cold classical Kuiper belt objects. *Astron. J.* **157**, 228–247 (2019).
22. Parker, A. H. & Kavelaars, J. J. Collisional evolution of ultra-wide trans-Neptunian binaries. *Astrophys. J.* **744**, 139–152 (2012).
23. Perets, H. B. Binary planetesimals and their role in planet formation. *Astrophys. J. Lett.* **727**, 3 (2011).
24. Funato, Y., Makino, J., Hut, P., Kokubo, E. & Kinoshita, D. The formation of Kuiper belt binaries through exchange reactions. *Nature* **427**, 518–520 (2004).
25. Heggie, D. C. Binary evolution in stellar dynamics. *Mon. Not. R. Astron. Soc.* **173**, 729–787 (1975).
26. Grundy, W. et al. Mutual orbit orientations of transneptunian binaries. *Icarus* **334**, 62–78 (2019).
27. Schäfer, C. et al. A smooth particle hydrodynamics code to model collisions between solid, self-gravitating objects. *Astron. Astrophys.* **590**, A19 (2016).
28. Goldreich, P., Lithwick, Y. & Sari, R. Planet formation by coagulation: a focus on Uranus and Neptune. *Annu. Rev. Astron. Astrophys.* **42**, 549–601 (2004).
29. Nesvorný, D., Li, R., Youdin, A. N., Simon, J. B. & Grundy, W. M. Trans-Neptunian binaries as evidence for planetesimal formation by the streaming instability. *Nat. Astron.* **3**, 808–812 (2019).
30. Canup, R. M. A giant impact origin of Pluto–Charon. *Science* **307**, 546–550 (2005).

Publisher's note Springer Nature remains neutral with regard to jurisdictional claims in published maps and institutional affiliations.

© The Author(s), under exclusive licence to Springer Nature Limited 2020

Methods

Lidov–Kozai secular evolution

Let us consider the evolution of a binary KBO due to LK secular evolution. Let the inner binary start with an initial separation of $a_0 = \alpha r_H$, eccentricity e_0 and mutual inclination i_0 . The Hill radius is $r_H = a_{\text{out}}(m_{\text{in}}/3M_\odot)^{1/3}$. The most stable orbit is around $\alpha_H \approx 0.4$ (ref. ⁸). The minimal eccentricity required for collision is

$$e_{\text{coll}} = 1 - \frac{R_{\text{tot}}}{\alpha r_H} \quad (2)$$

Using the standard LK formula, the maximal eccentricity is

$$e_{\text{max}}^2 = 1 - \frac{5}{3}(1 - e_0^2)\cos^2 i_0 \quad (3)$$

For a collision occur, we require that $e_{\text{max}} \geq e_{\text{coll}}$, which yields the critical inclination i_0^c

$$\cos i_0^c \approx \sqrt{\frac{6}{5(1 - e_0^2)} \frac{R_{\text{tot}}}{\alpha r_H}} = \frac{0.037}{\sqrt{1 - e_0^2}} \left(\frac{\alpha}{0.3}\right)^{-1/2} \quad (4)$$

such that collisions occur for $|\cos i_0| \leq |\cos i_0^c|$. Here, $R_{\text{tot}}/r_H \ll 1$ has been expanded to linear order. The probability for collision can be expressed in terms of integrating over the distribution function $f_{a,\theta}(a, \theta)$ and where $\theta \equiv \cos i$. For uniform independent distribution in $\cos i$, as inferred from KBO observations⁹, the probability is

$$P(e_0) = \int_{a_{\text{min}}}^{a_{\text{max}}} f_a(a) \theta_c(a) da \quad (5)$$

where $\theta_c(a)$ is given by equation (4).

Inclination angle at impact. From the conservation of $\sqrt{1 - e^2} \cos i = \text{const} \equiv j_z$ the inclination at impact is

$$\cos i_{\text{coll}} = \frac{\sqrt{1 - e_0^2} \cos i_0}{\sqrt{1 - e_{\text{coll}}^2}} = \sqrt{1 - e_0^2} \cos i_0 \sqrt{\frac{\alpha r_H}{2R_{\text{tot}}}} \quad (6)$$

To find the impact angle i_{coll} , we invert equation (6):

$$i_0 = \arccos\left(\cos i_{\text{coll}} \sqrt{\frac{2R_{\text{tot}}}{\alpha r_H}}\right) \quad (7)$$

To find the observed obliquity $i_{\text{coll}} = 98^\circ$, the critical inclination is at least $|\cos i_0| \leq 0.00585$, ($89.33^\circ \leq i_0 \leq 90.66^\circ$) for $\alpha = 0.1$, which is unlikely. Moreover, for $\alpha \leq 0.1$, collisions are unlikely regardless of the initial inclination, owing to the effects of oblateness, as shown below.

Effects of oblateness. Small KBOs might not have spherical shapes, in which case their gravitational potential is not spherical. Such a configuration induces extra precession on the orbit which can considerably affect the secular evolution. The leading term is encapsulated in a dimensionless parameter J_2 , which is related to ratio of the axes, or the polar and equatorial radii of the bodies³¹. Planets are mostly spherical, and their deviation is small $-J_2 \approx 10^{-3}$ for Earth and around $J_2 = 0.014$ for Jupiter—and is related to the flattening of the planets induced by their rotations. In the case of the components of MU₆₉, the objects are highly non-spherical and J_2 could be large. Using the principal moments of inertia of an oblate spheroid, we have $J_2 = [1 - (c/a)^2]/5$, which is around $J_2 \approx 0.18$ for the primary component and $J_2 \approx 0.1$ for the secondary component.

The additional precession may quench the LK oscillations if it is too strong. To quantify the effects of the additional precession we can

define a dimensionless quantity, ε_{rot} , that measures the ratio between the LK-induced and the oblateness-induced precessions^{32,33}

$$\varepsilon_{\text{rot}} = \frac{3}{2} J_2 \frac{m_{\text{in}}}{m_{\text{out}}} \frac{a_{\text{out}}^3 (1 - e_{\text{out}}^2)^{3/2} R_1^2}{(\alpha r_H)^5} \quad (8)$$

Setting $\varepsilon_{\text{rot}} = 3/2$ leads to the definition of the Laplace radius^{33,34} in terms of the Hill radius, $r_L \equiv \alpha_L r_H$ where

$$\alpha_L = \left(J_2 \frac{m_{\text{in}}}{m_{\text{out}}}\right)^{1/5} \frac{(a_{\text{out}}^3 R_1^2)^{1/5}}{r_H} (1 - e_{\text{out}}^2)^{3/10} = 0.03 \left(\frac{J_2}{0.2}\right)^{1/5} \left(\frac{R_1}{11 \text{ km}}\right)^{2/5} \quad (9)$$

leading to³² $\varepsilon_{\text{rot}} = 1.5(\alpha/\alpha_L)^{-5}$. It has been previously shown that the maximal eccentricity attained is given by the implicit expression for $\cos i_0 = 0$ (their equation 50):

$$\frac{\varepsilon_{\text{rot}}}{3} \left[\frac{1}{(1 - e_{\text{max}}^2)^{3/2}} - 1 \right] = \frac{9}{8} e_{\text{max}}^2 \quad (10)$$

Expanding in $\varepsilon_{\text{rot}} \ll 1$ and $e_{\text{max}}^2 \approx 1$

$$e_{\text{max}} \approx 1 - \frac{2}{9} \varepsilon_{\text{rot}}^{2/3} \quad (11)$$

A collision can occur only if $e_{\text{coll}} < e_{\text{max}}$ or if

$$\alpha_{\text{coll}} > \left(\frac{3}{2}\right)^{2/7} \alpha_L^{10/7} \left(\frac{2}{9} \frac{r_H}{R_{\text{tot}}}\right)^{3/7} \approx 0.12 \quad (12)$$

Note that a similar analysis can be performed for tidal distortions or relativistic corrections³². In this case, they are much weaker than the rotational effects.

Non-secular Lidov–Kozai evolution

In the previous section we considered the evolution due to secular LK evolution. In the semi-secular (semi-LK) regime^{6,7}, short-term fluctuations can substantially change the evolution. In the following we discuss the overall effects of such short-term perturbations. The strength of the perturbations is encapsulated in the single averaging parameter^{7,17}:

$$\varepsilon_{\text{SA}} \equiv \left(\frac{a_1}{b_{\text{out}}}\right)^{3/2} \sqrt{\frac{m_{\text{out}}}{m_{\text{in}}}} = \frac{\alpha^{3/2}}{\sqrt{3}(1 - e_{\text{out}}^2)^{3/2}} \approx 0.1 \left(\frac{\alpha}{0.3}\right)^{3/2} \quad (13)$$

One important quantity is the (averaged) z angular momentum $\bar{j}_z = \sqrt{1 - e_0^2} \cos i_0$, assuming that i_0 and e_0 have their mean value.

In this case, j_z is no longer conserved, but its value averaged over the outer orbit, \bar{j}_z , is conserved. The eccentricity of the orbit becomes unbound once the fluctuation in \bar{j}_z ($\Delta \bar{j}_z$) is larger than its initial value, namely $\Delta \bar{j}_z > \bar{j}_z$. The fluctuation has been estimated analytically^{7,17}, and can be used to show that the eccentricity is unbound if

$$\cos i_0 \sqrt{1 - e_0^2} \lesssim \frac{9}{8} \bar{\varepsilon}_{\text{SA}} \approx 0.118 \left(\frac{\alpha}{0.3}\right)^{3/2} \quad (14)$$

where $\bar{\varepsilon}_{\text{SA}} = \varepsilon_{\text{SA}}(1 + 2\sqrt{2}e_{\text{out}}/3) \approx 1.039\varepsilon_{\text{SA}}$ has been defined for convenience.

The width of the non-secular semi-LK regime increases with α , whereas the width of the secular LK regime decreases with increasing α . Comparing equation (4) and equation (14) yields the transitional separation α_t found in equation (1).

Spin period

There is little evidence for structural changes of MU₆₉ since its formation, and the spin period is believed to be primordial¹. In our model, the collision is gentle and occurs at relatively low velocities

Article

($v_{\text{esc}} = 442.4 \text{ cm s}^{-1}$ for our nominal density and $v_{\text{esc}} = 3.128 \text{ cm s}^{-1}$ for the lower density of 0.5 g cm^{-3} assumed in ref. ¹), such that almost any impact parameter (or impact angle) is allowed. Therefore, to obtain the observed spin period, we can use the standard arguments of angular momentum conservation and derive the impact parameter (or impact angle) that yields the desired spin rate.

Consider triaxial ellipsoidal bodies i with masses m_i and axes $a_i \geq b_i \geq c_i$, with $i=1, 2$. We assume that the major axes a_i are parallel, similar to the observed object, and that the collision occurs in parallel with the major axes. The largest moment of inertia is $I_3^{(i)} = m_i(a_i^2 + b_i^2)/5$.

After the collision the distance between the centre of masses of the joint body and each centre of the ellipsoid is r_i . Then the principal moment of inertia of the joint body is

$$I_3^{\text{tot}} = I_3^{(1)} + I_3^{(2)} + m_1 r_1^2 + m_2 r_2^2 = \sum_{i=1}^2 \frac{m_i}{5} (a_i^2 + b_i^2 + 5r_i^2)$$

Now, the ellipsoids collide with relative velocity v_{esc} and impact parameter b . The orbital angular momentum is $L_z = \mu b v_{\text{esc}}$, where $\mu = m_1 m_2 / (m_1 + m_2)$ is the reduced mass. If the two bodies are non-rotating, then the joint angular frequency is

$$\Omega = \frac{L_z}{I_3^{\text{tot}}} = \frac{5\mu b v_{\text{esc}}}{m_1(a_1^2 + b_1^2 + 5r_1^2) + m_2(a_2^2 + b_2^2 + 5r_2^2)} \quad (15)$$

If the individual bodies are rotating around the z axis with frequencies Ω_i , the additional angular momentum of each body is $I_3^{(i)} \Omega_i$ for $i=1, 2$, and thus equation (15) becomes

$$\Omega = \frac{5\mu b v_{\text{esc}} + m_1(a_1^2 + b_1^2)\Omega_1 + m_2(a_2^2 + b_2^2)\Omega_2}{m_1(a_1^2 + b_1^2 + 5r_1^2) + m_2(a_2^2 + b_2^2 + 5r_2^2)} \quad (16)$$

For an impact angle θ , the distance of the point of contact to the centre of each ellipsoid is $\xi_i = \sqrt{a_i^2 \cos^2 \theta + b_i^2 \sin^2 \theta}$. The impact parameter is related to the impact angle by $\sin \theta = b / (\xi_1 + \xi_2) = b/d$. The distances from the centre of mass are $r_1 = m_2 d / (m_1 + m_2)$ and $r_2 = m_1 d / (m_1 + m_2)$ and the spin rate is

$$\Omega = \frac{5\mu d v_{\text{esc}} \sin \theta + m_1(a_1^2 + b_1^2)\Omega_1 + m_2(a_2^2 + b_2^2)\Omega_2}{5\mu d^2 + m_1(a_1^2 + b_1^2) + m_2(a_2^2 + b_2^2)} \quad (17)$$

Figure 3 shows the spin-period dependence on the impact angle for the typical parameters of MU₆₉. The spin period is $P = 2\pi/\Omega$, where Ω is given by equation (17), and when there is no internal rotation, $\Omega_1 = \Omega_2 = 0$. We see that an impact angle of about 40° gives the observed spin period. We have performed hydrodynamical simulations based on the code of ref. ²⁷ that qualitatively agree with our assumptions and produce similar results. Typical classical KBOs could have primordial spin periods³⁵ with comparable contributions to the angular momentum budget. Recently, it was found²¹ that the mean cold classical KBO spin period is $9.48 \pm 1.53 \text{ h}$. Generally, there is no reason for the spin vectors of each body to be correlated, so on average the contribution is zero. In extreme cases, the spin vector of both objects could be aligned or anti-aligned with the orbital angular momentum. In these cases, a large range of impact angles and spin configurations are possible, resulting in the observed spin period after the collision. For a typical period of 10 h, the impact angle is about 20° in the aligned case, and about 70° in the anti-aligned case.

N-body stopping conditions and tests

We impose a stopping condition that the distance between the two bodies is less than their mutual radius. During the non-secular highly eccentric passage, the change in the pericentre q is much faster than the

inner orbital period (this is the definition of the non-secular regime), and hence the orbital elements are not reliable at this stage. Once the simulation stops it records the orbital elements at impact, which we use for our statistics, but these are not involved in the stopping condition. From the output we know the closest approach at impact. We have tested the stopping condition by varying it to be slightly smaller or larger than the q found in the first run. Indeed, when the stopping condition was below q the objects did not collide and the code continued running. We thereby concluded that the collision is physical and reliable.

Extended Data Table 1 shows the merger fractions from the simulations. The total merger fraction f_i is the total number of mergers divided by the initial number of runs, multiplied by the relative fractions of the inclination distribution, assuming that no mergers occur outside the sampled inclination distribution. The fraction f_{80-100} is calculated in the same way, except that the only mergers considered are those where the mutual inclination during the merger is within the designated boundaries of 80° – 100° . For example, for $\alpha = 0.2$, the merger fraction is $78/200 = 0.39$. Multiplied by the range of the inclination distribution, $f_i = 0.39 \times 0.3 \approx 0.12$ and the high-obliquity merger fraction is $f_{80-100} = 9/200 \times 0.3 \approx 0.014$. For $\alpha = 0.3$, the merger fraction is $99/250 = 0.396$. Multiplied by the range of the inclination distribution, $f_i = 0.396 \times 0.4 = 0.158$ and the high-obliquity merger fraction is $f_{80-100} = 12/250 \times 0.4 \approx 0.019$.

Impact modelling

We perform hydrodynamical collision simulations using our SPH code²⁷, which treats self-gravity, gas, fluid, elastic and plastic solid bodies that have a material strength, including a porosity and fracture model that can be applied for small-body collisions^{36,37}. In order to treat numerical rotational instabilities, a tensorial correction scheme³⁸ is implemented. The miluphCUDA code is implemented with CUDA, and runs on graphics processing units (GPUs), with an improvement of approximately one to two orders of magnitude for a single GPU compared to a single central processing unit (CPU). The code has previously been successfully applied to several studies involving impact processes^{36,37,39–47}.

For the porosity treatment, we implement the P - α model^{48,49}, in which the pores are much smaller than the spatial resolution and cannot be modelled explicitly. Here, the total change in the volume depends both on the compaction or collapse of the pore space and on the compression of the solid material that constitutes the matrix. The dependence is expressed in terms of a porous material pressure P and density ρ as $P/\rho = P_s/\rho_s$, where P_s and ρ_s are the pressure and density of the solid matrix material, respectively. The distention parameter $\bar{\alpha} = \rho_s/\rho$ is the ratio between the solid matrix material and the porous material densities, and relates to the porosity ψ via $\psi = 1 - 1/\bar{\alpha}$. For the solid matrix material we use the Tillotson equation of state (EOS) parameters⁵⁰ with a reduced bulk modulus of $A = 2.67 \times 10^8 \text{ Pa}$ (the leading term in the EOS) to take into account the smaller elastic wave speeds in porous materials compared to solid materials, consistent with previous work⁵¹. Our matrix density is chosen to be 2 g cm^{-3} , about the same as that used previously⁵², which leads to a 50% porosity for our fiducial bulk density for MU₆₉, 1 g cm^{-3} . The matrix density and the initial porosity are both in rough agreement with what might be expected from an object of this origin and size range. In particular, the former constrains the rock-ice mass ratio to be about 3–4 (depending on the exact choice of silicate grain density), which could be compatible with this type of KBO^{53–56}. However, we note that given the uncertainties involved, we seek only to obtain a rough estimate of the density that will permit us to test our working hypothesis. We then also run simulations with 75% porosity and half the previous bulk density to establish the qualitative differences between these two setups.

For collisions between small porous bodies, compressibility is limited by the crush curve for $\bar{\alpha}$ for typical pressures, instead of by the Tillotson

EOS parameters. We thereby choose three sets of crush-curve parameters⁵², using a simple quadratic crush curve⁵⁷:

$$\bar{\alpha} = 1 + (\bar{\alpha}_0 - 1) \frac{(P_s - P)^2}{(P_s - P_e)^2} \quad (18)$$

where $\bar{\alpha}_0 = 2$, P_e is the transition pressure between the elastic and plastic regimes and P_s is the pressure of full compaction. Both P_e and P_s are listed in Extended Data Table 2. As ref. ⁵² treats comet 67P/Churyumov–Gerasimenko, which belongs to a class of much smaller and active objects, we assume MU₆₉ is probably fluffier and more porous. Hence, our low-strength crush-curve values correspond to the previous high-strength values⁵², and taking the same modelling approach we then increment the parameters in each subsequent model by one order of magnitude.

Fracture and brittle failure are treated using the Grady and Kipp fragmentation prescription^{58–60}, which is based on randomly distributed flaws in the material following a Weibull distribution with material-dependent parameters. The lowest activation threshold strain, κ , derived from the Weibull distribution, is given by $\kappa = kV^{-1/m}$, where V is the volume of the brittle material and k and m are the material-dependent Weibull parameters. We adopt $m = 9.5$ for pressure-dependent failure⁶¹. The volume is calculated given the dimensions of the MU₆₉ binary. From the material strength parameters K and G , Young's modulus E may be calculated as $E = (9KG)/(3K + G)$. Here $K = 2.67 \times 10^8$ Pa, which is the leading term in the Tillotson EOS, and $G = 1.6 \times 10^8$ Pa. Finally, for undamaged material, $\kappa = Y_T/E$, where Y_T is the tensile strength given in table 30 of ref. ⁵². k may thus be extracted and is $k = 10^{47}$, 2×10^{39} and $2 \times 10^{28} \text{ m}^{-3}$ for the low-, medium- and high-strength-material setups, respectively. Damage accumulates when the local tensile strain reaches the activation threshold of a flaw.

For the plasticity model we use a pressure-dependent yield strength⁶² following the implementation of ref. ⁶¹. The yield stress Y_i is different for damaged and intact material. For intact material, the yield stress is $Y_i = Y_0 + \mu_i P / (1 + \mu_i P / (Y_M - Y_0))$, where Y_0 is the cohesion (again see table 30 of ref. ⁵²), μ_i is the coefficient of friction and Y_M is the shear strength at $P = \infty$. We adopt $\mu_i = 1.5$ (ref. ⁶¹) and a typical $Y_M = 1.5 \times 10^9$ Pa (ref. ⁶⁰), which is appropriate for an object composed of ice, rock and organics. For $P = 0$, we recover the pressure-independent form $Y_i = Y_0$. For damaged material the yield stress is $Y_d = \mu_d P$, where μ_d is the coefficient of friction of the damaged material. Here we take $\mu_d = 0.6$, following ref. ⁶¹, and thus fully damaged particles still undergo some shear stress.

Extended Data Fig. 1 shows additional results of our simulated impacts. We obtain the rotation period of MU₆₉ using the nominal density of 1 g cm^{-3} only when using the high-strength-material parameters. Medium-strength (Extended Data Fig. 1a) or low-strength (Extended Data Fig. 1b) materials deform MU₆₉ and do not produce the observed shape of a gently merged contact binary. If the nominal density is halved (0.5 g cm^{-3}), the impact velocity v_{esc} is lower, which produces less deformation in our simulations. Even medium-strength material parameters generate a gently merged contact binary for virtually all impact angles (Extended Data Fig. 1c, d). Here, we used the 55° impact angle, for which the observed spin period of MU₆₉ is approximately obtained. In Extended Data Fig. 2 the shape is considerably deformed after the collision if the impact velocity is larger than $v = 10v_{\text{esc}}$ using high-strength material parameters. The same velocity with weaker material parameters leads to a complete disruption of MU₆₉.

Our simulations were performed for a grid of impact angles, assuming pre-alignment of the two lobes. Simulating higher impact angles and low- and medium-strength-material compositions causes the two lobes to interact in other ways: in some cases they hit and create contact craters and then roll on top of each other; in other cases they collide, bouncing off each other instead of rolling, and then return to re-collide following a (now) shorter orbital period. These formation channels may also generate compatible shapes but, so far, not the exact rotation

period of MU₆₉. A full investigation of the collision phase space must also include the initial self-rotation of each lobe in addition to inclined hits. This requires a huge collision phase space, exceeding the scope of this work, and necessitates a dedicated hydrodynamical study. Preliminary results (in preparation) indicate that such an approach may yield more channels through which the unique orientation of MU₆₉ might be generated, besides the successful cases for pre-aligned binary components that are shown here.

Our standard resolution is 5×10^5 SPH particles. We have additionally preformed simulations with 10^5 and 2.5×10^5 particles. Test simulations were performed on the TAMNUN GPU cluster at the Technion Institute in Israel and production runs on the bwForCluster BinAC at the University of Tübingen, Germany.

Data availability

The data that support the findings of this study are available from the corresponding author upon reasonable request.

- Murray, C. D. & Dermott, S. F. *Solar System Dynamics* (Cambridge Univ. Press, 1999).
- Liu, B., Muñoz, D. J. & Lai, D. Suppression of extreme orbital evolution in triple systems with short-range forces. *Mon. Not. R. Astron. Soc.* **447**, 747–764 (2015).
- Grishin, E., Lai, D. & Perets, H. B. Chaotic quadruple secular evolution and the production of misaligned exomoons and warm Jupiters in stellar multiples. *Mon. Not. R. Astron. Soc.* **474**, 3547–3556 (2018).
- Tremaine, S., Touma, J. & Namouni, F. Satellite dynamics on the Laplace surface. *Astron. J.* **137**, 3706–3717 (2009).
- Thirouin, A., Noll, K. S., Ortiz, J. L. & Morales, N. Rotational properties of the binary and non-binary populations in the trans-Neptunian belt. *Astron. Astrophys.* **569**, A3 (2014).
- Wandel, O. J., Schäfer, C. M. & Maindl, T. I. Collisional fragmentation of porous objects in planetary systems. In *Proc. 1st Greek–Austrian Workshop Extrasolar Planetary Systems* (eds Maindl, T. I., Varvoglis, H. & Dvorak, R.) 225–242 (2017).
- Haghighipour, N., Maindl, T. I., Schäfer, C. M. & Wandel, O. J. Triggering the activation of main-belt comets: the effect of porosity. *Astrophys. J.* **855**, 60 (2018).
- Speith, R. *Improvements of the Numerical Method of Smoothed Particle Hydrodynamics*. Habilitation thesis, Univ. of Tübingen (2006).
- Dvorak, R., Maindl, T. I., Burger, C., Schäfer, C. & Speith, R. Planetary systems and the formation of habitable planets. *Nonlinear Phenom. Complex Syst.* **18**, 310–325 (2015).
- Maindl, T. I. et al. Impact induced surface heating by planetesimals on early Mars. *Astron. Astrophys.* **574**, A22 (2015).
- Haghighipour, N., Maindl, T. I., Schäfer, C., Speith, R. & Dvorak, R. Triggering sublimation-driven activity of main belt comets. *Astrophys. J.* **830**, 22 (2016).
- Schäfer, C. M. et al. Numerical simulations of regolith sampling processes. *Planet. Space Sci.* **141**, 35–44 (2017).
- Burger, C., Maindl, T. I. & Schäfer, C. M. Transfer, loss and physical processing of water in hit-and-run collisions of planetary embryos. *Celestial Mech. Dyn. Astron.* **130**, 2 (2018).
- Malamud, U., Perets, H. B., Schäfer, C. & Burger, C. Moonfalls: collisions between the Earth and its past moons. *Mon. Not. R. Astron. Soc.* **479**, 1711–1721 (2018).
- Malamud, U., Perets, H. B., Schäfer, C. & Burger, C. Collisional formation of massive exomoons of superterrestrial exoplanets. *Mon. Not. R. Astron. Soc.* **492**, 5089–5101 (2020).
- Malamud, U. & Perets, H. B. Tidal disruption of planetary bodies by white dwarfs – I: A hybrid SPH-analytical approach. *Mon. Not. R. Astron. Soc.* **492**, 5561–5581 (2020).
- Malamud, U. & Perets, H. B. Tidal disruption of planetary bodies by white dwarfs – II: Debris disc structure and ejected interstellar asteroids. *Mon. Not. R. Astron. Soc.* **493**, 698–712 (2020).
- Herrmann, W. Constitutive equation for the dynamic compaction of ductile porous materials. *J. Appl. Phys.* **40**, 2490–2499 (1969).
- Carroll, M. & Holt, A. C. Suggested modification of the P – α model for porous material. *J. Appl. Phys.* **43**, 759–761 (1972).
- Jutzi, M., Michel, P., Hiraoka, K., Nakamura, A. M. & Benz, W. Numerical simulations of impacts involving porous bodies. II. Comparison with laboratory experiments. *Icarus* **201**, 802–813 (2009).
- Leleu, A., Jutzi, M. & Rubin, M. The peculiar shapes of Saturn's small inner moons as evidence of mergers of similar-sized moonlets. *Nat. Astron.* **2**, 555–561 (2018).
- Jutzi, M., Benz, W., Toliou, A., Morbidelli, A. & Brasser, R. How primordial is the structure of comet 67P? Combined collisional and dynamical models suggest a late formation. *Astron. Astrophys.* **597**, A61 (2017).
- Rotundi, A. et al. Dust measurements in the coma of comet 67P/Churyumov–Gerasimenko inbound to the sun. *Science* **347**, aaa3905 (2015).
- Malamud, U. & Prialnik, D. Modeling Kuiper belt objects Charon, Orcus and Salacia by means of a new equation of state for porous icy bodies. *Icarus* **246**, 21–36 (2015).
- Lorek, S., Gundlach, B., Lacerda, P. & Blum, J. Comet formation in collapsing pebble clouds. What cometary bulk density implies for the cloud mass and dust-to-ice ratio. *Astron. Astrophys.* **587**, A128 (2016).
- Fulle, M. et al. The dust-to-ices ratio in comets and Kuiper belt objects. *Mon. Not. R. Astron. Soc.* **469**, S45–S49 (2017).
- Jutzi, M., Benz, W. & Michel, P. Numerical simulations of impacts involving porous bodies. I. Implementing sub-resolution porosity in a 3D SPH hydrocode. *Icarus* **198**, 242–255 (2008).

Article

58. Grady, E. D. & Kipp, E. Dynamic fracture and fragmentation. In *High-Pressure Shock Compression of Solids* (eds Asay, J. R. & Shahinpoor, M.) 265–322 (Springer, 1993).
59. Benz, W. & Asphaug, E. Impact simulations with fracture. I – Method and tests. *Icarus* **107**, 98 (1994).
60. Benz, W. & Asphaug, E. Catastrophic disruptions revisited. *Icarus* **142**, 5–20 (1999).
61. Jutzi, M. SPH calculations of asteroid disruptions: the role of pressure dependent failure models. *Planet. Space Sci.* **107**, 3–9 (2015).
62. Collins, G. S., Melosh, H. J. & Ivanov, B. A. Modeling damage and deformation in impact simulations. *Meteorit. Planet. Sci.* **39**, 217–231 (2004).

Acknowledgements We acknowledge discussions with D. C. Fabrycky and E. Kite. H.B.P. acknowledges support from the MINERVA Center for Life Under Extreme Planetary Conditions and the Kingsley Fellowship at Caltech. C.M.S. and O.W. acknowledge support by the High Performance and Cloud Computing Group at the Zentrum für Datenverarbeitung of the University of Tübingen, the state of Baden-Württemberg through bwHPC and the German

Research Foundation (DFG) through grant number INST 37/935-1 FUGG. C.M.S. acknowledges support from the DFG through grant number 398488521.

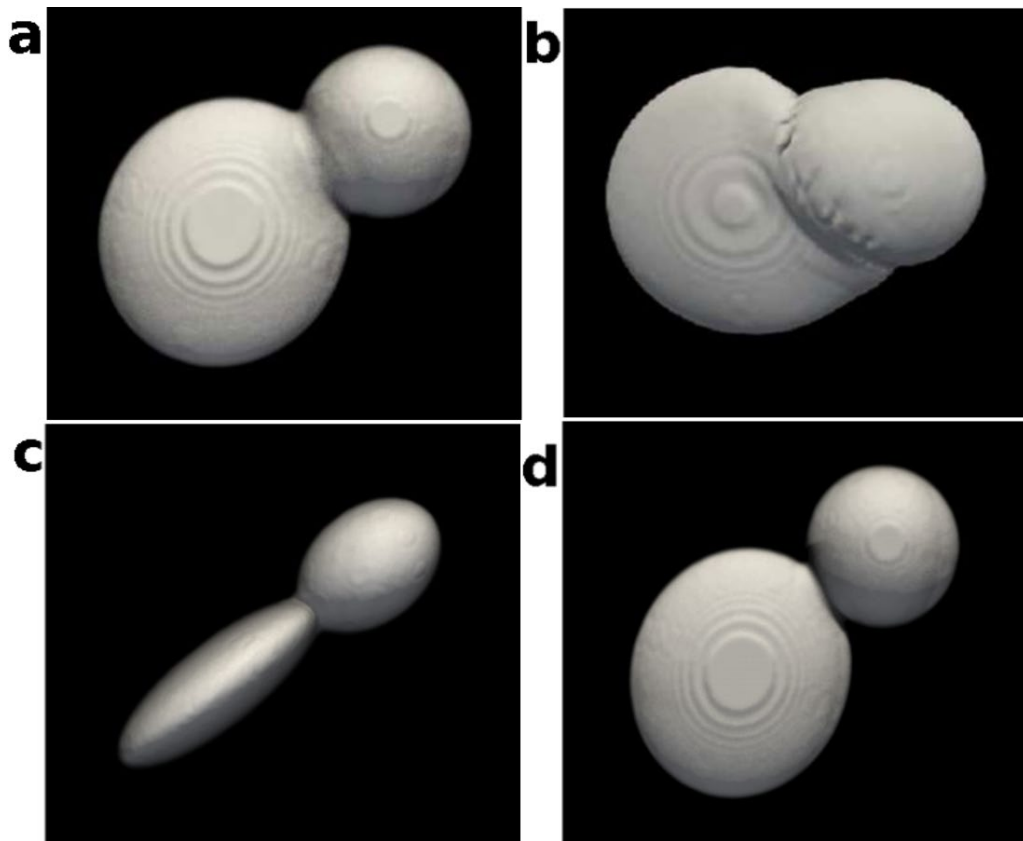
Author contributions E.G. led the project, performed the analytic calculations and ran and analysed the *N*-body simulations. U.M. led the hydrodynamical modelling, its analysis and wrote the hydrodynamical sections. H.B.P. initiated the project and supervised it, suggested the main ideas and concepts and took part in all of the analysis. O.W. ran the hydrodynamical simulations and was the main developer of the porosity module in the hydrodynamical code. C.M.S. developed the hydrodynamical code and supervised the development of the porosity module. E.G. and H.B.P. wrote the main text.

Competing interests The authors declare no competing interests.

Additional information

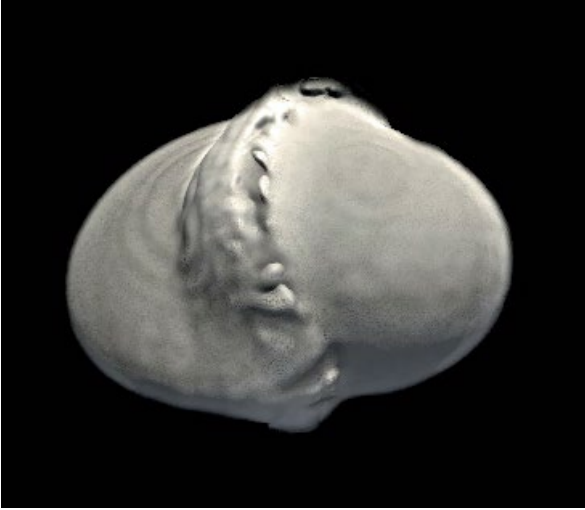
Correspondence and requests for materials should be addressed to E.G.

Reprints and permissions information is available at <http://www.nature.com/reprints>.



Extended Data Fig. 1 | Additional results of the collision models. a, 40° impact angle, medium-strength material. **b,** 40° impact angle, low-strength material. **c, d,** Low-density model (0.5 g cm^{-3}) with an impact angle of 55° and medium-strength material. The edge (**c**) and face (**d**) views are given.

Article



Extended Data Fig. 2 | Additional results of the collision models. 5° impact angle, high-strength material and large escape velocity, $v = 10v_{\text{esc}}$.

Extended Data Table 1 | Merger rate of the binaries in the non-secular regime

	0.2	0.3	0.4	U
N_m	78	99	114	101
N_{80-100}	9	12	18	15
f_i	0.12	0.16	0.18	0.16
f_{80-100}	0.014	0.019	0.029	0.024

N_m , total number of mergers.

N_{80-100} , number of mergers with inclinations $80^\circ < i < 100^\circ$.

f_i , total merger fraction normalized to the inclination sampling rate.

f_{80-100} , merger fraction for only those mergers with inclinations $80^\circ < i < 100^\circ$.

Article

Extended Data Table 2 | Crush curve, plasticity and fragmentation parameters

Type	P_e (Pa)	P_s (Pa)	Y_0 (Pa)	Y_T (Pa)
Low-strength	10^4	10^6	10^4	10^3
Medium-strength	10^5	10^7	10^5	10^4
High-strength	10^6	10^8	10^6	10^5

A Versatile Smoothed Particle Hydrodynamics Code for Graphic Cards

Christoph M. Schäfer^a, Oliver J. Wandel^a, Christoph Burger^{a,b}, Thomas I. Maindl^b, Uri Malamud^c, Sergey K. Buruchenko^d, Rafael Sfair^e, Hugo Audiffren^{a,f}, Evita Vavilina^a, Philip M. Winter^g

^aInstitut für Astronomie und Astrophysik, Auf der Morgenstelle 10, 72076 Tübingen, Germany

^bDepartment of Astrophysics, University of Vienna, Tuerkenschanzstr. 17, 1180 Vienna, Austria

^cPhysics Department, Technion - Israel Institute of Technology, Haifa, Israel 3200002

^dSouth Ural State University, 456776 Zababachina 9-115 Snezhinsk, Chelyabinsk Region, Russia

^eSao Paulo State University, Guaratingueta, Sao Paulo CEP 01049-010, Brazil

^fAix-Marseille University, 3 Place Victor Hugo, 13003 Marseille, France

^gInstitute for Machine Learning, Johannes Kepler University Linz, Altenberger Straße 69, 4040 Linz, Austria

Abstract

We present the second release of the now open source smoothed particle hydrodynamics code `miluphcuda`. The code is designed to run on Nvidia CUDA capable devices. It handles one to three dimensional problems and includes modules to solve the equations for viscous and inviscid hydrodynamical flows, the equations of continuum mechanics using SPH, and self-gravity with a Barnes-Hut tree. The covered material models include different porosity and plasticity models. Several equations of states, especially for impact physics, are implemented. The basic ideas of the numerical scheme are presented, the usage of the code is explained and its versatility is shown by means of different applications. The code is hereby publicly available.

Keywords: smoothed particle hydrodynamics, GPU-computing, hydrodynamics, continuum mechanics

1. Introduction

The Lagrangian meshfree particle method smoothed particle hydrodynamics (SPH) was invented by [50] and [27] to solve the hydrodynamic equations for compressible flows in astrophysical applications. During the last 40 years, it has been widely used in astrophysics to tackle a substantial number of problems. In the last two decades the field of applications have expanded vividly: SPH has been established as one of the major concepts for fluid animation and rigid-fluid coupling in computer graphics [36, 1], it was extended to continuum mechanics to model high-velocity impacts [45, 86], it is widely used in geosciences to model landslides and granular media [94, 11], and the method has been improved and extended substantially to model phase separating fluid mixtures [95], to solve the magnetohydrodynamical equations [72] and to model relativistic flows [77]. It has also been used to solve the non-linear Schrödinger equation [62]. The SPH scheme has proven to be an advantageous method to solve all kind of different partial differential equations (PDEs). Since the most astrophysical applications have to include gravity as the most dominating force, gravitational interactions had been implemented into the SPH scheme from the early development on. Moreover, not only external gravitational sources but also the self-gravity of the simulated flow or

solid body can be considered. Especially tree algorithms for the treatment of the long range gravitational force have been combined with SPH [32].

Several SPH codes have been developed in the recent years and we present in the following the codes that have been published under the GNU General Public License. The list is most certainly incomplete and we want to apologize any omitted code. The first popular code GADGET-2 by [85] is a massively parallel TreeSPH code, which is still widely used in the astrophysical community. A more recent and modern code from the astrophysical community is the PHANTOM code by [73]. It is a parallel, modular and low-memory smoothed particle hydrodynamics and magnetohydrodynamics code with focus on stellar, galactic, planetary and high energy astrophysics. The second version of the GASOLINE code, GASOLINE2, has also been published under the GPLv2 license [92]. The code concentrates also on astrophysical problems with a special focus on cosmology. Another versatile SPH code written is SPHERAL++ by [70]. Since the field of applications of the scheme has been broadened thoroughly in the recent decade, modern and versatile codes outside of the astrophysical community have emerged. PySPH is reproducible and high-performance framework for smoothed particle hydrodynamics is developed by [74]. It is implemented in a mix of Python and Cython. The user writes pure Python code and the high-performance computing (HPC) code is generated automatically. PySPH includes solver for fluid and solid mechanics and supports both

Email address: ch.schaefer@uni-tuebingen.de (Christoph M. Schäfer)

OpenMP and MPI. Another code to study free-surface flows is DualSPHysics [21], which is the very first SPH framework featuring a modern design and GUI interface (DesignSPHysics). AQUAgpusph [18] is a 3D, OpenCL accelerated SPH solver for GPUs. GPUSPH by Hérault et al. [35], which has been originally a port of the freely available SPHysics Fortran code to Nvidia’s CUDA library, is now a standalone project and supports multiple GPUs. PersianSPH is an open-source code and features elastic-plastic soil behaviour and elastic-plastic solid behaviour [41]. SPHERA [2] is also publicly available and supports the simulation of flooding including the transport of solid bodies, bed-load transport, damage on electrical substations and fast landslides in rocks and solids. Another versatile code within the astrocommunity is SWIFT by Schaller et al. [82]. Recent simulations with SWIFT included up to 100 million SPH particles [39]. It can directly read GADGET-2 output files and shows tremendous scaling.

Here, we present the updated version of our GPU SPH code `miluphcuda`¹. The new version is published under the GPLv3 license and available on github via <https://github.com/christophmschaefer/miluphcuda>. Originally, the code has been developed to model collisions between solid, self-gravitating objects in an astrophysical context. The basic implementation is described in [78], and until today, the code is solely applied in the astronomy community. The code handles one-, two- and three-dimensional problems. It has been used to study the activation of porous and non-porous asteroids [31, 30], collisions between Earth and its past moons [52], collisional formation of moons [53], impact cratering [93], the formation of Arrokoth [28], transfer and loss of water in hit-and-run collisions [13, 12] and sampling of granular material [81] among other applications. Recent extensions include further porosity models, a module to solve the Navier-Stokes equations, and more sophisticated equation of states like ANEOS.

The outline of this paper is as follows. The next section summarizes the characteristics of the code as presented in Schäfer et al. [78] and provides a comprehensive description of the new extensions. Section 3 shows some of the recent applications and numerical tests to provide an overview of the possibilities of the code. We will conclude in the final section and present details about the code and its structure in the appendix.

2. Physical and numerical method

In this section, we present the different physical models, their numerical implementations, and further aspects of `miluphcuda`.

The basic idea of the SPH scheme is to transform a system of partial differential equations to a system of or-

dinary differential equations, which can be solved by standard integrators. For this transformation the partial differential equations are approximated in two steps: First, with an average over all spatial field quantities by the help of the convolution with the kernel function and second by a discretisation of this average. For an introduction to the fundamental ideas of SPH, we refer to the comprehensive review articles by Benz [7], Monaghan [65], Monaghan [66], Liu and Liu [47] and Monaghan [63]. In the following, we present the SPH equations for viscid and inviscid hydrodynamics and continuum mechanics as implemented in the code. The different modules implemented in the code allow for the simulation of various different astrophysical objects: By the use of the sole hydrodynamical module, one can model a gaseous accretion disc, both viscous and inviscid. By adding the self-gravity module, the gravitational field produced by the disc is also included. The solid module allows to model brittle, rocky materials, such as smaller, non-porous planetesimals. Adding the porosity module, the code can be used to simulate porous objects like porous asteroids, comets and Kuiper belt objects. Larger planetesimals or dwarf planets can be simulated with a combination of the solid or hydro module with the self-gravity module. The different strength models included in the solid module allow to model brittle or granular materials, e.g. a layer of granular regolith on a brittle and porous asteroid.

2.1. Hydrodynamics

The flow of a fluid is completely described by its velocity field $\mathbf{v}(\mathbf{x}, t)$, and two thermodynamic field quantities, where usually the density $\varrho(\mathbf{x}, t)$ and the pressure $p(\mathbf{x}, t)$ are chosen. The conservation laws for mass, momentum and energy determine the dynamics and lead to a set of PDEs which can be solved with SPH for all locations \mathbf{x} and times t .

The Euler equation describes the flow of an inviscid, ideal fluid. It reads in Lagrangian representation

$$\varrho \frac{d\mathbf{v}}{dt} = -\nabla p, \quad (1)$$

with the velocity \mathbf{v} , the density ϱ and the pressure p . By the use of the identity

$$\frac{1}{\varrho} \nabla p = \frac{1}{\varrho^{2-\lambda}} \nabla \left(\frac{p}{\varrho^{\lambda-1}} \right) + \frac{p}{\varrho^\lambda} \nabla \frac{1}{\varrho^{1-\lambda}}, \quad (2)$$

one can derive the following two equivalent SPH representations,

$$\frac{d\mathbf{v}_a}{dt} = - \sum_b m_b \frac{p_a + p_b}{\varrho_a \varrho_b} \nabla W_{ab} \quad (3)$$

for $\lambda = 1$, and

$$\frac{d\mathbf{v}_a}{dt} = - \sum_b m_b \left[\frac{p_a}{\varrho_a^2} + \frac{p_b}{\varrho_b^2} \right] \nabla W_{ab} \quad (4)$$

for $\lambda = 2$.

¹`miluph` is pronounced [mailv]

2.2. Viscous flows

The extension of the Euler equation for viscous, Newtonian fluids is the Navier-Stokes equation. It reads in Lagrangian representation

$$\varrho \frac{d\mathbf{v}}{dt} = -\nabla p + \nabla \cdot T, \quad (5)$$

where T denotes the viscous stress tensor. The viscous stress tensor accounts for the internal friction of the flow. For a Newtonian fluid, where the viscosity depends linearly on the gradient of the velocity field, it is given by

$$T^{\alpha\beta} = \eta \left[\frac{\partial v^\alpha}{\partial x^\beta} + \frac{\partial v^\beta}{\partial x^\alpha} - \frac{2}{3} \delta^{\alpha\beta} \frac{\partial v^\gamma}{\partial x^\gamma} \right] + \zeta \delta^{\alpha\beta} \frac{\partial v^\gamma}{\partial x^\gamma} \quad (6)$$

with the dynamic viscosity coefficient η and the bulk viscosity coefficient ζ . The kinematic viscosity coefficient ν is the ratio between the dynamic viscosity coefficient and the density of the fluid, $\nu = \eta/\varrho$. The term in the parentheses in eq. (6) represents the traceless part of the viscous stress tensor and is called viscous shear stress tensor. The numerical treatment and solution of the Navier-Stokes equation is demanding because of the second derivatives of the velocities. We follow the approach by [23] and calculate the derivatives of the velocity components for particle a according to

$$\frac{\partial v_a^\alpha}{\partial x^\beta} = \sum_b \frac{m_b}{\varrho_b} (v_b^\alpha - v_a^\alpha) \frac{\partial W_{ab}}{\partial x^\beta} \equiv v_a^{\alpha\beta}. \quad (7)$$

The viscous stress tensor for particle a can be calculated via

$$T_a^{\alpha\beta} = \eta_a \left[v_a^{\alpha\beta} + v_a^{\beta\alpha} \right] - \frac{2}{3} \delta^{\alpha\beta} v_a^{\gamma\gamma}. \quad (8)$$

In a second step, the accelerations due to the viscous stress are determined via

$$\frac{dv_a^\alpha}{dt} = \sum_b m_b \frac{T_a^{\alpha\beta} + T_b^{\alpha\beta}}{\varrho_a \varrho_b} \frac{\partial W_{ab}}{\partial x^\beta}. \quad (9)$$

If the partial derivatives of the velocities are not calculated with eq. (7), but with the numerical equivalent SPH sum

$$\frac{\partial v_a^\alpha}{\partial x^\beta} = \frac{1}{\varrho_a} \sum_b m_b (v_b^\alpha - v_a^\alpha) \frac{\partial W_{ab}}{\partial x^\beta}, \quad (10)$$

the accelerations are determined via

$$\frac{dv_a^\alpha}{dt} = \sum_b m_b \left[\frac{T_a^{\alpha\beta}}{\varrho_a^2} + \frac{T_b^{\alpha\beta}}{\varrho_b^2} \right] \frac{\partial W_{ab}}{\partial x^\beta}. \quad (11)$$

The bulk part of the Navier-Stokes equation can also be used to define an artificial viscosity that prevents mutual particle penetration and does not yield unwanted spurious shear. A possible ansatz for an artificial bulk viscosity was successfully applied in planet-disk interaction simulations

in [79]: the bulk part of the viscous stress tensor is $\zeta \nabla \cdot \mathbf{v}$, which leads to an additional acceleration for particle a

$$\left. \frac{dv_a}{dt} \right|_{\text{bulk}} = \sum_b m_b \zeta_{ab} \frac{(\nabla \cdot \mathbf{v})_a + (\nabla \cdot \mathbf{v})_b}{\varrho_a \varrho_b} \nabla_a W_{ab}, \quad (12)$$

or

$$\left. \frac{dv_a}{dt} \right|_{\text{bulk}} = \sum_b m_b \zeta_{ab} \left[\frac{(\nabla \cdot \mathbf{v})_a}{\varrho_a^2} + \frac{(\nabla \cdot \mathbf{v})_b}{\varrho_b^2} \right] \nabla_a W_{ab}, \quad (13)$$

in case of the other SPH representation, respectively. The bulk viscosity coefficient ζ_{ab} for the interaction between particles a and b is

$$\zeta_{ab} = \begin{cases} -f \bar{h}_{ab}^2 \overline{(\nabla \cdot \mathbf{v})_{ab}} \bar{\varrho}_{ab} & \text{for } (\mathbf{v}_a - \mathbf{v}_b) \cdot (\mathbf{x}_a - \mathbf{x}_b) \\ 0 & \text{else.} \end{cases} \quad (14)$$

The term \bar{q}_{ab} denotes an abbreviation for the average $\frac{1}{2}(q_a + q_b)$ for any quantity q and f a parameter to scale the effect of the artificial bulk viscosity, usually set to 1.

2.3. Solid body mechanics

The implementation of solid body mechanics with fragmentation in our code follows the ideas and concepts of [86] and [8]. We refer for the thorough description of our implementation in [78] and present the basic equations in the following.

For a perfect elastic material, the conservation of momentum reads

$$\varrho \frac{d\mathbf{v}^\alpha}{dt} = \frac{\partial \sigma^{\alpha\beta}}{\partial x^\beta}, \quad (15)$$

where the stress tensor $\sigma^{\alpha\beta}$ is built up by the pressure p and the traceless deviatoric stress tensor $S^{\alpha\beta}$

$$\sigma^{\alpha\beta} = -p \delta^{\alpha\beta} + S^{\alpha\beta}. \quad (16)$$

The conservation of the internal energy u is given by

$$\frac{du}{dt} = -\frac{p}{\varrho} \frac{\partial v^\alpha}{\partial x^\alpha} + \frac{1}{\varrho} S^{\alpha\beta} \dot{\varepsilon}^{\alpha\beta}. \quad (17)$$

Here, $\dot{\varepsilon}^{\alpha\beta}$ denotes the strain rate tensor for small deformations

$$\dot{\varepsilon}^{\alpha\beta} = \frac{1}{2} \left(\frac{\partial v^\alpha}{\partial x^\beta} + \frac{\partial v^\beta}{\partial x^\alpha} \right). \quad (18)$$

Additionally, an equation for the time evolution of the deviatoric stress tensor $S^{\alpha\beta}$ is required to describe the dynamics of the solid body, which is called the constitutive equation. For an perfectly elastic behaviour, we choose Hooke's law, where the stress depends linearly on the strain, which yields using the Jaumann rate eventually

$$\frac{dS^{\alpha\beta}}{dt} = 2\mu \left(\dot{\varepsilon}^{\alpha\beta} - \frac{1}{3} \delta^{\alpha\beta} \dot{\varepsilon}^{\gamma\gamma} \right) + S^{\alpha\gamma} R^{\gamma\beta} - R^{\alpha\gamma} S^{\gamma\beta}, \quad (19)$$

with the shear modulus μ and the rotation rate tensor $R^{\alpha\beta}$

$$R^{\alpha\beta} = \frac{1}{2} \left(\frac{\partial v^\alpha}{\partial x^\beta} - \frac{\partial v^\beta}{\partial x^\alpha} \right). \quad (20)$$

2.4. Strength models

A solid material does not deform perfectly elastic for all experienced strains. Once the applied strain exceeds the elastic limit, the deformation becomes plastic. The transition from an elastic to a plastic state of a substance is characterised by a stress state. The stress at which the material starts deforming plastically is called yield stress, and the condition for plastic deformation is the yield criterion. For an isotropic medium, the yield criterion is a symmetric function of the principle stresses σ_i

$$f(\sigma_1, \sigma_2, \sigma_3) = \text{const.} \quad (21)$$

The constant on the righthandside is material dependent and related to the particular yield limit. Since f is a symmetric function of the principle stresses, the stress components can be expressed by the invariants of the stress tensor

$$f(I_1, J_2, J_3) = \text{const.} \quad (22)$$

In the original code, we have implemented the elementary von Mises yield strength to model plastic behaviour of solid bodies, and noted already the shortcoming of this simplistic model. Following [20] and [37], we have added two additional strength models suitable for the modelling of granular material and a pressure dependent yield strength model, which is applicable to rocks and interplays with the fragmentation model for brittle materials by Grady and Kipp [78].

2.4.1. Von Mises yield stress

In the von Mises yield stress model [91], the deviatoric stress is limited once it reaches a constant yield strength limit Y_M . At first, the second invariant of the stress tensor is computed via

$$J_2 = \frac{1}{2} S^{\alpha\beta} S_{\alpha\beta}, \quad (23)$$

for each individual particle, and the limiting factor f_Y is calculated according to

$$f_Y = \min \left[Y_M^2 / 3J_2, 1 \right]. \quad (24)$$

Then, the deviatoric stress, which was integrated using eq. (19), is limited

$$S^{\alpha\beta} \rightarrow f_Y S^{\alpha\beta}. \quad (25)$$

2.4.2. Drucker-Prager and Mohr-Coulomb yield criterion

The Drucker-Prager yield strength depends on the pressure and is applicable to model rocky materials. The condition for plasticity reads

$$\sqrt{J_2} = A - BI_1, \quad (26)$$

where I_1 denotes the first invariant of the stress tensor ($I_1 = \text{tr}[\sigma^{\alpha\beta}]$) and J_2 the second invariant given by eq. (23). The

two material constants A and B are the so-called Drucker-Prager constants. The criterion is related to the Mohr-Coulomb yield criterion, and the constants A , B can also be expressed in terms of cohesion c and angle of internal friction φ of the material via

$$A = \frac{6c \cos \varphi}{\sqrt{3}(3 - \sin \varphi)}, \quad B = \frac{2 \sin \varphi}{\sqrt{3}(3 - \sin \varphi)}. \quad (27)$$

2.4.3. Pressure dependent yield criterion in combination with damage model

In our fracture model [78], the reduction in strength under tensile loading is expressed via a scalar damage variable $0 \leq D \leq 1$, where $D = 0$ corresponds to intact material and $D = 1$ to a totally fractured material that cannot undergo any tension or deviatoric stress. In this sense, a material with $D = 0.5$ experiences half the deviatoric stress and tension of an undamaged material with $D = 0$. In order to relate the fragmentation model with the yield strength for plastic flow, [20] calculate a damage dependent yield strength in the following way. Undamaged, intact substances have a pressure dependent yield strength of

$$Y_P = c + \frac{\mu p}{1 + \mu p / (Y_M - c)}, \quad (28)$$

where μ is the coefficient of internal friction, given by $\mu = \tan \varphi$, c is the cohesion and Y_M the shear strength at infinite pressure. For totally damaged materials, the deviatoric stress is usually set to zero. However, as pointed out by [37], it is important to take into account the friction in totally damaged material, e.g., shattered rocks. Therefore, for totally damaged materials with $D = 1$, the yield strength is not vanishing but dominated by the pressure and given by

$$Y_D = \mu_D p, \quad (29)$$

where μ_D now denotes the coefficient of internal friction of the totally damaged, granular material. For partially damaged materials, the yield strength is determined according to

$$Y = (1 - D)Y_P + DY_D, \quad (30)$$

while $Y \leq Y_P$ is ensured. As soon as one particle exceeds the yield strength, the deviatoric stress is reduced according to eq. (25), with the limiting factor

$$f_Y = \min \left[Y / \sqrt{J_2}, 1 \right]. \quad (31)$$

2.5. Porosity Models

Macroscopic porosity can be easily modelled with SPH by simply adding macroscopic voids on the scale of the particle volume to the initial distribution. However, sub-resolution porosity can be troublesome. Various sub-resolution porosity models exist in the literature and are applied to porous materials from metals to rocks. Although

originally the p - α -model was developed to study impacts into metal shielding, we have first implemented it for the simulation of porous, rocky objects such as comets and asteroids.

2.5.1. The p - α -model

The p - α -model by [33], which was modified by [38], relates the porous pressure p of a material to the solid pressure p_s and the distention α . The main idea is to separate the volume change in a porous material into the pore collapse of the porous material and the compression of the matrix material. The distention is defined by

$$\alpha = \frac{\varrho_s}{\varrho} = \frac{1}{1 - \phi}, \quad (32)$$

with the solid density ϱ_s , the porous density ϱ and the porosity ϕ . The porous pressure is calculated with the empirically found equation using the distention α and the pressure of the solid material p_s [17]

$$p = \frac{1}{\alpha} p_s(\varrho_s, u_s) = \frac{1}{\alpha} p_s(\alpha \varrho, u), \quad (33)$$

where ϱ_s and u_s are the density and the energy of the solid, and ϱ and u of the porous material. The crush-curve relates the pressure to the porosity and yields a maximum pressure which the porous material can undergo before crushing. This gives an additional boundary condition for the pressure in the simulation. Two crush-curves are currently implemented. One being quadratic and the other having two regimes with parameters gained by fitting function 34 to the crush-curve of porous pumice, using a compression testing machine. In the plastic regime the distention α is computed as follows

$$\alpha(p) = \begin{cases} (\alpha_e - \alpha_t) \frac{(p_t - p)^{n_1}}{(p_t - p_e)^{n_1}} + (\alpha_t - 1) \frac{(p_s - p)^{n_2}}{(p_s - p_e)^{n_2}} + 1 & \text{if } p_e < p < p_t \\ (\alpha_t - 1) \frac{(p_s - p)^{n_2}}{(p_s - p_e)^{n_2}} + 1 & \text{if } p_t \leq p < p_s \\ 1 & \text{if } p \geq p_s, \end{cases} \quad (34)$$

where p_e is the pressure where the transition from the elastic to the plastic regime happens, p_s the pressure where the porous material is fully compacted and the density equals the matrix density ($\alpha = 1$) and the pressure p_t indicates a transition between the two regimes with different slopes n_1 and n_2 [38].

The distention is evolved in time depending on the pressure as follows

$$\dot{\alpha} = \frac{d\alpha}{dp} \frac{dp}{dt}. \quad (35)$$

One of the most important aspects of the p - α -model implementation is the check function for the timestep. The relation between the pressure and the distention is an implicit. However, to solve it explicitly, one has to make sure that the distention is resolved correctly. Hence, the distention has to follow the crush-curve since each distention value relates to a specific maximum pressure value. If the integrated distention yields a pressure beyond the

p_e [Pa]	p_t [Pa]	p_s [Pa]	α_0	α_t	n_1	n_2
10^6	6.8×10^7	2.13×10^8	3.45	1.90	12	3

Table 1: Parameters for the crush-curve which were used for the plot and the simulation in figure 1.

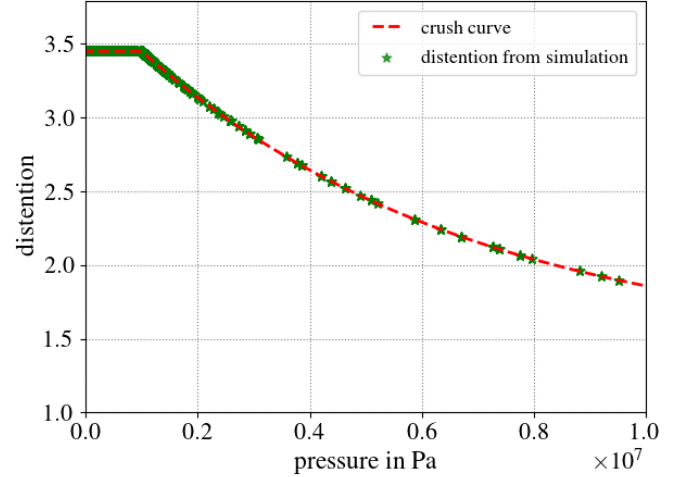


Figure 1: Relation between the distention α and the pressure p . The initial distention is $\alpha_0 = 3.45$ and until p_e is reached the deformation is elastic and $\frac{d\alpha}{dt} = 0$.

maximum pressure for this specific distention value, the time step has been too coarse, the crush-curve is not reproduced correctly and the timestep has to be reduced, the integration step has to be repeated. To ensure this critical boundary condition our integrators have either an distention or a pressure check function where the change of the previous to the current value is calculated and if these values are too large the timestep is decreased accordingly, and the current step is recalculated with the lowered timestep. In order to validate the porous model, we have simulated the impact of a nylon, spherical projectile into a cube of pumice in three dimensions. Figure 1 shows the pressure-distention values of the SPH particles from the impact. The distention α lies exactly on the crush-curve and thus resolving the timestep accordingly with crush-curve parameters shown in table 1. The simulation was a nylon sphere impacting into a pumice cube. The parameters for the Tillotson equation of state (EOS) are those of solid rock with a volume $V = 216 \text{ cm}^3$ and a matrix density $\varrho_s = 2325.3 \text{ kg/m}^3$. The impactor sphere has the Tillotson EOS parameters of nylon with a radius $r = 7 \text{ mm}$, a density $\varrho_s = 1185 \text{ kg/m}^3$ and an impact velocity $v_{\text{imp}} = 2.58 \text{ km s}^{-1}$.

A shock wave test was performed which travels in one spatial dimension. The material was porous aluminium with an initial distention of $\alpha_0 = 1.275$. The crush-curve parameters are shown in table 2 and the Tillotson EOS parameters are those of aluminium. The cylinder has a height $h = 2 \text{ cm}$ and a radius of $r = 0.2 \text{ cm}$. A constant velocity is set in the z -direction with $v_z = -45.8 \text{ cm s}^{-1}$. The

p_e [Pa]	p_s [Pa]	c_0 [m s ⁻¹]	c_e [m s ⁻¹]
8×10^7	7×10^8	5.35×10^3	4.11×10^3

Table 2: Parameters for the crush-curve which were used for the plot and the simulation in figure 2.

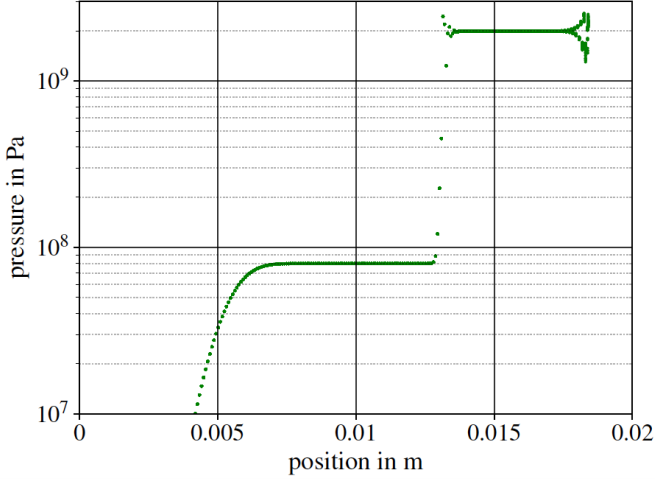


Figure 2: One dimensional shock wave in a three dimensional porous aluminium cylinder. The pressure is plotted as a function of the vertical position of the SPH particle in the cylinder. The plot shows two waves with an elastic precursor followed by the actual shock wave.

quadratic crush-curve

$$\alpha = 1 + (\alpha_e - 1) \frac{(p_s - p)^2}{(p_s - p_e)^2} \quad (36)$$

was used and $\left[\frac{d\alpha}{dp} \neq 0\right]_{\text{elastic}}$ is calculated using

$$\left[\frac{d\alpha}{dp}\right]_{\text{elastic}} = \frac{\alpha^2}{K_0} \left[1 - \left(\frac{1}{h(\alpha)^2}\right)\right] \quad (37)$$

where $K_0 = c_0^2 \varrho_0$ and

$$h(\alpha) = 1 + (\alpha - 1) \frac{c_e - c_0}{c_0(\alpha_e - 1)}, \quad (38)$$

with $\alpha_e = \alpha(p_e)$. The results are shown in figure 2. We find perfect agreement with the simulation presented by [38].

2.5.2. The ε - α -model

Another porosity model has been implemented into the code which is the so called ε - α -model [19]. The main difference between this and the above mentioned p - α -model is the calculation of the distention. In this model the distention is calculated using the volumetric strain ε_V which is given by the change in volume of an element divided by the initial volume leading to following expression:

$$\varepsilon_V = \int_{V_0}^{V'} \frac{dV}{V} = \ln\left(\frac{V'}{V_0}\right), \quad (39)$$

with V_0 as the initial and V' as the updated volume. The volumetric strain can be related to the distention α

$$\varepsilon_V = \ln\left(\frac{V'}{V_0}\right) = \ln\left(\frac{V' V_s}{V_s V_0}\right) = \ln\left(\frac{\alpha}{\alpha_0}\right), \quad (40)$$

with an ideally constant matrix volume V_s . The compaction function is defined as

$$\alpha(p) = \begin{cases} \alpha_0 e^{\kappa(\varepsilon_V - \varepsilon_e)} & \text{if } \varepsilon_e > \varepsilon_V \geq \varepsilon_x \\ 1 + (\alpha_0 e^{\kappa(\varepsilon_x - \varepsilon_e)} - 1) \left(\frac{\varepsilon_c - \varepsilon_V}{\varepsilon_c - \varepsilon_x}\right)^2 & \text{if } \varepsilon_x > \varepsilon_V > \varepsilon_c \\ 1 & \text{if } \varepsilon_V \leq \varepsilon_c, \end{cases} \quad (41)$$

with ε_e as the elastic-plastic transition strain, ε_x the threshold strain for the transition between the two compaction regimes, ε_c the threshold for full compaction, κ the exponential compaction rate and α_0 the initial distention. The parameter ε_c has to be calculated beforehand with following equation

$$\varepsilon_c = \frac{2 - 2\alpha_0 e^{\kappa(\varepsilon_x - \varepsilon_e)}}{\kappa \alpha_0 e^{\kappa(\varepsilon_x - \varepsilon_e)}} + \varepsilon_x. \quad (42)$$

In this model the distention is not calculated directly using the pressure. The change in the distention is calculated as follows

$$\dot{\alpha} = \frac{d\alpha}{d\varepsilon_V} \frac{d\varepsilon_V}{dt}. \quad (43)$$

2.5.3. Sirono-model

The Sirono porosity model implemented in the code is by [83] which was later modified by [80], and extended to different material by [26]. It is an isothermal model, which is the main difference to the two above mentioned models. It uses a slightly modified Murnaghan EOS which is an extension of the liquid EOS with a non-linear dependency of the pressure on the density

$$p(\phi) = K(\phi'_0) \left(\frac{\phi}{\phi'_0} - 1\right), \quad (44)$$

where $\phi'_0 = \frac{\varrho'_0}{\varrho_s}$ and ϱ'_0 is the reference density, i.e. the density at $p = 0$. To calculate the pressure at a given density we only need the bulk modulus $K(\phi)$ which is given by the power law

$$K(\phi) = 2\mu(\phi) = K_0 \left(\frac{\phi}{\phi_i}\right)^\gamma, \quad (45)$$

with the shear modulus $\mu(\phi)$ and $\phi_i = \varrho_i/\varrho_s$. Since there is no energy dependency in this EOS it is only used for the low velocity regime. The pressure is restricted by the compressive strength $\Sigma(\phi)$ and tensile strength $T(\phi)$. Until the pressure reaches the upper limit (the compressive strength) the deformation is elastic and once it surpasses the compressive strength the deformation process will be plastic. This changes the slope for the calculation of the pressure (equation 44) and thus deforming the material irreversibly. The pressure is limited in following way

$$p(\phi) = \begin{cases} \Sigma(\phi) & \text{if } \phi > \phi_c^+ \\ T(\phi) & \text{if } \phi < \phi_c^-. \end{cases} \quad (46)$$

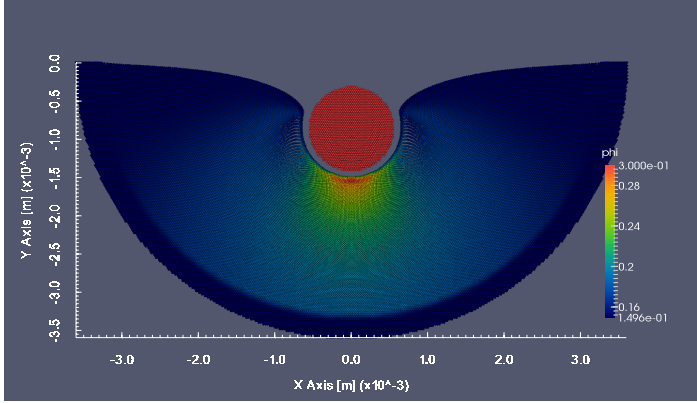


Figure 3: Crater depth of the glass bead falling into the porous dust cake. The colour mapped is the filling factor $\phi = \varrho/\varrho_s$.

The compressive strength is calculated using this equation

$$\Sigma(\phi) = \begin{cases} p_m \left(\frac{\phi_{\max} - \phi_{\min}}{\phi_{\max} - \phi_{\min} - \epsilon} - 1 \right)^{\Delta \ln 10} & \text{if } \phi \leq \phi_{\min} + \epsilon \\ p_m \left(\frac{\phi_{\max} - \phi_{\min}}{\phi_{\max} - \phi} - 1 \right)^{\Delta \ln 10} & \text{if } \phi_{\min} + \epsilon < \phi < \phi_{\max} \\ \infty & \text{if } \phi \leq \phi_{\max}, \end{cases} \quad (47)$$

with the material dependent parameters p_m , Δ , ϵ and the minimum and maximum filling factors ϕ_{\min} and ϕ_{\max} . For the test calculation presented in figure 3, the following values have been calibrated using [29] the mean pressure $p_m = 260$ Pa, $\Delta = 0.58$, $\epsilon = 0.005$, $\phi_{\min} = 0.12$ and $\phi_{\max} = 0.58$. The tensile strength is given by

$$T(\phi) = -10^{a+b\phi} \text{ Pa}, \quad (48)$$

with $a = 2.8$ and $b = 1.48$. Figure 3 shows one of these (in this case two dimensional) simulations where a glass bead falls into the porous dust cake (SiO_2). The used values for the setup are shown in table 3.

2.6. Equation of states

The equation of state relates the thermodynamic state variables and closes the system of PDEs. It is normally defined as a relation between the density, pressure and temperature or internal energy of a specific material. Depending on the physical regimes, different EOS are applied. There is no universal EOS, which can be used for all materials under all conditions, liquid, gaseous or solid. Therefore, various EOS are implemented and available in the code. In the original version, the available EOS were liquid EOS, Murnaghan EOS, and Tillotson EOS. In the new version, we have added the EOS for polytropic gas, isothermal gas, ideal gas, and ANEOS. The use of porosity models require additional porosity-dependent pressure relations, which are implemented via special EOS for these porous materials. Hence, there are several additional versions for porous materials with Tillotson EOS for the p - α -, the Sirono-, and the ϵ - α -model. Additional EOS may be included to the code straightforwardly by adding another EOS_TYPE_* to `pressure.h` and the calculation of the pressure to the kernel function in `pressure.cu`.

Physical Quantity	Value with Unit
Glass bead	
Matrix density ϱ_0	$2.54 \times 10^3 \text{ kg/m}^3$
Bulk modulus K_0	$5 \times 10^9 \text{ Pa}$
Murnaghan exponent n	4
Radius r	$0.55 \times 10^{-3} \text{ m}$
Impact velocity v_0	0.65 m s^{-1}
Dust target	
Initial filling factor ϕ_0	0.15
Matrix density ϱ_s	2000 kg/m^3
Reference density ϱ'_0	300 kg/m^3
Bulk modulus K_0	$3 \times 10^5 \text{ Pa}$
Radius r_{dust}	$3.3 \times 10^{-3} \text{ m}$
Other parameters	
Artificial viscosity α, β	0.1, 0

Table 3: Parameter table of the two dimensional crater depth validation simulations for the Sirono model.

2.6.1. Murnaghan EOS

The Murnaghan EOS can be derived from the assumption that the bulk modulus varies linearly with pressure [67]. It reads

$$p = \frac{K_0}{n} \left(\left(\frac{\varrho}{\varrho_0} \right)^n - 1 \right), \quad (49)$$

where K_0 is the bulk modulus and ϱ_0 the density in the relaxed state. The Murnaghan EOS can be used to model weakly compressible materials. In this publication, it was applied to model the gravitational collapse of a granular column, see section 3.4.

2.6.2. Tillotson EOS

A widely used non-linear EOS for simulating high-velocity impacts was introduced by [90] and can be applied over a wide range of physical conditions, while being computationally simple. It provides rudimentary distinction between the solid and vapour phase, but lacks a consistent treatment of phase changes. In the case of compressed regions ($\varrho \geq \varrho_0$) and u lower than the energy of incipient vaporization u_{iv} the equation of state reads

$$p = \left[a_T + \frac{b_T}{1 + u/(u_0 \eta^2)} \right] \varrho u + A_T \xi + B_T \xi^2, \quad (50)$$

with $\eta = \varrho/\varrho_0$ and $\xi = \eta - 1$. In case of expanded material (u greater than the energy of complete vaporization u_{cv}) the equation of state takes the form

$$p = a_T \varrho u + \left[\frac{b_T \varrho u}{1 + u/(u_0 \eta^2)} + A_T \xi \exp[-\beta_T (\eta^{-1} - 1)] \right] \quad (51)$$

$$\times \exp[-\alpha_T (\eta^{-1} - 1)^2]. \quad (52)$$

The symbols ϱ_0 , A_T , B_T , u_0 , a_T , b_T , α_T , and β_T are material dependent parameters. In the partial vaporization $u_{iv} < u < u_{cv}$, the pressure is linearly interpolated between the two values obtained via (50) and (51), respectively. The Tillotson EOS has the advantage of being computational very simple, and still sophisticated enough for the application over a wide regime of physical conditions in high pressure ranges, such as high-velocity collisions and impact cratering.

Note, that the Tillotson EOS can also yield negative pressure values for expanded ($\eta < 1$) and cold ($u < u_{iv}$) states. This corresponds to a tension in the solid material. As stated by [58], a fluid will fragment into smaller droplets at lower densities, limiting the tension. In order to consider this behaviour, a density limit parameter can be defined for each material type in the simulation. As soon as the ratio η falls below this limit, the pressure is set to zero instead of becoming negative. Additionally, there is also a compile time option which prevents negative pressure values at all.

2.6.3. ANEOS

A more sophisticated treatment of phase changes is possible with the analytic equations of state (ANEOS) package [see, e.g., 60]. ANEOS is based on calculating the Helmholtz free energy from first principles, where all relevant quantities can then be deduced from. This also holds for the temperature, which is not directly possible for the Tillotson EOS. However, ANEOS requires more than 40 input parameters (10 for the Tillotson EOS), and is not freely available. It consists of several thousand lines of FORTRAN code, which has to be utilized to produce lookup-tables, which can then be interpolated from. To enhance the thermodynamical aspects of our SPH code's material model, we have recently finished implementing ANEOS to overcome the limitations of the Tillotson EOS [?].

2.7. Fixed and variable smoothing

The code supports three different methods for SPH smoothing: Either a fixed smoothing length for each material type is set or the smoothing length varies for each particle separately. In the latter case, a fixed number of interaction partners can be set individually for each material type or the smoothing length is integrated according to the following evolution equation

$$\frac{dh}{dt} = \frac{h}{d} \nabla \cdot \mathbf{v}, \quad (53)$$

where d denotes the dimension. Additionally, an upper and lower limiter can be chosen for each material type. If two particles with differing smoothing lengths h_a and h_b interact, the kernel is calculated with their mean $\frac{1}{2}(h_a + h_b)$. The search for the interaction partners is conducted by the help of the Barnes-Hut tree. For each particle, a tree walk starting at the root of the tree is performed.

The search continues descending only into nodes that intersect with the sphere with the radius of the particle's smoothing length. Finally, individual particles in the lowest nodes (the leaves) are checked for interaction by calculating the distance and comparing to the smoothing length. Since the interaction partner search for one particle is independent from the search for the partners of another particle, the search algorithm parallelizes perfectly.

2.8. Time integrator

The default time integrator is an embedded second order Runge-Kutta integrator, which uses an additional third step to determine an adaptive time step. Its implementation is based on the description in Butcher [16]. Four more integrators are implemented: a simple Euler integrator for test purposes during new developments, two different predictor-corrector schemes, one with a prediction step of half the time step and a correction step with the whole time step and vice versa, and a special purpose coupled Heun and fourth order Runge-Kutta integrator. The time step size for all integrators is limited by the Courant condition and the artificial viscosity is also taken into account [63]

$$\Delta t \leq \text{CFL} \frac{h}{c_s + 1.2(c_s \alpha + \mu_{\max} \beta)}. \quad (54)$$

Here, CFL is the Courant number, c_s denotes the sound speed, h is the smoothing length, α and β are the artificial viscosity parameters and μ_{\max} is the maximum value of μ_{ab} from all interaction pairs. The term μ_{ab} is an approximation for the velocity divergence and calculated according to

$$\mu_{ab} = \frac{\bar{h}_{ab}(\mathbf{v}_a - \mathbf{v}_b) \cdot (\mathbf{x}_a - \mathbf{x}_b)}{(\mathbf{x}_a - \mathbf{x}_b)^2 + \varepsilon_v \bar{h}_{ab}^2}. \quad (55)$$

The term \bar{h}_{ab}^2 is the average of the smoothing lengths of particle a and b . and the factor $\varepsilon_v \bar{h}_{ab}^2$ in the denominator prevents divergence of μ_{ab} . Apart from the Courant time limit, there exist additional limit check functions to ensure convergence of the crush-curve for simulations including porosity, see section 2.5, and upper limits for an absolute change of specific values like the damage variable in simulations including brittle fracture can be specified to ensure convergence, i.e.

$$\Delta t \leq \begin{cases} \varepsilon \frac{|\xi| + \xi_{\min}}{\left| \frac{d\xi}{dt} \right|} & \text{for } \left| \frac{d\xi}{dt} \right| > 0 \\ \Delta t_{\max} & \text{else,} \end{cases} \quad (56)$$

for all quantities ξ which are integrated, where $\varepsilon < 1$ and ξ_{\min} is a measure to set the minimum time step.

In addition, a combined Heun and fourth order Runge-Kutta (RK4) integrator is implemented with intended application for circumbinary disks following the method by [88]. The Heun part is used to solve the hydrodynamical equations, i.e. to integrate the SPH equations and the

RK4 part is used to integrate the orbits of the gravitating objects. For each complete timestep in the Heun integrator, the four steps of the RK4 are performed. In every substep of the RK4 the accelerations for all gravitational point masses are calculated. At the end of timestep, both integrators are at the new time $t+\Delta t$ and the cycle restarts.

2.9. Additional gravitating bodies

An arbitrary number of purely gravitationally interacting (point-)masses may be included in the simulation. The gravitational force from these objects leads to an additional acceleration of the particles. These masses also interact mutually and their motions are integrated with the same integrator that integrates the fluid or solid body. This renders simulations possible that include more than one central object, e.g. collisions of smaller objects in a planetary system or the simulation of accretion disks around circumbinaries with one or more potentially embedded planets. The point masses are stored in additional data files and a minimum and maximum distance for the particle can be specified individually for each point mass. Once a particle comes too close or too far, it is deactivated in the simulation.

2.10. Long-range forces

Currently, `miluphcuda` allows to simulate the self-gravity of the mass distribution given by the particle distribution. The long-range forces due to the mutually gravitational interaction of the particles is either calculated directly via a N^2 algorithm or approximately using the Barnes-Hut tree [4] that is also used for the interaction partner search. The latter one may be also a starting point to implement other long-range forces like Coulomb's law. The additional acceleration due to the gravitational interaction is added to the momentum equation of the applied module, i.e. one of eqs. (1,5,15).

The self-gravity module has been validated by the simulation of an isothermal, spherical and initially uniformly rotating collapsing molecular cloud by Schäfer et al. [78]. The module is used in the three applications presented in sections 3.1 to 3.3.

3. Applications

In this section we intent to display the versatility of `miluphcuda`. We have adapted the code to various differing physical problems including hydro- and solid mechanics, with and without gravitational forces, self-gravity, strength-dominated and strengthless bodies, inviscid and viscous flows. The subsections contain exemplary simulations of various projects which make use of our code. In practice, each numerical investigation with SPH has to include a convergence study, i.e. varying number of particle numbers, varying smoothing lengths, and different values for other parameters of the method such as the artificial viscosity. Since our intention is to present many different

simulations with all available modules, we do not present these convergence studies here, and focus only on variety of applications.

3.1. Embedding realistic collision outcomes into long-term planet formation simulations

The formation of terrestrial planets is believed to proceed in several relatively distinct steps, where during the last and final phase, often termed 'late-stage accretion', planetary embryos (\sim Moon- to Mars-sized objects) and remaining smaller planetesimals eventually accrete into planets. This phase is characterized by chaotic interaction and giant collisions among large, similar-sized, gravity-dominated bodies, which shape many of a planet's final characteristics – its orbital parameters, spin and obliquity, and not least its composition, especially also volatile/water contents. Since (giant) collisions are naturally the core agent of accretion, it is crucial to study those events individually in detail. However, to obtain truly self-consistent results especially in the context of a chaotic planet formation environment it is eventually the combination of the long-term dynamical evolution of protoplanets/planetesimals with realistic outcomes of individual encounters that is necessary. We follow two different approaches for this problem, both centered around physically accurate collision simulations with `miluphcuda`. The first one is to use a catalog of collision outcomes, spanning the most relevant parts of parameter space, where the outcome of a particular collision scenario is then interpolated from (Sect. 3.1.1). The second approach is to run a dedicated SPH simulation for each occurring collision event 'on the fly', whose results are directly re-inserted into the further underlying N-body evolution (Sect. 3.1.2).

Our main aim in these applications is to study volatile/water transport, which may have been delivered to the accretion zone of Earth by successive collisions among water-carrying planetesimals and planetary embryos from the outer asteroid belt region. Even though semi-analytical models (scaling laws) to approximately predict collision outcomes have been developed in recent years [44, 43, 55], they are currently not able to reliably predict the more subtle consequences for water inventories [12], where existing studies have almost exclusively assumed oversimplified perfectly inelastic merging of water-bearing bodies. This is despite the fact that water and other volatile material is particularly susceptible to collisional fragmentation and loss processes, and thus masses as well as water contents of final terrestrial planets are considerably overestimated in most cases.

Giant collisions of similar-sized bodies (cf. Figure 4) are complex and generally super-sonic events, where strong shocks dissipate large amounts of energy, which can lead to large-scale melting and vaporization, or even eject outer layers mechanically. In addition material initially under high pressure can be released from the deep interior when bodies are (partly) disrupted (cf. Figure 6). Correct modeling of the thermodynamic response with a suitable equa-

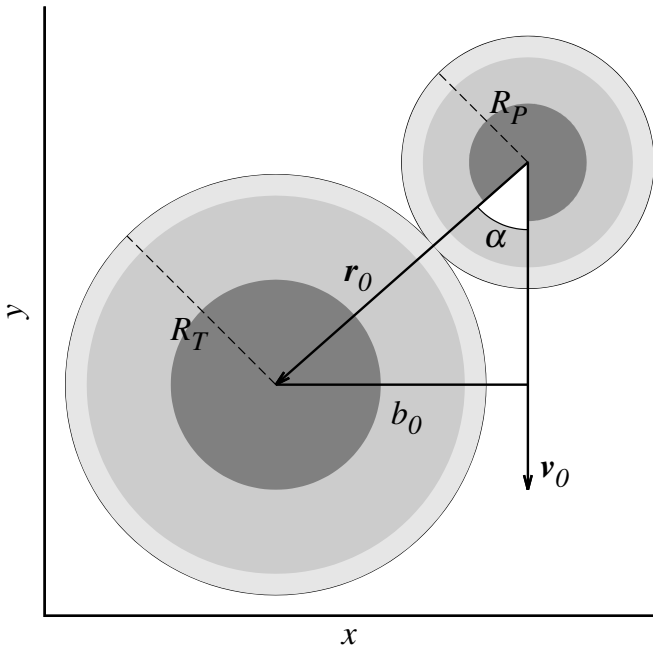


Figure 4: Collision geometry for similar-sized, differentiated bodies in a target-centric frame. $|\mathbf{v}_0|$ is the impact velocity, α the impact angle (0° for head-on).

tion of state is therefore crucial (Sect. 2.6), while the precise material rheology becomes typically less important once in the gravity-dominated regime. The majority of such encounters is more or less oblique, which makes them naturally fully 3-dimensional events, and gives rise to frequent hit-and-run outcomes (e.g., Figure 6), where the colliding bodies separate again (gravitationally) after the interaction phase.

3.1.1. Collisions catalog for protoplanetary bodies

In order to arrive at a more realistic estimate of the amount of water transported to Earth’s accretion zone, we systematically investigated the rate of water transport in collisions by performing a suite of several hundred collision simulations with `miluphcuda`. Here, we present results in terms of the fraction of water retained after a collision for different parameters of the system including collision velocity, impact angle, and the masses and water-mass fractions of the projectile and target. The resulting catalog of collisional water loss focuses on planetary embryos of masses in the Ceres to Earth range and initial water content. Table 4 lists the parameters chosen for the catalog. In order to limit the parameter space we assumed a uniform structure consisting of a basaltic silicate rock interior covered by a water ice mantle for all bodies. Our material model is based on the Tillotson equation of state [see 59] and uses the parameters given in Table 4. The Weibull parameters for the damage model are $m = 16$ and $k = 10^{61} \text{ m}^{-3}$ [68] for basalt and $m = 9.1$ and $k = 10^{46} \text{ m}^{-3}$ [42] for water ice, respectively.

The outcome in terms of the masses of the largest two surviving fragments and the water remaining on these survivors is given in the supplementary data to this article. The data is given in xlsx format with columns as described in Table 6. Visualizing our high-dimensional data is difficult. In order to properly present our catalog, we thus apply the embedding algorithm UMAP [56, 57], which allows an efficient, non-linear down-projection of our six-dimensional input space. We use the default hyperparameters for the UMAP mapping, except for `n_neighbours=15` and `min_dist=0.99`. Figure 5 visualizes the embedded dataset. Each of the original six dimensions is contributing some structure to the embedding. There are 17 clusters which are – each for itself – homogeneous in impact angle and projectile/target water mass fraction and composed of different impact velocities and masses. Although the plots are still difficult to interpret, a comparison of the color gradients indicate that the water retention of the two largest fragments is correlated with both the impact velocity and the impact angle: while the gradients of the velocity closely describe the intra-cluster gradients of the water retention, the impact angle does so with the global gradient across all clusters.

In the near future we plan to create a scheme that allows us to integrate data from an extended catalog into N-body calculations that will use predicted collision outcomes instead of perfect merging. First experiments with multi-dimensional interpolation work satisfactorily regarding the water loss, but fail in terms of predicting correct fragment sizes, positions, and velocity vectors after the impact. Therefore, we currently run a simulation campaign of thousands of collisions – enough to apply machine learning methods to predict detailed collision outcomes as they occur in planet formation simulations (Winter, Winkler, Maindl, and Schäfer, in prep.).

3.1.2. Direct N-body – SPH hybrid simulations

The direct combination of an underlying N-body computation [realized with the versatile REBOUND package, 75] with dedicated individual collision simulations has the advantage of full self-consistency and allows to precisely model all collisions at hand, including more subtle processes like water loss and transfer between colliding bodies in hit-and-run encounters. Such a direct hybrid approach has been applied only rarely and with limited resolution [25, 24], and never to follow water or other volatiles to our knowledge.

In order to ensure the flawless handover from the N-body computation to an SPH collision and back, several well-synchronized steps are necessary, implemented via a Python interface, which calls the necessary subprocesses (including `miluphcuda`) and handles communication between them. Once bodies are found to be on colliding trajectories, the N-body integration continues until they have approached to a well-defined starting distance for the SPH simulation – several times the sum of their radii to allow for the build-up of potential pre-collision tidal defor-

Parameter	Values
Total mass $M_{\text{tot}} = M_{\text{projectile}} + M_{\text{target}}$	2 M_{Ceres} (1.88×10^{21} kg), 2 M_{C} (1.47×10^{23} kg), 2 M_{G} (1.28×10^{24} kg), 2 M_{E} (1.19×10^{25} kg)
Mass ratio $\gamma = M_{\text{projectile}}/M_{\text{target}}$	0.1, 0.5, 1.0
Projectile water mass fraction w_p	0.1, 0.2
Target water mass fraction w_t	0.1, 0.2
Impact velocity v [v_{esc}]	1.0, 1.5, 2.0, 3.0, 5.0
Impact angle α [deg]	0, 20, 40, 60

Table 4: Scenario parameters of the collision catalog. The velocity v_{esc} denotes the two-body escape velocity.

Material	ρ_0 [kg/m ³]	A_T [GPa]	B_T [GPa]	E_0 [MJ/kg]	E_{iv} [MJ/kg]	E_{cv} [MJ/kg]
Basalt	2700	26.7	26.7	487	4.72	18.2
Ice	917	9.47	9.47	10	0.773	3.04
Material	α_T	β_T	a_T	b_T	μ [GPa]	Y_M [GPa]
Basalt	0.5	1.5	5	5	22.7	3.5
Ice	0.3	0.1	10	5	2.8	1

Table 5: Tillotson EOS Parameters adopted from Benz and Asphaug [9] used in the simulations for the collision catalog. The bulk modulus is set equal to A_T and B_T , shear modulus and the von Mises yield stress are denoted by μ and Y_M , respectively.

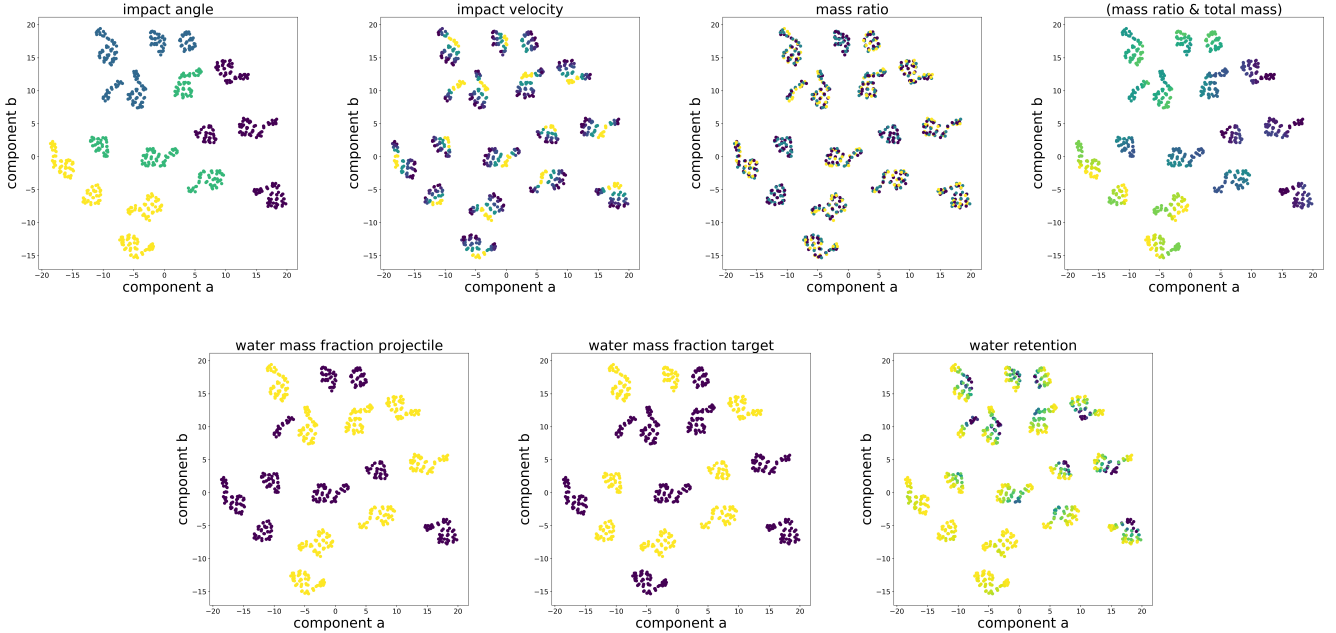


Figure 5: For visualization, the six-dimensional input space was embedded into two dimensions component a and component b using UMAP. The titles of the plots indicate the respective color codings. Note that only the water retention color code represents a result after evaluating the collision outcomes, the others represent the initial conditions.

Column	Description
v	collision velocity [v_{esc}]
alpha	collision angle [deg]
m	$M_{\text{tot}} = M_{\text{projectile}} + M_{\text{target}}$ [kg]
gamma	mass ratio $\gamma = M_{\text{projectile}}/M_{\text{target}}$
wp	projectile water mass fraction
wt	target water mass fraction
mS1	mass of survivor 1 [kg]
mS2	mass of survivor 2 [kg]
wmFS1	survivor 1 water mass fraction
wmFS2	survivor 2 water mass fraction
wretained	$1 - \frac{\text{water lost to debris [kg]}}{\text{total initial water [kg]}}$

Table 6: Column description of the collision outcome data in the supplement.

mations. The colliding bodies are initialized already with self-consistent hydrostatic profiles following Burger et al. [12], which works practically instantaneously and eliminates the need for lengthy numerical relaxation. To ensure a self-consistent (gravity) environment, the star and all other bodies in the N-body system (besides the two colliding ones) are additionally included as point masses for the whole duration of the SPH simulation. Once the collision / interaction phase is over (potential post-collision fragments have clearly separated), we first identify spatially connected fragments via an octree / friends-of-friends algorithm, followed by additional search for gravitationally bound fragments, which are then each considered a single post-collision body. Eventually their (barycenters’) positions and velocities are re-inserted into the N-body integration. The vastly different time as well as size scales of individual collisions vs. long-term N-body evolution pose particular challenges. Individual collisions cover \sim hours to days at most, while the whole planetary accretion phase lasts for several 100 Myrs. The spatial domain of individual collisions is usually considerably below 10^6 km, while the whole system covers tens of au ($\sim 10^9$ km). The capabilities of `miluphcuda` allow us to run the necessary multi-material collision simulations (including surface water layers), where the various available strength / material models (Sect. 2.4) and equations of state (Sect. 2.6) can be utilized to account for the broad range of physical states of water in an active planet formation environment. The actual conditions at the onset of some currently simulated collision however, depend on many parameters, among them the distance to the star, the body’s (especially thermal) history, and the time since the last (large) collision / impact event. For a truly holistic picture all these processes (and likely more) will have to be included eventually, which is our ultimate but not yet accomplished goal, therefore a preliminary solution is to model water inventories as

(strengthless) fluid, properties that likely resemble a surface ocean on average. Our SPH code provides the necessary fast and efficient computations to run typically \sim hundreds of dedicated collision simulations per underlying N-body scenario, where individual ones (with resolutions between 25 000 to 75 000 SPH particles) require on the order of an hour to complete (with all pre- and post-processing steps).

In order to model collisional water transport we apply this hybrid framework to an evolving system of several hundred planetary embryos and planetesimals which extends into the water-rich region beyond the ice condensation line (snow line). We include either no (very disruptive), one (accretion or erosion), or two (hit-and-run) post-collision bodies in the further N-body evolution. The rationale is that collisions between large, gravity-dominated bodies generally result in at most two large post-collision bodies besides orders-of-magnitude smaller additional debris, which has either been desiccated directly during the collision, or remaining water is otherwise likely often lost quickly, once vaporized by large-scale energy deposition during impact. An example of such a collision is illustrated in Figure 6.

3.2. Formation of massive exomoons of super-terrestrial exoplanets

Most simulation studies of giant impacts have focused on the collisional phase space conducive to the formation of Solar system planets and satellites [5]. Despite an extensive collision simulation literature, there have only been a few studies that investigated giant impacts relevant to exoplanets that are more massive than the Earth [54, 55, 48, 6], and in particular studies that focus on the formation of exosolar satellites Barr and Bruck Syal [6]. We also use `miluphcuda` in order to simulate novel scenarios which enable the formation of massive exomoons. We investigate the mass, long-term tidal-stability, composition and origin of material of such exomoons.

Since super-terrestrial planet collisions are often highly energetic, the debris discs which they generate typically require sensitive treatment which goes beyond the capabilities of the more common, Tillotson EOS. We therefore implement the M-ANEOS EOS. Our M-ANEOS parameter input files are derived from Melosh [61]. We consider differentiated impactors and targets composed of 30% iron and 70% dunite by mass. The initial setup of each simulation is calculated via a pre-processing step, in which both impactor and target are generated with relaxed internal structures, i.e. having hydrostatic density profiles and internal energy values from adiabatic compression, following the algorithm provided in appendix A of Burger et al. [12]. All our simulations have a resolution of 10^6 SPH particles.

An example of a particularly interesting simulation is shown in Figure 7. While most collisions generate a massive disk, which later evolves to coagulate into a massive satellite, we also find this rare and illustrative case in which

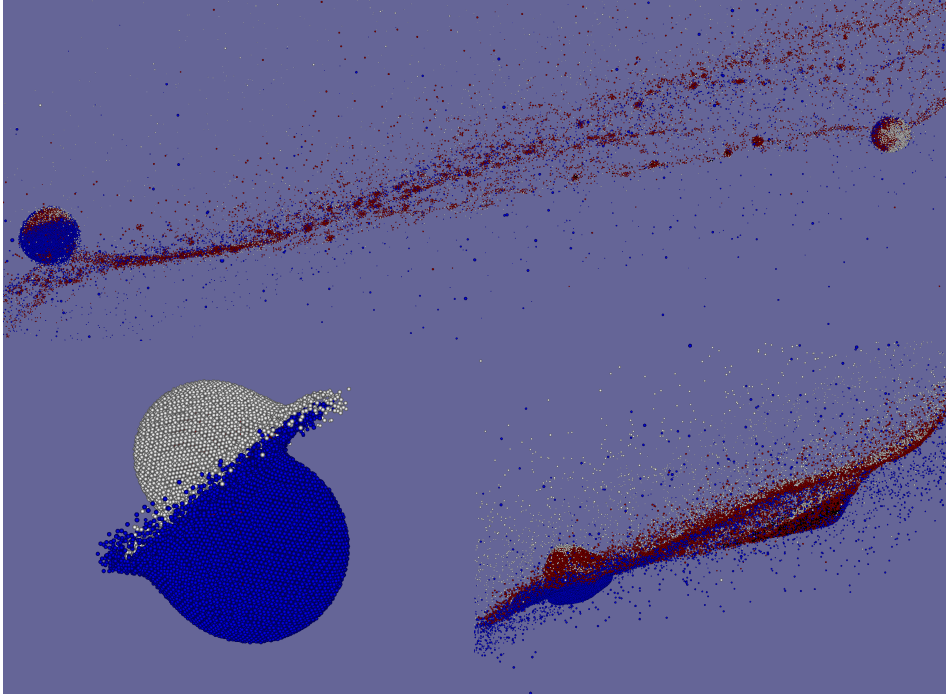


Figure 6: Snapshots of a hit-and-run collision between protoplanet-sized bodies. The impactor (white) approaches from the left. Both objects are differentiated into an iron core (black), a silicate mantle (red) and a water shell, color-coded in blue for the target and white for the impactor, to illustrate not only collisional losses but also water transfer between the bodies. Refer to Burger et al. [12] for more details.

an exomoon forms through a graze & capture scenario between a super-Earth and an Earth-sized planet. The result is an intact, planet-sized exomoon, containing about half the mass of the Earth. At this size, an exomoon can be potentially detectable using our best available observing instruments. E.g., see the Hunt for Exomoons with Kepler (HEK) [40] initiative. We note that to date, there has not been any confirmed detection of an exomoon, hence this finding may be important.

We validate our model by successfully reproducing the results obtained in a predecessor study [6] which uses a different, adaptive mesh refinement (AMR) code. Indeed our results are broadly compatible with theirs, and the data follows similar trends.

3.3. Ring structures around Chariklo and Haumea

All the four giant planets of our solar system host ring structures in equatorial orbits within their Roche radius, and recently at least two other bodies are found to host ring structures: the Centaur 10199 Chariklo [10] and the dwarf planet Haumea [69]. The characteristics of the rings vary widely, but in many systems it is possible to find dense and narrow rings mainly composed by particles with sizes ranging from centimetres to a tens of meter bodies. In such case the particles' interaction cannot be neglected, what poses a computational challenge for usual N-body approach usually applied to study the particles dynamics.

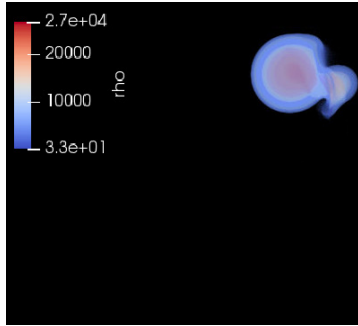
Furthermore, dense rings are optically thick and highly collisional systems. The typical impacts might happen at multiple times the metal escape velocity, so the collisions

outcome cannot be safely determine from the extrapolation of the usual prescriptions [e.g., 44].

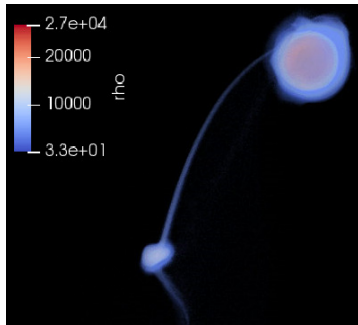
Some of the issues mentioned above can be solved using SPH simulations. The parallel nature of the technique allows an efficient way to compute the mutual interaction among a large ensemble of particles. Besides being possible to take into account the material properties, SPH simulations also allow the inclusion of fragmentation and porosity effects, so the collisions are treated in a more realistic way.

Our code has been successfully adapted to simulate the system of Chariklo aiming to explain the formation the region depleted of material between the two rings, and to investigate the interaction of the ring particles with a putative satellite that may inhabit this gap. We employed the Tillotson equation of state, and the initial setup consisted in a small section of 10×5 km of the rings filled with $20\text{-}\mu\text{m}$ bodies, each one being composed by particles spaced by 1 m. The number of bodies where determined to result in an optical depth comparable to the observed value. The self-gravity was taken into account, and all bodies were assumed to be composed by ice particles subject to the gravitational force of Chariklo and the satellite, both treated as external forces. The motion of the particles were followed in a rotating frame that moves with the satellite and periodic boundary conditions were applied in the azimuthal direction.

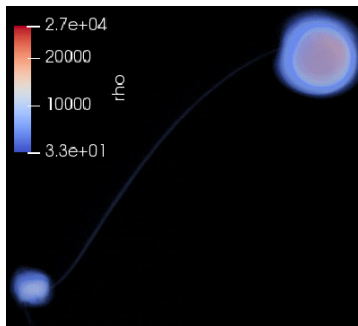
To validate the results obtained with `miluphcuda` we compared the simulation outcome with a similar setup integrated using the IAS15 algorithm, a high-order numer-



(a) 0.17 hours



(b) 1.5 hours



(c) 3 hours

Figure 7: The first three hours of a giant impact between a $0.83 M_{\oplus}$ impactor and $6.4 M_{\oplus}$ target, obtaining a graze & capture scenario, which generates an intact, $0.5 M_{\oplus}$ exomoon. The colour scheme shows the density in units of $\text{kg} \times \text{m}^{-3}$.

ical integrator implemented in REBOUND [76]. Preliminary results show that both runs are in agreement and the SPH code performed well, even more when we consider that N-body run required some simplification in the effects that can be added to the simulation.

3.4. Collapse of a granular column

To show the applicability of the code to model granular medium, we have simulated the three dimensional collapse of a granular column under gravitation following a validation simulation from Szevc [87], who compared simulations to experimental results by Lube et al. [49]. Initially, a granular column of radius R_0 and height $H_0 = aR_0$ (with $a = 0.55$ in the simulation presented here) is placed on the ground. The granular material has a density of

$\rho = 2.6 \text{ g/cm}^3$, a sound speed of 100 m/s, an internal angle of friction of 30 deg and zero cohesion. Depending on the ratio a between initial height and radius, Szevc [87] and Lube et al. [49] find fitting values for the final runout R_{∞} of the medium on the ground. The runout length determined by Szevc [87] is

$$R_{\infty} = \begin{cases} 0.72aR_0 + R_0 & a < 1.7 \\ 1.02a^{3/5}R_0 + R_0 & a \geq 1.7 \end{cases}, \quad (57)$$

while the experimental data indicate [49]

$$R_{\infty} = \begin{cases} 1.24aR_0 + R_0 & a < 1.7 \\ 1.6a^{1/2}R_0 + R_0 & a \geq 1.7. \end{cases} \quad (58)$$

The rheology is modelled using the Mohr-Coulomb yield strength. In order to obtain a weakly compressible material, we apply the Murnaghan EOS with $n = 7$, use a bulk modulus of $K = 10^8 \text{ Pa}$ and a shear modulus of $\mu = 10^7 \text{ Pa}$. The number of particles in the simulation is about 470 000. We find a final runout length of $R_{\infty} = 17.94 \text{ cm}$, which is larger than the experimental value of 16.32 cm, found by Lube et al. [49], a deviation of about 6%. For the same ratio a and initial radius R_0 , the simulations of Szevc [87] yield a runout length of 13.54 cm, a lower value than the experimental outcome. Figure 8 shows renderings of the initial granular column and the material at the end.

3.5. High-speed dynamics

The code was used to simulate several high-velocity impacts in the context of asteroid target fragmentation by [15]. Moreover, its performance was compared to commercial software. In this section we present exemplary simulations showing the capability of miluphcuda to handle high-speed dynamics and shock-wave physics related problems. [71] studied the experimental outcome of hypervelocity impacts of non-spherical projectiles on zinc plates by looking at specific features in the produced debris clouds. He documented changes in the debris clouds by shooting a zinc sphere, rod, and disk into 0.965 mm-thick zinc plates with a speed of about 5 km s^{-1} . The three different shapes of the projectile yield highly distinct debris clouds: The debris cloud produced by the spherical projectile features a hourglass shape, the rod forms a cone-like structure of plate material attached to the remaining intact material of the impacting rod, the disk projectile generates a pillar-shaped debris cloud with only little dispersion. We have simulated the impact with 212 000, 795 000, and 175 000 particles respectively, using the Tillotson EOS with the values as specified in table 7 in two dimensions, and a constant smoothing length of $2.5 \times$ the initial particle separation. The parameters of the three impact experiments are as follows: the diameter of the sphere is 5.76 mm and the impact speed is 4.98 km s^{-1} , the dimensions of the rod are 3.988 mm diameter and 14.148 mm length, and of the disk 13 mm are diameter and 0.795 mm thickness, with impact

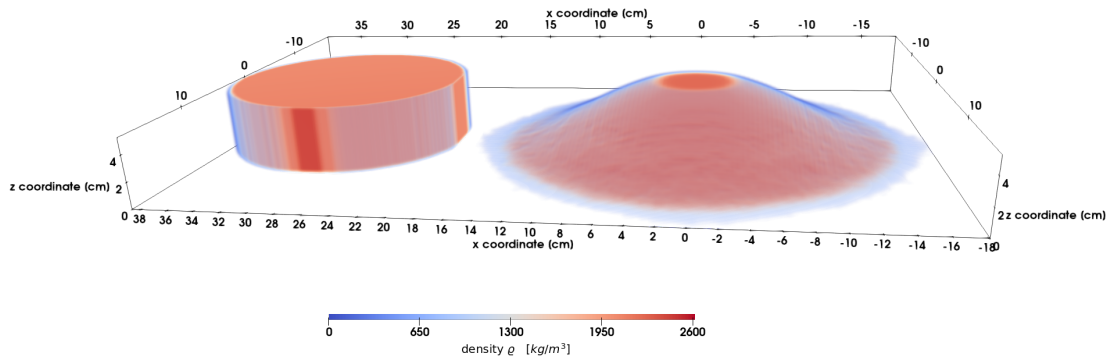


Figure 8: Gravitational collapse of a granular column. The SPH density is shown in the volume rendered image for the initial state on the left hand side and for the final state on the right hand side. The initial ratio between radius and height was $a = 0.55$.

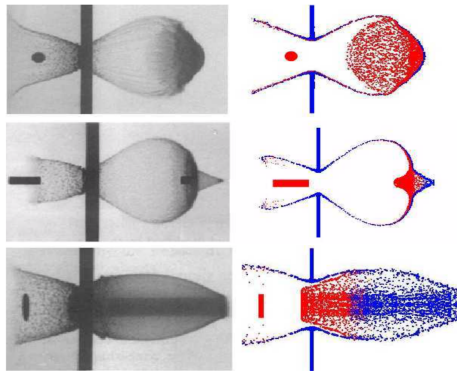


Figure 9: Debris clouds produced in high-velocity impacts of three differently shaped projectiles into zinc plates. The left panels show the radiographs as published by [71] and the right panels show the two dimensional simulation outcome using the SPH code. The projectile was (from top to bottom) a sphere, rod, disk.

speeds of 4.97 km s^{-1} and 5 km s^{-1} , respectively. The radiographs of the debris clouds produced in the experiment and the result of the SPH simulation are shown in figure 9. The simulation is capable to reproduce the resulting debris clouds accurately in shape and size.

3.6. Shocktube test problem

One standard test for a hydro code is the one dimensional shocktube test problem [see, e.g., 64]. The initial values at $t = 0$ are given by

$$\mathbf{U}(x, t = 0) = \begin{cases} \mathbf{U}_l & x \leq x_0 \\ \mathbf{U}_r & x > x_0 \end{cases}, \quad (59)$$

where $\mathbf{U}_{l,r} = (\rho_{l,r}, v_{l,r}, u_{l,r})$ denotes the constant initial values for density, velocity and internal energy left and right of x_0 . The pressure is given by the ideal gas equation

$$p = (\gamma - 1)\rho u, \quad (60)$$

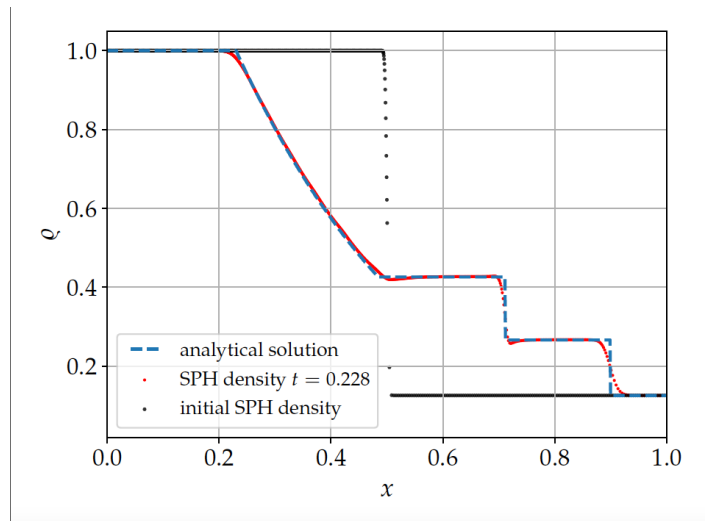


Figure 10: Shocktube problem. The initial density distribution is indicated by the black dots. The analytical solution at time $t = 0.228$ is given by the dashed blue curve. The density after this time obtained with the SPH simulation is shown by the red dots..

with $\gamma = 7/5$ in our setup. We place particles in the interval $[-1, 2]$ with $x_0 = 0.5$, and set $\mathbf{U}_l(x, t = 0) = (1, 0, 2.5)$ and $\mathbf{U}_r = (0.125, 0, 2)$. The particles have equal masses with a separation of 4×10^{-3} in the lower density region $[-1, 0.5]$ and a ρ_r/ρ_l narrower separation in the higher density region $]0.5, 2]$, leading to a total number of 3376 particles. The smoothing length is 1×10^{-2} . We apply the standard Monaghan artificial viscosity with $\alpha = 1, \beta = 2$. The initial density at $t = 0$, the density at $t = 0.0228$ and the analytical solution is shown in fig. 10. We find good agreement with the analytical solution.

3.7. Viscously spreading ring

In order to test the Navier-Stokes implementation, we simulate the two dimensional viscously spreading ring with

ϱ_0 [kg/m ³]	A_T [GPa]	B_T [GPa]	E_0 [MJ/kg]	E_{iv} [MJ/kg]	E_{cv} [MJ/kg]
7140	145	115	315	1.138	1.138
α_T	β_T	a_T	b_T	μ [GPa]	Y_M [GPa]
0.5	1.5	10	10	39	0.34

Table 7: Parameters for the Tillotson EOS which were applied for the high-velocity impact simulations. The shear modulus μ and the von Mises yield stress Y_M are also given.

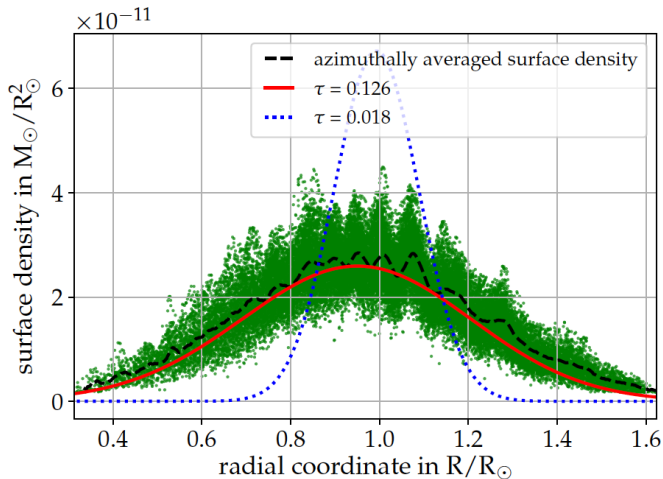


Figure 11: Radial surface density profile of the viscous dust ring after the viscous time $\tau = 0.126$. The black dashed line denotes the azimuthally averaged surface density, the green dots the density of the particles, and the solid red line the analytical solution given by eq. (62).

the parameters given in [84]. The viscously spreading ring is pressure-less and orbits a central point mass on a Keplerian orbit. With the approximation of a small kinematic viscosity coefficient ν that is independent of the surface density, an analytic solution was derived by [51]. With the initial radial profile of a ring with total mass M at $t = 0$

$$\Sigma(R) = \frac{M}{2\pi R_0} \delta(R - R_0), \quad (61)$$

the surface density evolves according to

$$\Sigma(\tau, x) = \frac{M}{\pi R_0^2} \frac{1}{\tau x^{1/4}} I_{1/4} \left(\frac{2x}{\tau} \right) \exp \left(-\frac{1+x^2}{\tau} \right), \quad (62)$$

with $x = R/R_0$, $\tau = 12\nu t/R_0^2$, and $I_{1/4}$ is the modified Bessel function to the order of $1/4$. Following [84], we simulate the viscously spreading ring with $N = 40\,000$ particles. The mass of the ring is $10^{-10} M_\odot$, the central mass is $M_c = 1 M_\odot$, and the initial radius is $R_0 = 1 R_\odot$. The kinematic viscosity coefficient is $\nu = 3 \times 10^{-8} R_\odot^2/\text{s}$. The (constant) smoothing length is set to $h = 0.0501 R_\odot$. The initial particle distribution represents the surface density given by eq. (62) at the viscous time $\tau = 0.018$. The initial velocity for each particle is given by the Keplerian velocity around the central

mass

$$v_\varphi = \sqrt{\frac{GM_c}{R}}. \quad (63)$$

Figure 11 shows the radial surface density profile of the ring after the viscous time $\tau = 0.126$. The simulation matches the analytical solution amply while slightly overestimating the surface density at the outer rim of the ring. We find also the spiral instability as described and analysed by [84]. The variation of the azimuthally averaged surface density (black dashed line) around the analytical (1D-) solution emerges from this (2D-) instability.

3.8. Circumbinary disk evolution

An arbitrary number of (point-) mass objects can be added to the simulation as described in section 2.9. We have simulated the evolution of a circumbinary disk in a two dimensional simulation. A circumbinary disk is an accretion disk orbiting a binary system that consists for example of a binary star. The numerical simulation of circumbinary disks may be quite arduous depending on the dynamical parameters of the binary system, e.g., the eccentricity [89]. The gravitational force acting from the binary stars on the gas may lead to spiral shock waves in the disk and to the formation of an inner gap around the two stars eventually. The code was applied to model the accretion disk around HD104237 using the parameters as described in [22]. The two binaries have masses of $2.2 M_\odot$ and $1.4 M_\odot$, a semi-major axis of $a = 0.22$ au and an eccentricity of $e = 0.6$. The gas density shows the spiral shock waves exerted by violent gravitational interaction with the binary stars. The detailed analysis of our simulations of circumbinary disks are beyond of the scope of this paper and will be published elsewhere (Audiffren et al., in prep.).

4. Conclusion

The numerical particle method SPH has proven to be an appropriate scheme when dealing with PDEs in the context of hydrodynamics and continuum mechanics. The GPU SPH code `miluphcuda` is now publicly available with this new release. We have presented several applications of the code from a wide range of fields, including inviscid and viscous flows, strengthless bodies and solid bodies, and self-gravitating objects. The main focus of the code lies in collisional and impact studies with different materials and

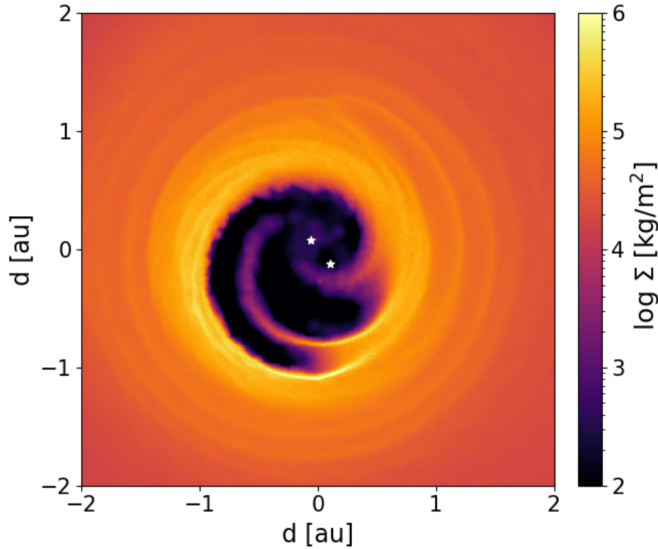


Figure 12: The surface density distribution in the circumbinary disk around HD104237 after a simulation time of 159 binary orbits on a logarithmic scale. The two white stars indicate the current position of the primary secondary.

high and low velocities, although it has been extended to handle liquid and gaseous flows from one to three dimensions, e.g., to study circumbinary disks. Another promising application has been the combination of the SPH code with the REBOUND software package to study the long term evolution of water transfer in late stage accretion. The code runs on single Nvidia GPU, which can be plugged in normal workstations running Linux or macOS with ease, and allows for speed-ups compared to a single core CPU code [78] depending on the specific problem up to 40 in pure SPH simulations and up to 80 in simulations including self-gravity. Since the new modules have only been implemented in the GPU version of our SPH code, we cannot provide speed-up values for simulations including porosity. Compared to non-porous simulations, simulations including porosity demand for much lower time step sizes to obtain convergence of the crush-curve. Since the computational effort per time step remains unchanged overall, we expect comparable speed-ups for porous simulations.

Acknowledgements

Several plots in this publication have been made by the use of the matplotlib package by [34] or with ParaView [3]. We thank the anonymous reviewers whose comments and suggestions helped to improve and clarify this manuscript. CB and TIM appreciates support by the FWF Austrian Science Fund project S 11603-N16. CMS and CB appreciate support by the DFG German Science Foundation project 398488521. CMS wants to thank Daniel Thun, Martin Jutzi and Willy Kley for helpful discussions during the course of this project.

The authors acknowledge support by the High Performance

and Cloud Computing Group at the Zentrum für Datenverarbeitung of the University of Tübingen, the state of Baden-Württemberg through bwHPC and the German Research Foundation (DFG) through grant no INST 37/935-1 FUGG.

Appendix A. The code basics and speedup

The code is written in the C programming language and uses the Nvidia CUDA application programming interface (CUDA version ≥ 6.0). The different physical modules and the dimension can be set by compile time switches. The basic tree code is based on the implementation by [14]. A description of the source and configuration files are shown in table A.8. The material configuration files are parsed using libconfig [46]. The preferred data format for the data files is HDF5. However, if the library is missing, the simulations can also run with simple ASCII table files, one SPH particle per line. A skeleton Makefile is included in the repository and has to be modified according to the local settings and GPU architecture. The code runs on Linux and macOS with a CUDA-capable GPU. The number of threads for each CUDA kernel can be set as a compile time option in `timeintegration.h`. Note, that the best settings depend on your specific hardware and physical model. There is no distinct recommendation we can provide. Usually, a reduction of the computational time can be obtained by changing slightly the number of threads for the kernel with the maximal computational time. It is advisable to tweak the number of threads for the kernels before starting production runs. All compile time options related to the physical and numerical model are set in `parameter.h`. More options like the choice of the integrator, simulation time and number of output files, are parsed on the command line on the execution. All available command line options are explained via the help option `miluphcuda -h`.

If you intend to implement additional physics to the code, the following steps are required: Add new variables to the `Particle` structure in `miluph.h` and include the corresponding memory allocation in `memory_handling.cu`. For each substep of the integrator, the central function `rhs()` is called, which subsequently calls the CUDA kernels to determine all derivatives that are required by the integrator. A skeleton CUDA kernel running over all particles in the simulation is shown in listing 1.

```

1  __global__ void skeleton_function(int *
      interactions)
2  {
3      int i, inc;
4      inc = blockDim.x * gridDim.x;
5      /* main loop over all sph particles */
6      for (i = threadIdx.x + blockIdx.x *
      blockDim.x; i < numParticles; i += inc) {
7
8          /* loop over all interaction partners
      of particle i */
9          for (j = 0; j < p.noi[i]; j++) {

```

```

10      /* index of interacting particle is
11      stored in array interactions */
12      ip = interactions[i *
13      MAX_NUM_INTERACTIONS + j];
14      // now p.rho[i] contains the
15      density of particle i and
16      // p.rho[ip] the density of its
17      interaction partner...
18
19      // insert your sph calculation here
20  } // neighbour loop end
21 } // proceed with next particle

```

Listing 1: A skeleton CUDA kernel running over all particles and their interaction partners.

The main reason to port the code to CUDA is the expected speedup compared to the CPU-only implementation. Modern SPH codes like SWIFT are designed to run on HPC architectures like clusters with distributed memory and use the Message Passing Interface (MPI) for the process communication. However, access to HPC clusters might be limited and scarce for several reasons. Moreover, long (\sim several weeks) running simulations are normally not possible due to queue regulations. Our code was especially designed to run on standard workstations with Nvidia GPUs to render high resolution SPH simulations possible without the access to special dedicated cluster hardware. Running on single GPUs only, the resolution is limited by the memory of the GPU, which is obviously much less than the distributed memory of a cluster. Hence, with current GPU hardware (12 GB memory), the maximal number of particles in a simulation with `miluphcuda` is 4×10^6 to 10^7 depending on the activated modules in the code.

The speedup for a three dimensional hydro simulation including self-gravity is presented in fig. A.13. We have compared the runtime for four different tasks: (i) neighbour search, (ii) SPH equations, (iii) self gravity, (iv) total right hand side. The last task combines (i)-(iii) and includes also the time to build the tree and calculate pressure and sound speed for all particles. Task (ii) includes the SPH equations for momentum only, since the test case was isothermal. The highest speed up is achieved in the self-gravity module, followed by the speedup in the neighbour search. These results justify our motivation to port the code to CUDA, since most of the computational time is spent in the self-gravity task for simulations including self-gravity, and in the neighbour-searching task for simulations without self-gravity.

References

- [1] Akinci, N., Ihmsen, M., Akinci, G., Solenthaler, B., Teschner, M., 2012. Versatile rigid-fluid coupling for incompressible sph. *ACM Trans. Graph.* 31, 62:1–62:8. URL: <http://doi.acm.org/10.1145/2185520.2185558>, doi:10.1145/2185520.2185558.

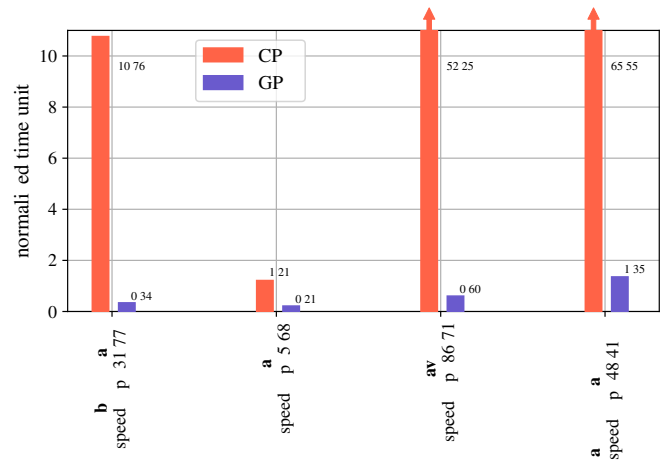


Figure A.13: Speedup obtained with the CUDA port of the code compared to the CPU-only code [78]. The CPU is an intel i7 clocked at 3.4 GHz. The GPU is a primitive (first release in 2013) standard gaming consumer graphics card Nvidia GTX Titan with a base clock of 837 MHz and 2688 CUDA cores. Shown are the normalized time units spent for different tasks.

- [2] Amicarella, A., Kocak, B., Sibilla, S., Grabe, J., 2017. A 3d smoothed particle hydrodynamics model for erosional dam-break floods. *International Journal of Computational Fluid Dynamics* 31, 413–434. URL: <https://doi.org/10.1080/10618562.2017.1422731>, doi:10.1080/10618562.2017.1422731, arXiv:<https://doi.org/10.1080/10618562.2017.1422731>.
- [3] Ayachit, U., 2015. *The ParaView Guide: A Parallel Visualization Application*. Kitware, Inc., USA.
- [4] Barnes, J., Hut, P., 1986. A hierarchical $O(N \log N)$ force-calculation algorithm. *Nature* 324, 446–449. doi:10.1038/324446a0.
- [5] Barr, A.C., 2016. Formation of exomoons: a solar system perspective. *The Astronomical Review* 12, 24–52. doi:10.1080/21672857.2017.1279469, arXiv:1701.02125.
- [6] Barr, A.C., Bruck Syal, M., 2017. Formation of massive rocky exomoons by giant impact. *Monthly Notices of the Royal Astronomical Society* 466, 4868–4874. doi:10.1093/mnras/stx078, arXiv:1701.02705.
- [7] Benz, W., 1990. Smooth Particle Hydrodynamics - a Review, in: Buchler, J.R. (Ed.), *Numerical Modelling of Nonlinear Stellar Pulsations Problems and Prospects*, p. 269.
- [8] Benz, W., Asphaug, E., 1994. Impact Simulations with Fracture. I. Method and Tests. *Icarus* 107, 98–116. doi:10.1006/icar.1994.1009.
- [9] Benz, W., Asphaug, E., 1999. Catastrophic disruptions revisited. *Icarus* 142, 5–20. doi:10.1006/icar.1999.6204, arXiv:astro-ph/9907117.
- [10] Braga-Ribas, F., Sicardy, B., Ortiz, J.L., Snodgrass, C., Roques, F., Vieira-Martins, R., Camargo, J.I.B., Assafin, M., Duffard, R., Jehin, E., Pollock, J., Leiva, R., Emilio, M., Machado, D.I., Colazo, C., Lellouch, E., Skottfelt, J., Gillon, M., Ligier, N., Maquet, L., Benedetti-Rossi, G., Gomes, A.R., Kervella, P., Monteiro, H., Sfair, R., Moutamid, M.E., Tancredi, G., Spagnotto, J., Maury, A., Morales, N., Gil-Hutton, R., Roland, S., Ceretta, A., Gu, S.H., Wang, X.B., Harpsøe, K., Rabus, M., Manfroid, J., Opitom, C., Vanzi, L., Mehret, L., Lorenzini, L., Schneider, E.M., Melia, R., Lecacheux, J., Colas, F., Vachier, F., Widemann, T., Almenares, L., Sandness, R.G., Char, F., Perez, V., Lemos, P., Martinez, N., Jørgensen, U.G., Dominik, M., Roig, F., Reichart, D.E., Lacluyze, A.P., Haislip, J.B., Ivarsen, K.M., Moore, J.P., Frank, N.R., Lambas, D.G., 2014. A ring system

Filename	Purpose
anEOS.cu, anEOS.h	functions for initializing and running ANEOS
artificial_stress.cu, artificial_stress.h	functions for artificial stress
boundary.cu, boundary.h	special treatment of boundaries (external forces, etc.)
checks.h	consistency checks of compile time options
coupled_heun_rk4_sph_nbody.cu, coupled_heun_rk4_sph_nbody.h	coupled 2nd order Heun with 4th order RK integrator
cuda_utils.h	CUDA specific functions
damage.cu, damage.h	functions for the fragmentation and damage models
density.cu, density.h	calculate density
device_tools.cu, device_tools.h	functions to print GPU information
euler.cu, euler.h	simple Euler integrator for test purposes
gravity.cu, gravity.h	functions for the calculation of self gravity and gravitational interaction of SPH particles with point masses
internal_forces.cu, inter- nal_forces.h	compute the change of stress tensor (regolith) and/or deviatoric stress tensor (all other solid materials), time evolution of density
io.cu, io.h	functions for input/output, ASCII and HDF5
kernel.cu, kernel.h	calculate SPH kernel values
linalg.cu, linalg.h	helping functions for matrix operations, etc.
little_helpers.cu, little_helpers.h	
Makefile	Makefile for GNU Make. Needs customization!
material.cfg	material configuration and parameters, see <code>material_data/</code> subdirectory.
memory_handling.cu, memory_handling.h	functions for memory allocation and copying between host and device
miluph.cu	main
miluph.h	header file with <code>Particle</code> structure definition
parameter.h	file includes all important compile time options, physical model and numerical settings
pc_values.dat	minimum absolute values, which are needed for the predictor-corrector integration schemes
plasticity.cu, plasticity.h	material models (rheology): Drucker-Prager, Collins, von Mises
porosity.cu, porosity.h	porosity models
predictor_corrector.cu, predictor_corrector.h	Predictor-Corrector integrator with predictor step $dt/2$
predictor_corrector_euler.cu, predictor_corrector_euler.h	Predictor-Corrector integrator with predictor step dt
pressure.cu, pressure.h	calculation of the pressure according to the chosen EOS; currently there is, for solids: Tillotson EOS, Murnaghan EOS, Regolith EOS (Drucker-Prager model), ANEOS; for porous solids: Jutzi EOS (Tillotson EOS with $p - \alpha$), Jutzi-Murnaghan EOS (Murnaghan EOS with $p - \alpha$); for gas: Ideal gas EOS, Polytropic gas EOS, Isothermal gas EOS
rhs.cu, rhs.h	right-hand sides, calls the kernels that compute the time derivatives
rk2adaptive.cu, rk2adaptive.h	RK2 integrator with adaptive time step
rk4_pointmass.cu, rk4_pointmass.h	RK4 integrator for gravitating pointmasses
soundspeed.cu, soundspeed.h	calculation of the soundspeed
stress.cu, stress.h	calculation of the stress tensor
timeintegration.cu, timeintegration.h	calculation of all internal forces of the solid or fluid; calculation of artificial viscosity and artificial stress
tree.cu, tree.h	functions for the Barnes-Hut tree, interaction search
velocity.cu, velocity.h	calculate velocities
viscosity.cu, viscosity.h	Navier-Stokes equation
xsph.cu, xsph.h	functions for the XSPH algorithm

Table A.8: List of files in `miluphcuda`.

- detected around the Centaur (10199) Chariklo. *Nature* 508, 72–75. doi:10.1038/nature13155.
- [11] Bui, H.H., Fukagawa, R., Sako, K., Ohno, S., 2008. Lagrangian meshfree particles method (sph) for large deformation and failure flows of geomaterial using elastic-plastic soil constitutive model. *International Journal for Numerical and Analytical Methods in Geomechanics* 32, 1537–1570. URL: <https://onlinelibrary.wiley.com/doi/abs/10.1002/nag.688>, doi:10.1002/nag.688, arXiv:<https://onlinelibrary.wiley.com/doi/pdf/10.1002/nag.688>.
- [12] Burger, C., Maindl, T.I., Schäfer, C.M., 2018. Transfer, loss and physical processing of water in hit-and-run collisions of planetary embryos. *Celestial Mechanics and Dynamical Astronomy* 130. doi:10.1007/s10569-017-9795-3, arXiv:1710.03669.
- [13] Burger, C., Schäfer, C.M., 2017. Applicability and limits of simple hydrodynamic scaling for collisions of water-rich bodies in different mass regimes. *Proceedings of the First Greek-Austrian Workshop on Extrasolar Planetary Systems*, 63–81 arXiv:1704.06075.
- [14] Burtscher, M., 2011. GPU Computing Gems Emerald Edition.
- [15] Buruchenko, S.K., Schäfer, C.M., Maindl, T.I., 2017. Smooth particle hydrodynamics gpu-acceleration tool for asteroid fragmentation simulation. *Procedia Engineering* 204, 59 – 66. URL: <http://www.sciencedirect.com/science/article/pii/S1877705817342807>, doi:<https://doi.org/10.1016/j.proeng.2017.09.726>. 14th Hypervelocity Impact Symposium 2017, HVIS2017, 24-28 April 2017, Canterbury, Kent, UK.
- [16] Butcher, J.C., 1987. *The Numerical Analysis of Ordinary Differential Equations: Runge-Kutta and General Linear Methods*. Wiley-Interscience, New York, NY, USA.
- [17] Carroll, M., Holt, A.C., 1972. Suggested Modification of the $P - \alpha$ Model for Porous Materials .
- [18] Cercos-Pita, J., 2015. Aquagpusph, a new free 3d sph solver accelerated with opencl. *Computer Physics Communications* 192, 295 – 312. URL: <http://www.sciencedirect.com/science/article/pii/S0010465515000909>, doi:<https://doi.org/10.1016/j.cpc.2015.01.026>.
- [19] Collins, G., Melosh, J., Wünnemann, K., 2011. Improvements to the epsilon-alpha compaction model for simulating impacts into high-porosity solar system objects. *International Journal of Impact Engineering - INT J IMPACT ENG* 38, 434–439. doi:10.1016/j.ijimpeng.2010.10.013.
- [20] Collins, G.S., Melosh, H.J., Ivanov, B.A., 2004. Modeling damage and deformation in impact simulations. *Meteoritics & Planetary Science* 39, 217–231. URL: <https://onlinelibrary.wiley.com/doi/abs/10.1111/j.1945-5100.2004.tb00337.x>, doi:10.1111/j.1945-5100.2004.tb00337.x, arXiv:<https://onlinelibrary.wiley.com/doi/pdf/10.1111/j.1945-5100.2004.tb00337.x>.
- [21] Crespo, A., Domínguez, J., Rogers, B., Gómez-Gesteira, M., Longshaw, S., Canelas, R., Vacondio, R., Barreiro, A., García-Feal, O., 2015. Dualsphysics: Open-source parallel cfd solver based on smoothed particle hydrodynamics (sph). *Computer Physics Communications* 187, 204 – 216. URL: <http://www.sciencedirect.com/science/article/pii/S0010465514003397>, doi:<https://doi.org/10.1016/j.cpc.2014.10.004>.
- [22] Dunhill, A.C., Cuadra, J., Dougados, C., 2015. Precession and accretion in circumbinary discs: the case of HD 104237. *MNRAS* 448, 3545–3554. doi:10.1093/mnras/stv284, arXiv:1411.0687.
- [23] Flebbe, O., Muenzel, S., Herold, H., Riffert, H., Ruder, H., 1994. Smoothed Particle Hydrodynamics: Physical Viscosity and the Simulation of Accretion Disks. *ApJ* 431, 754. doi:10.1086/174526.
- [24] Genda, H., Iizuka, T., Sasaki, T., Ueno, Y., Ikoma, M., 2017. Ejection of iron-bearing giant-impact fragments and the dynamical and geochemical influence of the fragment re-accretion. *Earth and Planetary Science Letters* 470, 87–95. doi:10.1016/j.epsl.2017.04.035, arXiv:1704.05251.
- [25] Genda, H., Kokubo, E., Ida, S., 2011. Giant Impacts and Terrestrial Planet Formation, in: *Lunar and Planetary Science Conference*, p. 2090.
- [26] Geretschauser, R.J., Speith, R., Güttler, C., Krause, M., Blum, J., 2010. Numerical simulations of highly porous dust aggregates in the low-velocity collision regime*. *Astronomy and Astrophysics* 513.
- [27] Gingold, R.A., Monaghan, J.J., 1977. Smoothed particle hydrodynamics: theory and application to non-spherical stars. *MNRAS* 181, 375–389. doi:10.1093/mnras/181.3.375.
- [28] Grishin, E., Malamud, U., Perets, H.B., Wand el, O., Schäfer, C.M., 2020. The wide-binary origin of (2014) MU₆₉-like Kuiper belt contact binaries. *Nature* 580, 463–466. doi:10.1038/s41586-020-2194-z.
- [29] Güttler, C., Krause, M., Geretschauser, R.J., Speith, R., Blum, J., 2009. The Physics of Protoplanetary Dust Agglomerates. IV. Toward a Dynamical Collision Model. *ApJ* 701, 130–141. doi:10.1088/0004-637X/701/1/130, arXiv:0906.0088.
- [30] Haghhighipour, N., Maindl, T.I., Schäfer, C., Speith, R., Dvorak, R., 2016. Triggering sublimation-driven activity of main belt comets. *The Astrophysical Journal* 830, 22. doi:10.3847/0004-637X/830/1/22, arXiv:1606.06226.
- [31] Haghhighipour, N., Maindl, T.I., Schäfer, C.M., Wandel, O.J., 2018. Triggering the activation of main-belt comets: The effect of porosity. *The Astrophysical Journal* 855, 60. doi:10.3847/1538-4357/aaa7f3, arXiv:1801.08247.
- [32] Hernquist, L., Katz, N., 1989. TREESPH - A unification of SPH with the hierarchical tree method. *ApJS* 70, 419–446. doi:10.1086/191344.
- [33] Herrmann, W., 1969. Constitutive Equation for the Dynamic Compaction of Ductile Porous Materials. *Journal of Applied Physics* 40.
- [34] Hunter, J.D., 2007. Matplotlib: A 2d graphics environment. *Computing In Science & Engineering* 9, 90–95.
- [35] Hérault, A., Bilotta, G., Dalrymple, R.A., 2010. Sph on gpu with cuda. *Journal of Hydraulic Research* 48, 74–79. doi:10.1080/00221686.2010.9641247.
- [36] Ihmsen, M., Orthmann, J., Solenthaler, B., Kolb, A., Teschner, M., 2014. SPH Fluids in Computer Graphics, in: Lefebvre, S., Spagnuolo, M. (Eds.), *Eurographics 2014 - State of the Art Reports*, The Eurographics Association. doi:10.2312/egst.20141034.
- [37] Jutzi, M., 2015. Sph calculations of asteroid disruptions: The role of pressure dependent failure models. *Planetary and Space Science* 107, 3 – 9. URL: <http://www.sciencedirect.com/science/article/pii/S0032063314002931>, doi:<https://doi.org/10.1016/j.pss.2014.09.012>. vIII Workshop on Catastrophic Disruption in the Solar System.
- [38] Jutzi, M., Michel, P., Hiraoka, K., Nakamura, A.M., Benz, W., 2009. Numerical simulations of impacts involving porous bodies: II. Comparison with laboratory experiments. *Icarus* 201.
- [39] Kegerreis, J.A., Eke, V.R., Gonnet, P., Korycansky, D.G., Massey, R.J., Schaller, M., Teodoro, L.F.A., 2019. Planetary giant impacts: convergence of high-resolution simulations using efficient spherical initial conditions and SWIFT. *MNRAS* 487, 5029–5040. doi:10.1093/mnras/stz1606, arXiv:1901.09934.
- [40] Kipping, D.M., Bakos, G.Á., Buchhave, L., Nesvorný, D., Schmitt, A., 2012. The hunt for exomoons with kepler (hek). i. description of a new observational project. *The Astrophysical Journal* 750, 115. doi:10.1088/0004-637X/750/2/115, arXiv:1201.0752.
- [41] Korzani, M.G., Galindo-Torres, S.A., Scheuermann, A., Williams, D.J., 2017. Parametric study on smoothed particle hydrodynamics for accurate determination of drag coefficient for a circular cylinder. *Water Science and Engineering* 10, 143 – 153. URL: <http://www.sciencedirect.com/science/article/pii/S167423701730056X>, doi:<https://doi.org/10.1016/j.wse.2017.06.001>.
- [42] Lange, M.A., Ahrens, T.J., Boslough, M.B., 1984. Impact cratering and spall failure of gabbro. *Icarus* 58, 383–395. doi:10.1016/0019-1035(84)90084-8.
- [43] Leinhardt, Z.M., Dobinson, J., Carter, P.J., Lines, S., 2015. Numerically Predicted Indirect Signatures of Terrestrial Planet

- Formation. *ApJ* 806, 23. doi:[10.1088/0004-637X/806/1/23](https://doi.org/10.1088/0004-637X/806/1/23), [arXiv:1506.05233](https://arxiv.org/abs/1506.05233).
- [44] Leinhardt, Z.M., Stewart, S.T., 2012. Collisions between Gravity-dominated Bodies. I. Outcome Regimes and Scaling Laws. *ApJ* 745, 79. doi:[10.1088/0004-637X/745/1/79](https://doi.org/10.1088/0004-637X/745/1/79), [arXiv:1106.6084](https://arxiv.org/abs/1106.6084).
- [45] Libersky, L.D., Petschek, A.G., 1991. Smooth particle hydrodynamics with strength of materials, in: Trease, H.E., Fritts, M.F., Crowley, W.P. (Eds.), *Advances in the Free-Lagrange Method Including Contributions on Adaptive Gridding and the Smooth Particle Hydrodynamics Method*, pp. 248–257. doi:[10.1007/3-540-54960-9_58](https://doi.org/10.1007/3-540-54960-9_58).
- [46] Lindner, M., 2015. `libconfig@ONLINE`. URL: <http://www.hyperrealm.com/libconfig>.
- [47] Liu, M.B., Liu, G.R., 2010. Smoothed particle hydrodynamics (sph): an overview and recent developments. *Archives of Computational Methods in Engineering* 17, 25–76. URL: <https://doi.org/10.1007/s11831-010-9040-7>, doi:[10.1007/s11831-010-9040-7](https://doi.org/10.1007/s11831-010-9040-7).
- [48] Liu, S.F., Hori, Y., Lin, D.N.C., Asphaug, E., 2015. Giant impact: An efficient mechanism for the devolatilization of super-earths. *The Astrophysical Journal* 812, 164. doi:[10.1088/0004-637X/812/2/164](https://doi.org/10.1088/0004-637X/812/2/164), [arXiv:1509.05772](https://arxiv.org/abs/1509.05772).
- [49] Lube, G., Huppert, H.E., Sparks, R.S.J., Hallworth, M.A., 2004. Axisymmetric collapses of granular columns. *Journal of Fluid Mechanics* 508, 175–199. doi:[10.1017/S0022112004009036](https://doi.org/10.1017/S0022112004009036).
- [50] Lucy, L.B., 1977. A numerical approach to the testing of the fission hypothesis. *Astron. Journal* 82, 1013–1024. doi:[10.1086/112164](https://doi.org/10.1086/112164).
- [51] Lynden-Bell, D., Pringle, J.E., 1974. The evolution of viscous discs and the origin of the nebular variables. *MNRAS* 168, 603–637. doi:[10.1093/mnras/168.3.603](https://doi.org/10.1093/mnras/168.3.603).
- [52] Malamud, U., Perets, H.B., Schäfer, C., Burger, C., 2018. Moonfalls: collisions between the Earth and its past moons. *MNRAS* 479, 1711–1721. doi:[10.1093/mnras/sty1667](https://doi.org/10.1093/mnras/sty1667), [arXiv:1805.00019](https://arxiv.org/abs/1805.00019).
- [53] Malamud, U., Perets, H.B., Schäfer, C., Burger, C., 2020. Collisional formation of massive exomoons of superterrestrial exoplanets. *MNRAS* 492, 5089–5101. doi:[10.1093/mnras/staa211](https://doi.org/10.1093/mnras/staa211), [arXiv:1904.12854](https://arxiv.org/abs/1904.12854).
- [54] Marcus, R.A., Sasselov, D., Hernquist, L., Stewart, S.T., 2010a. Minimum radii of super-earths: Constraints from giant impacts. *The Astrophysical Journal Letters* 712, L73–L76. doi:[10.1088/2041-8205/712/1/L73](https://doi.org/10.1088/2041-8205/712/1/L73), [arXiv:1003.0451](https://arxiv.org/abs/1003.0451).
- [55] Marcus, R.A., Sasselov, D., Stewart, S.T., Hernquist, L., 2010b. Water/icy super-earths: Giant impacts and maximum water content. *The Astrophysical Journal Letters* 719, L45–L49. doi:[10.1088/2041-8205/719/1/L45](https://doi.org/10.1088/2041-8205/719/1/L45), [arXiv:1007.3212](https://arxiv.org/abs/1007.3212).
- [56] McInnes, L., Healy, J., Melville, J., 2018a. UMAP: Uniform Manifold Approximation and Projection for Dimension Reduction. *ArXiv e-prints* [arXiv:1802.03426](https://arxiv.org/abs/1802.03426).
- [57] McInnes, L., Healy, J., Saul, N., Grossberger, L., 2018b. Umap: Uniform manifold approximation and projection. *The Journal of Open Source Software* 3, 861.
- [58] Melosh, H., 1996. *Impact Cratering: A Geologic Process*. Oxford monographs on geology and geophysics, Oxford University Press.
- [59] Melosh, H.J., 1989. Impact cratering: A geologic process.
- [60] Melosh, H.J., 2007. A hydrocode equation of state for SiO_2 . *Meteoritics & Planetary Science* 42, 2079–2098. URL: <https://onlinelibrary.wiley.com/doi/abs/10.1111/j.1945-5100.2007.tb01009.x>, doi:[10.1111/j.1945-5100.2007.tb01009.x](https://doi.org/10.1111/j.1945-5100.2007.tb01009.x), [arXiv:https://onlinelibrary.wiley.com/doi/pdf/10.1111/j.1945-5100.2007.tb01009.x](https://arxiv.org/abs/https://onlinelibrary.wiley.com/doi/pdf/10.1111/j.1945-5100.2007.tb01009.x).
- [61] Melosh, H.J., 2007. A hydrocode equation of state for SiO_2 . *Meteoritics and Planetary Science* 42, 2079–2098. doi:[10.1111/j.1945-5100.2007.tb01009.x](https://doi.org/10.1111/j.1945-5100.2007.tb01009.x).
- [62] Mocz, P., Succi, S., 2015. Numerical solution of the nonlinear Schrödinger equation using smoothed-particle hydrodynamics. *Phys. Rev. E* 91, 053304. doi:[10.1103/PhysRevE.91.053304](https://doi.org/10.1103/PhysRevE.91.053304), [arXiv:1503.03869](https://arxiv.org/abs/1503.03869).
- [63] Monaghan, J., 2012. Smoothed particle hydrodynamics and its diverse applications. *Annual Review of Fluid Mechanics* 44, 323–346. URL: <https://doi.org/10.1146/annurev-fluid-120710-101220>, doi:[10.1146/annurev-fluid-120710-101220](https://doi.org/10.1146/annurev-fluid-120710-101220), [arXiv:https://doi.org/10.1146/annurev-fluid-120710-101220](https://arxiv.org/abs/https://doi.org/10.1146/annurev-fluid-120710-101220).
- [64] Monaghan, J., Gingold, R., 1983. Shock simulation by the particle method sph. *Journal of Computational Physics* 52, 374 – 389. URL: <http://www.sciencedirect.com/science/article/pii/0021999183900360>, doi:[https://doi.org/10.1016/0021-9991\(83\)90036-0](https://doi.org/10.1016/0021-9991(83)90036-0).
- [65] Monaghan, J.J., 1992. Smoothed particle hydrodynamics. *ARA&A* 30, 543–574. doi:[10.1146/annurev-aa.30.090192.002551](https://doi.org/10.1146/annurev-aa.30.090192.002551).
- [66] Monaghan, J.J., 2005. Smoothed particle hydrodynamics. *Reports on Progress in Physics* 68, 1703–1759. URL: <https://doi.org/10.1088/2F0034-4885/2F68/2F8/2F01>, doi:[10.1088/0034-4885/68/8/r01](https://doi.org/10.1088/0034-4885/68/8/r01).
- [67] Murnaghan, F.D., 1937. Finite deformations of an elastic solid. *American Journal of Mathematics* 59, 235–260. URL: <http://www.jstor.org/stable/2371405>.
- [68] Nakamura, A.M., Michel, P., Setoh, M., 2007. Weibull parameters of Yakuno basalt targets used in documented high-velocity impact experiments. *Journal of Geophysical Research (Planets)* 112, E02001. doi:[10.1029/2006JE002757](https://doi.org/10.1029/2006JE002757).
- [69] Ortiz, J.L., Santos-Sanz, P., Sicardy, B., Benedetti-Rossi, G., Bérard, D., Morales, N., Duffard, R., Braga-Ribas, F., Hopp, U., Ries, C., Nascimbeni, V., Marzari, F., Granata, V., Pál, A., Kiss, C., Pribulla, T., Komžík, R., Hornoch, K., Pravec, P., Bacci, P., Maestriperi, M., Nerli, L., Mazzei, L., Bachini, M., Martinelli, F., Succi, G., Ciabattari, F., Mikuz, H., Carbognani, A., Gaehrken, B., Mottola, S., Hellmich, S., Rommel, F.L., Fernández-Valenzuela, E., Bagatin, A.C., Cikota, S., Cikota, A., Lecacheux, J., Vieira-Martins, R., Camargo, J.I.B., Assafin, M., Colas, F., Behrend, R., Desmars, J., Meza, E., Alvarez-Candal, A., Beisker, W., Gomes-Junior, A.R., Morgado, B.E., Roques, F., Vachier, F., Berthier, J., Mueller, T.G., Madiedo, J.M., Unsalan, O., Sonbas, E., Karaman, N., Erece, O., Koseoglu, D.T., Ozisik, T., Kalkan, S., Guney, Y., Nisaei, M.S., Satir, O., Yesilyaprak, C., Puskullu, C., Kabas, A., Demircan, O., Alikakos, J., Charmandaris, V., Leto, G., Ohlert, J., Christille, J.M., Szakáts, R., Farkas, A.T., Varga-Verebélyi, E., Marton, G., Marciniak, A., Bartczak, P., Santana-Ros, T., Butkiewicz-Bak, M., Dudziński, G., Alí-Lagoa, V., Gazeas, K., Tzouganatos, L., Paschalis, N., Tsamis, V., Sánchez-Lavega, A., Pérez-Hoyos, S., Hueso, R., Guirado, J.C., Peris, V., Iglesias-Marzoa, R., 2017. The size, shape, density and ring of the dwarf planet haumea from a stellar occultation. *Nature* 550, 219–223. doi:[10.1038/nature24051](https://doi.org/10.1038/nature24051).
- [70] Owen, J.M., 2001. An open-source project for modeling hydrodynamics in astrophysical systems. *Computing in Science Engineering* 3, 54–59. doi:[10.1109/5992.963428](https://doi.org/10.1109/5992.963428).
- [71] Piekutowski, A.J., 2001. Debris clouds produced by the hypervelocity impact of nonspherical projectiles. *International Journal of Impact Engineering* 26, 613 – 624. URL: <http://www.sciencedirect.com/science/article/pii/S0734743X01001221>, doi:[https://doi.org/10.1016/S0734-743X\(01\)00122-1](https://doi.org/10.1016/S0734-743X(01)00122-1).
- [72] Price, D.J., 2012. Smoothed particle hydrodynamics and magnetohydrodynamics. *Journal of Computational Physics* 231, 759–794. doi:[10.1016/j.jcp.2010.12.011](https://doi.org/10.1016/j.jcp.2010.12.011), [arXiv:1012.1885](https://arxiv.org/abs/1012.1885).
- [73] Price, D.J., Wurster, J., Nixon, C., Tricco, T.S., Toupin, S., Pettitt, A., Chan, C., Laibe, G., Glover, S., Dobbs, C., Nealon, R., Dittmann, D., Worpel, H., Bonnerot, C., Dipierro, G., Ragusa, E., Federrath, C., Iaconi, R., Reichardt, T., Forgan, D., Hutchison, M., Constantino, T., Ayliffe, B., Mentiplay, D., Hirsh, K., Lodato, G., 2017. PHANTOM: Smoothed particle hydrodynamics and magnetohydrodynamics code. *Astrophysics Source Code Library*. [arXiv:1709.002](https://arxiv.org/abs/1709.002).
- [74] Prabhu Ramachandran, 2016. PySPH: a reproducible and high-performance framework for smoothed particle hydrodynamics, in: Sebastian Benthall, Scott Rostrup (Eds.), *Proceedings of*

- the 15th Python in Science Conference, pp. 122 – 129. doi:[10.25080/Majora-629e541a-011](https://doi.org/10.25080/Majora-629e541a-011).
- [75] Rein, H., Liu, S.F., 2012. REBOUND: an open-source multi-purpose N-body code for collisional dynamics. *A&A* 537, A128. doi:[10.1051/0004-6361/201118085](https://doi.org/10.1051/0004-6361/201118085), [arXiv:1110.4876](https://arxiv.org/abs/1110.4876).
- [76] Rein, H., Spiegel, D.S., 2015. IAS15: a fast, adaptive, high-order integrator for gravitational dynamics, accurate to machine precision over a billion orbits. *journal name* 446, 1424–1437. doi:[10.1093/mnras/stu2164](https://doi.org/10.1093/mnras/stu2164), [arXiv:1409.4779](https://arxiv.org/abs/1409.4779).
- [77] Rosswog, S., 2015. Sph methods in the modelling of compact objects. *Living Reviews in Computational Astrophysics* 1, 1. URL: <https://doi.org/10.1007/lrca-2015-1>, doi:[10.1007/lrca-2015-1](https://doi.org/10.1007/lrca-2015-1).
- [78] Schäfer, C., Riecker, S., Maindl, T.I., Speith, R., Scherrer, S., Kley, W., 2016. A smooth particle hydrodynamics code to model collisions between solid, self-gravitating objects. *Astronomy & Astrophysics* 590, A19. doi:[10.1051/0004-6361/201528060](https://doi.org/10.1051/0004-6361/201528060), [arXiv:1604.03290](https://arxiv.org/abs/1604.03290).
- [79] Schäfer, C., Speith, R., Hipp, M., Kley, W., 2004. Simulations of planet-disc interactions using Smoothed Particle Hydrodynamics. *A&A* 418, 325–335. doi:[10.1051/0004-6361:20034034](https://doi.org/10.1051/0004-6361:20034034), [arXiv:astro-ph/0401425](https://arxiv.org/abs/astro-ph/0401425).
- [80] Schäfer, C., Speith, R., Kley, W., 2007. Collisions between equal-sized ice grain agglomerates. *A&A* 470, 733–739. doi:[10.1051/0004-6361:20077354](https://doi.org/10.1051/0004-6361:20077354), [arXiv:0705.2672](https://arxiv.org/abs/0705.2672).
- [81] Schäfer, C.M., Scherrer, S., Buchwald, R., Maindl, T.I., Speith, R., Kley, W., 2017. Numerical simulations of regolith sampling processes. *Planetary and Space Science* 141, 35–44. doi:[10.1016/j.pss.2017.04.015](https://doi.org/10.1016/j.pss.2017.04.015), [arXiv:1705.00893](https://arxiv.org/abs/1705.00893).
- [82] Schaller, M., Gonnet, P., Chalk, A.B.G., Draper, P.W., 2018. SWIFT: SPH With Inter-dependent Fine-grained Tasking. [arXiv:1805.020](https://arxiv.org/abs/1805.020).
- [83] Sirono, S.i., 2004. Conditions for collisional growth of a grain aggregate. *Icarus* 167.
- [84] Speith, R., Kley, W., 2003. Stability of the viscously spreading ring. *A&A* 399, 395–407. doi:[10.1051/0004-6361:20021783](https://doi.org/10.1051/0004-6361:20021783), [arXiv:astro-ph/0212139](https://arxiv.org/abs/astro-ph/0212139).
- [85] Springel, V., 2000. GADGET-2: A Code for Cosmological Simulations of Structure Formation. *Astrophysics Source Code Library*. [arXiv:0003.001](https://arxiv.org/abs/0003.001).
- [86] Stellingwerf, R.F., Wingate, C.A., 1994. Impact Modelling with SPH (Invited paper). *Memorie della Società Astronomia Italiana* 65, 1117.
- [87] Szevec, K., 2016. Smoothed particle hydrodynamics modeling of granular column collapse. *Granular Matter* 19, 3. URL: <https://doi.org/10.1007/s10035-016-0684-3>, doi:[10.1007/s10035-016-0684-3](https://doi.org/10.1007/s10035-016-0684-3).
- [88] Thun, D., Kley, W., 2018. Migration of planets in circumbinary discs. *A&A* 616, A47. doi:[10.1051/0004-6361/201832804](https://doi.org/10.1051/0004-6361/201832804), [arXiv:1806.00314](https://arxiv.org/abs/1806.00314).
- [89] Thun, D., Kley, W., Picogna, G., 2017. Circumbinary discs: Numerical and physical behaviour. *A&A* 604, A102. doi:[10.1051/0004-6361/201730666](https://doi.org/10.1051/0004-6361/201730666), [arXiv:1704.08130](https://arxiv.org/abs/1704.08130).
- [90] Tillotson, J.H., 1962. *Metallic Equations of State for Hypervelocity Impact*. Technical Report General Atomic Report GA-3216. General Dynamics. San Diego, CA.
- [91] von Mises, R., 1913. *Mechanik der festen Körper im plastisch deformablen Zustand*. *Göttin. Nachr. Math. Phys.* 1, 582–592.
- [92] Wadsley, J.W., Keller, B.W., Quinn, T.R., 2017. Gasoline2: a modern smoothed particle hydrodynamics code. *Monthly Notices of the Royal Astronomical Society* 471, 2357–2369. URL: <https://doi.org/10.1093/mnras/stx1643>, doi:[10.1093/mnras/stx1643](https://doi.org/10.1093/mnras/stx1643), [arXiv:http://oup.prod.sis.lan/mnras/article-pdf/471/2/2357/19491158/stx1643.pdf](https://oup.prod.sis.lan/mnras/article-pdf/471/2/2357/19491158/stx1643.pdf).
- [93] Wandel, O.J., Schäfer, C.M., Maindl, T.I., 2017. Collisional fragmentation of porous objects in planetary systems. *Proceedings of the First Greek-Austrian Workshop on Extrasolar Planetary Systems*, 225–242.
- [94] Yu, M., Huang, Y., Deng, W., Cheng, H., 2018. Forecasting landslide mobility using an sph model and ring shear strength tests: a case study. *Natural Hazards and Earth System Sciences* 18, 3343–3353. URL: <https://www.nat-hazards-earth-syst-sci.net/18/3343/2018/>, doi:[10.5194/nhess-18-3343-2018](https://doi.org/10.5194/nhess-18-3343-2018).
- [95] Zander, C., Hopp-Hirschler, M., Nicken, U., 2018. Mesoscopic simulation and characterization of the morphological evolution in phase separating fluid mixtures. *Computational Materials Science* 149, 267 – 281. URL: <http://www.sciencedirect.com/science/article/pii/S0927025618301721>, doi:<https://doi.org/10.1016/j.commatsci.2018.03.019>.

Conclusion & Outlook

Throughout the composition of this thesis we encountered many challenges and learned a variety of new things. One of the biggest challenges was the incorporation of a well-functioning timestep regulation, which is necessary due to the iterative nature of the P - α scheme. The pressure P and the distention α depend on each other, therefore a small timestep is required in order to get the correct pair of values. If they deviate from the crush-curve during the compaction phase, the desired behaviour of the porous crushing cannot be guaranteed anymore. For that purpose, we implemented a timestep checking function for our time integrators. This function compares the changes regarding the distention and pressure, and in case they are too large, reduces the timestep and recalculates the last step. It is tuned in such a way that the timestep size is optimally calculated in order not to waste valuable simulation time but still ensure the resolution of the crush-curve. Hence, we make sure that our porosity model is always accurate and the calculations are as fast as possible.

Another challenge is the large parameter space for the different simulation scenarios. The collision speed can vary between some cm/s up to several km/s, which means that they vary from sub- to supersonic, as well as from almost isothermal to strongly dissipative collisions. A smaller, not really well-studied parameter is the sound speed c_s . In the matrix material it is somewhat well-known and a simple approximation is $c_s = \sqrt{K/\rho}$ using the bulk modulus K . However, for porous materials this is not as simple as before. Measurements suggest values down to some tens of m/s, while the sound speed in solid matrix material is of the order of some km/s. In the end, we settled on using a mixture between a) a linear function interpolating between the porous sound speed $c_{s,\text{por}}$ and the solid sound speed $c_{s,\text{solid}}$ with decreasing distention ranging from α_0 to $\alpha = 1$ and b) a variable sound speed calculated for the Tillotson EOS by Reinhardt & Stadel (2017).

Our research provided the following new information regarding porous small bodies in our Solar System:

- Impacts of small bodies are a reasonable mechanism for exposing sub-surface volatiles, thus triggering the sublimation-driven activity of MBCs. The water content of MBCs has to be larger than traditionally suggested and the water-ice must be buried within the top 15 m.
- We limited the parameter space for the impact on Phobos that created the crater Stickney.

We got more insight regarding the most probable scenario needed to create this large crater, which is consistent with other researchers' results.

- It is possible to explain and form contact binaries through the merger of two objects that have a wide initial separation. The binary orbit can be perturbed in a collisional environment. As a result, even binaries with originally low inclinations can get excited to higher inclinations and, thus, be subjected to semi-secular Lidov-Kozai evolution leading to the formation of contact binaries. We demonstrate the feasibility of this evolution in case of the KBO Arrokoth which likely is not unique. It could be a natural by-product of the evolution of KBOs in the early Solar System and the formation pathway suggested for KBO binaries.

However, this is not the end but rather just another step in investigating the different influences of porosity, improving the models and code as well as finding possible formation channels to understand why and how our Solar System evolved the way it did. There are still a lot of aspects with room for improvement.

Regarding an outlook towards future studies, the most important thing which was already implemented but not improved yet in this thesis is the equation of state. Most of our simulations were performed with the Tillotson EOS which lacks a consistent treatment of phase transitions. For low velocity simulations this is fine, however for high speed impact simulations with large amounts of energy being deposited in the material, this can be problematic. A sophisticated thermodynamical description is important to realistically model temperatures and phases of the material. Therefore, we included the P - α porosity model into ANEOS due to this equation of state being an analytic one based on calculating the Helmholtz free energy from first principles. This yields a more realistic description of the thermodynamical aspects and will thoroughly be tested and used in the near future.

Further important things which have room for improvement are:

- The understanding of material properties like tensile strength, crush behaviour, and bulk parameters. There have not yet been enough measurements and experiments for a satisfying understanding of how porous materials behave exactly, under which pressure they start to deform, and so forth.
- The research for an EOS which can be used for a mixture of materials like ice and basalt, which is present in many of the small bodies.
- Narrowing down the parameter space regarding EOS parameters for porous materials.
- Further optimization of the SPH scheme to increase the spatial resolution (using more particles).

To conclude, a variety of findings were thoroughly elaborated and explained in this thesis. With the above mentioned improvements coming in the next years, we hope that the formation processes of our Solar System will be even better understood, shedding light on the darkest corners.

List of Figures

1.1	Small bodies in the inner Solar System	7
1.2	Small bodies in the outer Solar System	8
1.3	Density of different small bodies	9
1.4	Macroporosity of different small bodies	10
1.5	Tempel 1	12
1.6	Itokawa	13
1.7	Chury	13
1.8	Arrokoth	14
1.9	Chariklo	15
2.1	Macroporosity on Itokawa	19
2.2	Porosity in perlite and sand	20

Bibliography

- Abe, S., Mukai, T., Barnouin, O., Cheng, A., Hirata, N. et al. *Density, porosity and internal structure of asteroid Itokawa by the Hayabusa mission. -1*, 493 (2006).
- Benz, W. and Asphaug, E. *Impact Simulations with Fracture. I. Method and Tests*. Icarus, 107 (1994).
- Benz, W. and Asphaug, E. *Simulations of brittle solids using smooth particle hydrodynamics*. Computer Physics Communications, 87 (1995).
- Bottke, W. F., Nolan, M. C., Greenberg, R. and Kolvoord, R. A. *Velocity Distributions among Colliding Asteroids*. Icarus, 107(2), 255 – 268 (1994).
- Braga-Ribas, F., Sicardy, B., Ortiz, J. L., Snodgrass, C., Roques, F. et al. *A ring system detected around the Centaur (10199) Chariklo*. Nature, 508(7494), 72–75 (2014).
- Britt, D. T., Yeomans, D., Housen, K. and Consolmagno, G. *Asteroid Density, Porosity, and Structure*. Asteroids III (2002).
- Bui, H. H., Fukagawa, R., Sako, K. and Ohno, S. *Lagrangian meshfree particles method (SPH) for large deformation and failure flows of geomaterial using elastic-plastic soil constitutive model*. International Journal for Numerical and Analytical Methods in Geomechanics, 32(12), 1537–1570 (2008).
- Carry, B. *Density of asteroids*. Planetary and Space Science, 73(1), 98–118 (2012).
- Chapman, C. R., Davis, D. R. and Greenberg, R. *Asteroid fragmentation processes and collisional evolution..* NASA Technical Memo, 3511, 72–73 (1977).
- Collins, G., Melosh, H. and Wünnemann, K. *Improvements to the $\epsilon - \alpha$ porous compaction model for simulating impacts into high-porosity solar system objects*. International Journal of Impact Engineering, 38 (2011).
- DeMeo, F. E., Binzel, R. P., Slivan, S. M. and Bus, S. J. *An extension of the Bus asteroid taxonomy into the near-infrared*. Icarus, 202(1), 160 – 180 (2009).
- Geretshauser, R. J., Speith, R., Güttler, C., Krause, M. and Blum, J. *Numerical simulations of highly porous dust aggregates in the low-velocity collision regime**. Astronomy and Astrophysics, 513 (2010).

- Gingold, R. A. and Monaghan, J. J. *Smoothed particle hydrodynamics - Theory and application to non-spherical stars* (1977).
- Grady, D. and Kipp, M. *Continuum modelling of explosive fracture in oil shale*. International Journal of Rock Mechanics and Mining Sciences & Geomechanics Abstracts, 17 (1980).
- Greenberg, J. M. *Predicting that comet Halley is dark*. Nature, 321(6068), 385 (1986).
- Grishin, E., Malamud, U., Perets, H. B., Wandel, O. and Schäfer, C. M. *The wide-binary origin of (2014) MU69-like Kuiper belt contact binaries*. Nature, 580(7804), 463–466 (2020).
- Haghighipour, N., Maindl, T. I., Schäfer, C. M. and Wandel, O. J. *Triggering the Activation of Main-belt Comets: The Effect of Porosity*. The Astrophysical Journal, 855(1), 60 (2018).
- Herrmann, W. *Constitutive Equation for the Dynamic Compaction of Ductile Porous Materials*. Journal of Applied Physics, 40 (1969).
- Horner, J., Evans, N. W. and Bailey, M. E. *Simulations of the population of Centaurs - I. The bulk statistics*. Monthly Notices of the Royal Astronomical Society, 354(3), 798–810 (2004).
- Housen, K. and Holsapple, K. *Impact cratering on porous asteroids*. Icarus, 163, 102–119 (2003).
- Housen, K., Sweet, W. and Holsapple, K. *Impacts into Porous Asteroids*. Icarus, 300 (2017).
- Housen, K. R. and Holsapple, K. A. *Scale Effects in Strength-Dominated Collisions of Rocky Asteroids*. Icarus, 142(1), 21 – 33 (1999).
- Jutzi, M., Benz, W. and Michel, P. *Numerical simulations of impacts involving porous bodies: I. Implementing sub-resolution porosity in a 3D SPH hydrocode*. Icarus, 198 (2008).
- Küppers, M., O'Rourke, L., Bockelée-Morvan, D., Zakharov, V., Lee, S. et al. *Localized sources of water vapour on the dwarf planet (1)Ceres*. Nature, 505(7484), 525–527 (2014).
- Laguna, P. *Smoothed particle interpolation*. The Astrophysical Journal, 439 (1995).
- Libersky, L. D. and Petschek, A. G. (1991). *Smooth particle hydrodynamics with strength of materials*. In H. E. Trease, M. F. Fritts, & W. P. Crowley (Eds.) *Advances in the Free-Lagrange Method Including Contributions on Adaptive Gridding and the Smooth Particle Hydrodynamics Method*, (pp. 248–257). Berlin, Heidelberg: Springer Berlin Heidelberg.
- Lucy, L. B. *A numerical approach to the testing of the fission hypothesis* (1977).
- Michikami, T., Moriguchi, K., Hasegawa, S. and Fujiwara, A. *Ejecta velocity distribution for impact cratering experiments on porous and low strength targets*. Planetary and Space Science, 55(1), 70 – 88 (2007).
- Miyamoto, H., Yano, H., Scheeres, D., Abe, S., Barnouin, O. et al. *Regolith Migration and Sorting on Asteroid Itokawa*. Science, 316, 1011–1014 (2007).

- Park, R. S., Konopliv, A. S., Bills, B. G., Rambaux, N., Castillo-Rogez, J. C. et al. *A partially differentiated interior for (1) Ceres deduced from its gravity field and shape*. *Nature*, 537(7621), 515–517 (2016).
- Price, D. J. *Smoothed particle hydrodynamics and magnetohydrodynamics*. *Journal of Computational Physics*, 231(3), 759–794 (2012).
- Pätzold, M., Andert, T., Hahn, M., Asmar, S., Barriot, J.-P. et al. *A homogeneous nucleus for comet 67P/Churyumov–Gerasimenko from its gravity field*. *Nature*, 530, 63–65 (2016).
- Randles, P. and Libersky, L. *Smoothed Particle Hydrodynamics: Some recent improvements and applications*. *Computer Methods in Applied Mechanics and Engineering*, 139 (1996).
- Reinhardt, C. and Stadel, J. *Numerical aspects of giant impact simulations*. *Monthly Notices of the Royal Astronomical Society*, 467(4), 4252–4263 (2017).
- Richardson, D. C., Leinhardt, Z. M., Melosh, H. J., Bottke, J., W. F. and Asphaug, E. (2002). *Gravitational Aggregates: Evidence and Evolution*, (pp. 501–515).
- Saito, J., Miyamoto, H., Nakamura, R., Ishiguro, M., Michikami, T. et al. *Detailed Images of Asteroid 25143 Itokawa from Hayabusa*. *Science*, 312(5778), 1341–1344 (2006).
- Schäfer, C. M., Wandel, O. J., Burger, C., Maindl, T. I., Malamud, U. et al. *A Versatile Smoothed Particle Hydrodynamics Code for Graphic Cards*. *Astronomy & Computing* (submitted).
- Schäfer, C. (2005). *Application of Smooth Particle Hydrodynamics to selected Aspects of Planet Formation*. Ph.D. thesis, Eberhard-Karls-Universität zu Tübingen.
- Sirono, S. and Greenberg, J. *Do Cometesimal Collisions Lead to Bound Rubble Piles or to Aggregates Held Together by Gravity?*. *Icarus*, 145(1), 230 – 238 (2000).
- Sirono, S.-i. *Conditions for collisional growth of a grain aggregate*. *Icarus*, 167 (2004).
- Speith, R. (1998). *Untersuchung von Smoothed Particle Hydrodynamics anhand astrophysikalischer Beispiele*. Ph.D. thesis, Eberhard-Karls-Universität Tübingen.
- Speith, R. (2006). *Improvements of the numerical method Smoothed Particle Hydrodynamics*. Habilitation, Eberhard-Karls-Universität Tübingen.
- Stellingwerf, R. F. and Wingate, C. A. *Impact Modelling with SPH (Invited paper)*. *Memorie della Società Astronomia Italiana*, 65, 1117 (1994).
- Stern, S. A., Weaver, H. A., Spencer, J. R., Olkin, C. B., Gladstone, G. R. et al. *Initial results from the New Horizons exploration of 2014 MU69, a small Kuiper Belt object*. *Science*, 364(6441) (2019).
- Stewart, S. T. and Ahrens, T. J. (1999). *Porosity Effects on Impact Processes in Solar System Materials*. In *APS Shock Compression of Condensed Matter Meeting Abstracts*, APS Meeting Abstracts, (p. R5.02).

- Thomas, P., A'Hearn, M., Belton, M., Brownlee, D., Carcich, B. et al. *The nucleus of Comet 9P/Tempel 1: Shape and geology from two flybys*. *Icarus*, 222(2), 453 – 466 (2013). Stardust/EPOXI.
- Veverka, J., Thomas, P., Harch, A., Clark, B., Bell, J. et al. *NEAR Encounter with Asteroid 253 Mathilde: Overview*. *Icarus*, 140(1), 3 – 16 (1999).
- Wandel, O. J., Schäfer, C. M. and Maindl, T. I. (2017). *Collisional fragmentation of porous objects in planetary systems*. In T. I. Maindl, H. Varvoglis, & R. Dvorak (Eds.) *The First Greek-Austrian Workshop on Extrasolar Planetary Systems*, (pp. 225–242).
- Watson, W. W. *letter on the porosity of asteroids*. *Minor Planet Bulletin*, 5, 32 (1978).
- Weidenschilling, S. J. and Cuzzi, J. N. *Protostars and Planets III* (1993).
- Weidling, R., Güttler, C., Blum, J. and Brauer, F. *The Physics of Protoplanetary Dust Agglomerates. III. Compaction in Multiple Collisions*. *The Astrophysical Journal*, 696 (2009).
- Yoshida, F. and Nakamura, T. *Size Distribution of Faint Jovian L4 Trojan Asteroids*. *The Astronomical Journal*, 130(6), 2900–2911 (2005).
- Yu, M., Huang, Y., Deng, W. and Cheng, H. *Forecasting landslide mobility using an SPH model and ring shear strength tests: a case study*. *Natural Hazards and Earth System Sciences*, 18(12), 3343–3353 (2018).

Acknowledgement

First of all, I would like to give my sincere thanks to Prof. Wilhelm Kley for giving me this opportunity to do my PhD in his group. He was always asking about my progress and I am thankful for his supervision as well as his trust in my work.

A huge "Thank you" goes to Christoph Schäfer for the mental as well as the professional support, a lot of advice and many challenges, as well as the funny and interesting personal talks. I am very grateful to have worked with and under you.

I would like to thank Daniel Thun and Marius Hertfelder for the enjoyable years as office colleagues.

A special thank you goes to all the new SPH guys and girls who started working with our code, since it was really fun helping you all out.

Gela Hämmerling, as well as Anna Penzil, thanks for proofreading and giving the work its final touch.

Furthermore, I want to give my thanks to the whole group, since the working environment was really enjoyable.

Last but not least, I want to thank my parents for their mental and financial support over the last decade. Without them this PhD thesis would not have been possible.